UC San Diego
UC San Diego Electronic Theses and Dissertations

Title
Investigation of Delamination Initiation and Propagation in the Vicinity of Fastener Locations in Primary Composite Structures

Permalink
https://escholarship.org/uc/item/5gn936zd

Author
Ngo, Mimi

Publication Date
2019

Peer reviewed|Thesis/dissertation

eScholarship.org Powered by the California Digital Library
University of California

UNIVERSITY OF CALIFORNIA SAN DIEGO

Investigation of Delamination Initiation and Propagation in the Vicinity of Fastener Locations in Primary Composite Structures

A dissertation submitted in partial satisfaction of the
requirements for the degree Doctor of Philosophy

in

Structural Engineering

by

Mimi Ngo

Committee in charge:

Professor Hyonny Kim, Chair
Professor Veronica Eliasson
Professor Francesco Lanza Di Scalea
Professor Ken Loh
Professor Vitali Nesterenko

2019

Copyright

Mimi Ngo, 2019

All rights reserved.

The Dissertation of Mimi Ngo is approved, and it is acceptable in quality and form for publication on microfilm and electronically:

_____

_____

_____

_____

_____
Chair

University of California San Diego

2019

TABLE OF CONTENTS

Signature Page iii

Table of Contents iv

List of Abbreviations vii

List of Symbols viii

List of Figures ix

Acknowledgements xix

Vita xxi

Abstract of the Dissertation xxii

1 Introduction 1

1.1 Motivation 1

1.2 Objective 3

1.3 Novel Contribution 4

2 Background 6

2.1 Bearing Failure of Carbon Fiber Composites 6

2.2 Effect of Bolted Joint Configurations on Bearing Failure 8

2.3 Composite Damage Due to Drilling 14

2.4 Effect of Clamping Pressure on Bearing Failure 19

2.5 Effect of Composite Layup on Bearing Failure 23

2.6 Fatigue Behavior of Composites 25

3 Experiment Test Setup 30

3.1 Specimen Design 31

3.2 Composite Specimen Drilling 33

3.3 Single Lap Shear (SLS) and Double Lap Shear (DLS) Test 40

3.4 Semi-Circular Notch (SCN) Test 44

3.5 Nondestructive Investigation (NDI) 47

3.6 MTS Hydraulic Test Setup 50

4 Experimental Results 53

4.1 Bearing Strengths 53

4.2 Bearing Progressive Damage of Composite Materials 55

4.3 Double and Single Lap Shear Static Test Comparison 68

4.4 Double Lap and Single Lap Shear Fatigue Test 74

4.5 Semi-circular Notch Static Test 98

5 Finite Element Modeling 109

5.1 Virtual Crack Closure Technique (VCCT) 109

5.2 Semi-Circular Notched Model Description 114

5.3 Preliminary Studies 121

5.4 SCN FE Model with No Damage 126

5.5 Bearing Stress with Hashin Failure Criteria and VCCT 129

6 Conclusions 137

References 140

Appendices 144

A. Drilling Process for Composite Material 144

B. Fixture and Specimen Drawings 147

C. Ultrasonic C-scan Settings 149

D. Static and Fatigue Test Procedure 149

E. Bearing Strength for DLS Specimens 153

F. Hole Elongation Measurements 154

LIST OF ABBREVIATIONS

DLS	Double Lap Shear
SCN	Semi-circular Notch
SLS	Single Lap Shear
UCSD	University of California, San Diego
UT	Ultrasonic Testing
VCCT	Virtual Crack Closure Technique

LIST OF SYMBOLS

A	Cross-sectional Area, m^2
a	Crack Length, m
b	Width of element size
d	Length of element Size
F	Force, N
G_I	Mode I strain energy release rate, N-m/m^2
G_{II}	Mode II strain energy release rate, N-m/m^2
G_{III}	Mode III strain energy release rate, N-m/m^2
G_{Ic}	Mode I critical strain energy release rate, N-m/m^2
G_{IIc}	Mode II critical strain energy release rate, N-m/m^2
G_{IIIc}	Mode III critical strain energy release rate, N-m/m^2
G_{equiv}	Equivalent strain energy release rate, N-m/m^2
G_{equivC}	Equivalent critical strain energy release rate, N-m/m^2
TOF	Time-of-flight, sec
σ_{brg}	Bearing Stress, N/m^2

LIST OF FIGURES

Figure 1.1: Bearing failure due to cyclic loading of a countersunk bolted joint. 2

Figure 2.1: Common bolted joint failure model [1]..... 7

Figure 2.2: Bearing failure of joint loaded to 23 kN (left) and formation of kink bands in bearing plane (right) [4]. 8

Figure 2.3: Typical joint configurations on aerospace structures [4]. 9

Figure 2.4: Out-of-plane displacement caused by eccentric load path in single lap joint [4]. 9

Figure 2.5: Contact stress due to secondary bendingpin [4]. 10

Figure 2.6: Typical pin and fasteners used in bolted joints. Pin is used for pure bearing test since it is geometrically symmetric about pin's length direction. Pure bearing test eliminates factors taht can influence bearing strength, such as clamping pressure. 11

Figure 2.7: Double lap shear joint configuration cross-sectional view. 11

Figure 2.8: Microscopy of composite material experiencing bearing load with a protruding head (left) and countersunk (right) fastener [6]. 13

Figure 2.9: Radial stress distribution at the hole boundary of the composite having a countersunk (left) and protruding head (right) fastener [6]. 13

Figure 2.10: Bearing static test results for protruding head joint versus countesunk joint [7]. 14

Figure 2.11: Peel up delamination when drill enters (left) and push out delamination when drill exits (right) [12]. 15

Figure 2.12: Uncut fibers at the exit side caused by a sharp drill (left) and blunt drill (right) [9]. 16

Figure 2.13: Effect of speed and feed rate on thrust force [14]. 17

Figure 2.14: Hole size from different feed rates at 12,000 rpm [14]. 18

Figure 2.15: Bearing stress due to various drilling feed rates [15]. 18

Figure 2.16: Double lap joint fixture and specimen assembly. The applied torque-up load on the nut and transferred to the washers to provide lateral constraint (out-of-plane deformation). 20

Figure 2.17: Effect of clamping pressure on bearing strength and hole elongation [16].. 22

Figure 2.18: Optical microscopies of bearing damage in bolted joints with various clamping pressure [16]. 22

Figure 2.19: Bearing failure modes due to clamping pressure [16]. 23

Figure 2.20: Effect of stacking sequence on bearing failure load [22]. 24

Figure 2.21: Effect of 0° plies versus 90° plies on bearing strength [25]. 25

Figure 2.22: Movement of bolt during fatigue loading [26]. 26

Figure 2.23: Hole wear caused by fatigue loading in composite bolted joint [27]. 26

Figure 2.24: Hole elongation during pin-bearing fatigue test [28]. 28

Figure 2.25: Fatigue test of pin-bearing failure sequence [28]. 28

Figure 3.1: Bearing Specimens for DLS and SLS (left) and SCN (right). 32

Figure 3.2: Bearing specimen cross-sectional view. 33

Figure 3.3: Composite hole drilling setup on the CNC millimg machine. 34

Figure 3.4: Optical microscopy image of a countersunk hole drilled from using the baseline drill parameters. Rough surfaces were created due to fast feed rate, which does not allow enough time for tool to cut the composite. 37

Figure 3.5: Optical microscopy of countersunk hole with slow feed rate. The tool overheats due to friction causing gouches from matrix burn-out. 38

Figure 3.6: Optical microscopy of countersunk hole showing no flaws (i.e., delamination and gouges from matrix burnt-out). Drill parameters used to create this hole was used to fabricate all 9.53 mm countersunk hole for tested specimens. 39

Figure 3.7: Flourescent dye penetrant test performed on the specimen that was fabricated with the optimal drill, ream and countersunk paraemters. No matrix burnt-out or delamination on hole surface. Gouges on the side of specimen was due to sectioning the specimen with a wet tile-saw. 39

Figure 3.8: Delamination induced due to high drill feed rate and no stiff support where the tool exits. 40

Figure 3.9: Double lap shear test configuration using a cusom designed countersunk bolt. A torque load of 0.50 N-m (finger-tight) was used in this setup. 42

Figure 3.10: Single lap shear test configration with hi-lock fastener. Torque up load of 45 N-m was applied to this joint configuration. 42

Figure 3.11: Location of where the hole elongation is measured using a hole gauge and micrometer. Measurements were taken three times and the averaged. 43

Figure 3.12: SCN through-hole and countersunk specimen geometry. 45

Figure 3.13: SCN specimen and fixture assembly for bearing test on the MTS machine. 45

Figure 3.14: Top view (left) and side view (right) of SCN specimen and fixture assembly. 46

Figure 3.15: Ultrasonic C-scan system. 48

Figure 3.16: Ultrasonic pulse-echo technique. 49

Figure 3.17: C-scan (left) and the corresponding A-scan (right) for one pixel on the C-scan image. 50

Figure 3.18: Illustration of cyclic loading procedure. 52

Figure 4.1: Typical bearing load vs. displacement plot form a static test. Load level definitions used to study progressive damage of composite specimens are indicated. 54

Figure 4.2: Onset of bearing damage defined by 5% deviation from the experimental results. 54

Figure 4.3: DLS static test of three Reference laminate tested at low, medium and ultimate loads. 57

Figure 4.4: DLS static test of three laminates from the specimen type with large groupings of 0° plies tested at low, medium and ultimate loads. 57

Figure 4.5: DLS static test of three laminates from the specimen type with large change in angle plies tested at low, medium and ultimate loads. 58

Figure 4.6: Schematic view of microscopy sectioning. 59

Figure 4.7: Optical microscopies of DLS static specimens tested at low, mid and ultimate failure loads. 60

Figure 4.8: Microscopy of the DLS specimen from the reference laminate after loaded to low load (28.6 kN). 63

Figure 4.9: Microscopy of the DLS specimen with large grouping of 0° plies after experiencing low load (36.7 kN). 63

Figure 4.10: Microscopy of the DLS specimen with large change in angle plies after experiencing low load (28.1 kN). 64

Figure 4.11: Microscopy of the DLS specimen from the reference laminate after stopping the experiment at mid load (45.1 kN). 64

Figure 4.12: Microscopy of the DLS specimen with large grouping of 0° plies after experiencing mid load (39.4 kN). 65

Figure 4.13: Microscopy of the DLS specimen with large change in angle plies that was stopped at mid load (56.4 kN). 65

Figure 4.14: Optical microscopy of a DLS specimen from the reference laminate type that was loaded to 57.1 kN. 66

Figure 4.15: Optical mircoscopy of the DLS specimen with large grouping of 0° plies that was loaded to 57.1 kN. 66

Figure 4.16: Microscopy of the DLS specimen type with large change in angle plies after experiencing 56.9 kN. 67

Figure 4.17: Demonstration of delamination initiation after fiber fracture. 67

Figure 4.18 DLS versus SLS static test results for the reference type spcimen. 69

Figure 4.19: Static test results for DLS and SLS specimens with large groupings of 0° plies. 69

Figure 4.20: DLS and SLS static test results for specimens with large change in angle plies. 70

Figure 4.21: Microscopy of the SLS reference laminate that experienced 45.9 kN. 72

Figure 4.22: Microscopy of the SLS laminate with large groupings of 0° plies after experiencing 44.8 kN. 73

Figure 4.23: Microscopy of image from the SLS specimen with large change in angle plies that was loaded to 47.4 kN. 73

Figure 4.24: Example of a countersunk specimen C-scan image. 75

Figure 4.25: Static test plots performed after completing a set number of cyclic loading for a single specimen. 77

Figure 4.26: DLS fatigue test results illustrating percent change in joint stiffness and hole elongation verus number of cycles. 77

Figure 4.27: Ultrasonic C-scan images for a single DLS fatigue specimen used to monitor delamination propagation. There are no significant delamination growth until increasing load, which can be observed at 78,000 cycles and 98,000 cycles. 78

Figure 4.28: Optical microscopy of a DLS specimen after performing 178,000 cycles. Significant damage occurred in the straight shank region of the bolted hole. 79

Figure 4.29: Bolted joint after 4,000 loading cycles at 66% of the ultimate bearing load. 80

Figure 4.30: DLS fatigue test results for each laminate type comparing specimens loaded at 66% versus 50% ultimate bearing stress. 84

Figure 4.31: An example of a pristine specimen with delamination induced by drilling. 85

Figure 4.32: Static tests performed after completing a set of cyclic loading to monitor bolted joint stiffness for all lamiante types. 88

Figure 4.33: Change in joint stiffness and hole elongation for the reference laminate that was cyclic loaded at 50% ultimate bearing stress. 89

Figure 4.34: Change in joint stiffness and hole elongation for the laminate with large groupings of 0° plies that was loaded at 50% ultimate bearing stress. 89

Figure 4.35: Percent change in hole elongation and joint stiffness versus cycles for for the specimen with large change in angle plies that was loaded at 50% ultiamte bearing stress. 90

Figure 4.36: C-scan images used to monitor delamination growth in fatigue test for A) large groupings of 0° plies, B) reference lamiante and C) large change in angle plies. 91

Figure 4.37: Ultrasonic C-scans of specimen cycled at 66% ultimate bearing stress (top) versus 50% ultimate bearing stress (bottom). 93

Figure 4.38: Microscopy of the reference laminate after cyclic loading it to 66% ultimate bearing stress. 95

Figure 4.39: Microscopy of the DLS specimen with large grouping of 0° plies after performing cyclic load at 66% ultimate bearing stress. 95

Figure 4.40: Microscopy of the DLS specimen with large chagne in angle plies after performing cyclic load at 66% ultimate bearing stress. 96

Figure 4.41: Microscopy of DLS reference laminate after experiencing cyclic load at 50% ultimate bearing stress. 96

Figure 4.42: Microscopy of DLS specimen with large grouping of 0° plies after experiencing cyclic load at 50% ultimate bearing stress. 97

Figure 4.43: Microscopy of DLS specimen with large change in angle plies after cyclic loading it at 50% ultimate bearing stress. 97

Figure 4.44: DLS and SCN static test results for three laminate types. 99

Figure 4.45: Microscopies of SCN through-hole (left) and countersunk (right) specimens after bearing static test. 103

Figure 4.46: Ultrasonic C-scans of SCN through-hole (top) and countersunk hole (bottom) after static test. 104

Figure 4.47: Microscopies of DLS versus SCN countersunk specimens after performing static test. 105

Figure 4.48: Optical microscopies of DLS fatigue versus SCN countersunk static tested speciimen for all laminate types. 107

Figure 4.49: Pin bending effect on material erosion during fatigue test 108

Figure 5.1: Three frature modes including Mode I (opening mode), Mode II (sliding mode), Mode III (tearing mode) [30]. 110

Figure 5.2: Crack extension from node release in Mode I strain energy release rate calculation [34]. 112

Figure 5.3: Area under the force versus displacement plot from nodes 2 and 5 is used to calculate strain energy release rates [34]. 113

Figure 5.4: FE model of SCN specimen with steel pin assembly (top) representing the setup for SCN test configuration without the aluminum plates on both sides (bottom)..... 115

Figure 5.5: Semi-circular notched FE model illustrating how the plies were partitioned through thickness of the laminate. 115

Figure 5.6: FE model of SCN specimen illustrating pre-crack locations for using VCCT in Abaqus. 117

Figure 5.7: Optical microscopy from SCN specimens showing delaminaiton locations, which was used to determine the placements of pre-cracks in the FE model..... 118

Figure 5.8: Boundary conditions and displacement applied to the SCN FE model in Abaqus. 121

Figure 5.9: Element size for mesh sensitivity study. The mesh size was changed in the radius geometry near the crack tip. 122

Figure 5.10: Mesh sensitivity study for SCN FE model with VCCT and Hashin damage included. Mesh size 0.8 mm and 1 mm show closer convergence behavior. 123

Figure 5.11: Benchmark study case performed on DCB model to verify VCCT process in Abaqus is correct. Strain energy release rate (left) and critical load at crack initiation (right) was matched with Ronald Kreuger's DCB model. 125

Figure 5.12: FE model of SCN specimen with and without damage compared to experimenta test data for model verification. 126

Figure 5.13: Contour plot of the bearing stress distribution on the loading direction. Units for stress displayed is Pa. 127

Figure 5.14: Transverse shear stress of SCN FE model show greatest shear stress at the center of the pin-bearing surface on the conical region. Units are in Pa. 128

Figure 5.15: Transverse normal stress on the pin-bearing surface of the SCN laminate. Stress units displayed is Pa. 129

Figure 5.16: Hashin fiber compresison failure, which show locations where pin loading has the most affect on the bolt-bearing surface. Red color (value of 1) indicates damage has occured, whereas blue color (value of 0) means there is no damage. 130

Figure 5.17: Hashin fiber tension failure image illustrating locations where fibers have high tensile stress. Red color (value of 1) indicates damage has occured, whereas blue color (value of 0) means there is no damage. 131

Figure 5.18: Hashin matrix compressiom failure with four pre-cracks, which occurs first before other failure modes occur (i.e. fiber tension and compression). Red color (value of 1) indicates damage has occured, whereas blue color (value of 0) means there is no damage. 131

Figure 5.19: Hashin matrix tension failure in indicating tensile stress in matrix is greatest where delamination occurs. Red color (value of 1) indicates damage has occured, whereas blue color (value of 0) means there is no damage. 132

Figure 5.20: Microscopy of the reference layup type specimen showing location of delamination. This supports the damage observed in the FE model..... 132

Figure 5.21: Bond state mapping of each crack. Red color indicate the plies between the cracks are still bonded and blue represents disbond. Crack 1 shows delamination initiation first..... 134

Figure 5.22: Strain energy release rate from Mode II of crack 1 prior to delamination initiation. Mode II is the dominating failure mode for delamination in this joint configuration. The material fracture toughness input was 554 J/m^2..... 135

Figure 5.23: Final bond state status before analysis was terminated. Delamination propagated in Crack 1 and nodes began to release in crack 2. 135

Figure 5.24: Bearing stress on the bolt-hole surface showing stress concentration between the concial and shank interface. 136

Figure 6.1: Single lap shear test fixture with dimensions in inches..... 147

Figure 6.2: Double lap shear test fixture with dimensions in inches. 148

Figure 6.3: Dimensions of the custom designed pin used in the double lap shear test... 148

Figure 6.4: Basic TestWare user interface. Simple test operations can be modified during the test. 150

Figure 6.5: Procedure used for fatigue test on the MPT program. Each type can either run simutaneously with one another or in a chronological order. 151

LIST OF TABLES

Table 3.1: Bearing specimens layup information 32

Table 3.2: Tools used to dril, ream and countersink a 9.53 mm hole on all composite specimens. 35

Table 3.3: Baseline drilling procedure for fabricating a countersunk hole on a composite laminate. 36

Table 3.4: Drilling procedure with increasing speed rate and decreasing feed rate. 37

Table 3.5: Parameters used to drill a 9.53 mm countersunk hole on all composite specimens using the CNC machine. 38

Table 4.1: DLS joint stiffnesses from static tests. 58

Table 4.2: Peak load applied to the static DLS test specimens. 59

Table 4.3: Average initial bearing strength. 70

Table 4.4 : Average ultimate bearing strength. 71

Table 4.5: Hole elongation measured after completing a set number of cycles for a DLS specimen loaded at 66% of ultimate bearing stress from each laminate type. 82

Table 4.6: Hole elongation measured after completing a set number of cycles for a DLS specimen loaded at 50% of ultimate bearing stress from each laminate type. 82

Table 4.7: Average initial failure stress from DLS and SCN static tests showing that regardless of the test type, their initial failure stress is similar. 100

Table 4.8: Bearing strength from DLS and SCN static tests. 100

Table 5.1: Material properties of AS4/3501-6 carbon fiber reinforced epoxy composite. 116

Table 5.2: VCCT input parameters for AS4/3501-6 composite material. 119

Table 5.3: Hashin damage input parameters for Abaqus. 119

Table 6.1: Speed and feed rates used to fabricate all specimens used in this research... 145

Table 6.2: Ultrasonic C-scan input parameters on the UTwin software. 149

Table 6.3: Hole elongation measured for the reference specimens that were cycled at 50% ultimate bearing stress. 154

Table 6.4: Hole elongation measured for the reference specimens that were cycled at 50% ultimate bearing stress. 155

Table 6.5: Hole elongation measured for the specimen with large groupings of 0° plies that were cycled at 50% ultimate bearing stress. 156

Table 6.6: Hole elongation measured for the specimen with large change in angle plies that were loaded to 50% ultimate bearing stress..... 157

Table 6.7: Hole elongation measured for the specimen with large change in angle plies that were loaded to 50% ultimate bearing stress. Continuation of Figure 6.5. ... 158

Table 6.8: Hole elongation measured for all specimens that were loaded to 66% ultimate bearing stress..... 158

Table 6.9: Hole elongation measured for specimen with large groupings of 0° plies that were loaded to 66% ultimate bearing stress. Continuation of Table 6.7, but for this laminate type. 159

Table 6.10: Hole elongation measured for the reference lamiante and one with large chagne in angle plies that were loaded to 66% ultimate bearing stress. Continuation of Table 6.8, but for these laminate type..... 159

Table 6.11: Bearing Strength for all specimens tested under static load. 153

ACKNOWLEDGEMENTS

With sincere gratitude, I would like to express my appreciation towards Dr. Hyonny Kim for this truly memorable and valuable research experience. Whether or not there was progress in research, his continuous support, guidance and patience made every moment of my Ph.D. an enjoyable experience. His realistic optimism on research and life greatly influenced the way I approach my own research and life. Thank you.

I would also like to give a special thanks to Joshua Rivera from NAVAIR for supporting this work and Dr. Satchi Venkataraman from San Diego State University for his valuable guidance. Thank you, Stephen Porter for your continuously supporting my academic growth during my time as an undergraduate volunteer up until the end of my PhD journey. I must thank Dr. Francesco Lanza Di Scalea for allowing me to operate with your C-scan machine any time I needed it for my research. A very big thank you to everyone in my research team for assisting me with my research and teaching me things that would have taken me hours to figure out on my own.

Last but not in the least, I must thank my family and friends for supporting me behind the scenes throughout my years at UCSD. I am very grateful to have an unconditionally loving family and friends who always made sure I have everything I need to succeed. Their understanding and patience for me during this time is greatly appreciated. Thank you so much.

Chapters 3 and 4 include materials as it appear in the Investigation of Delamination and Growth Behavior at Fastener Locations in Primary Composite Structures, 2017. Ngo, Mimi and Kim, Hyonny, Proceedings of the 32nd Annual American Society for Composites Technical Conference, 2017 and A Comparative Study on Pin Bearing Effect Under Bearing Static and Fatigue Failure, 2018. Ngo, Mimi and Kim, Hyonny, Proceedings of the 33rd Annual American Society for Composites Technical Conference, 2018. The dissertation author was the primary investigator and author of this paper.

VITA

Education

2014	Bachelor of Science, University of California, San Diego
2017	Master of Science, University of California, San Diego
2019	Doctor of Philosophy, University of California, San Diego

Experience

2013-2014	Undergraduate Student Researcher, Department of Structural Engineering, University of California, San Diego
2014-2019	Graduate Student Researcher, Department of Structural Engineering, University of California, San Diego
2016-2019	Teaching Assistant, Department of Structural Engineering, University of California, San Diego
2018	Engineering Intern, The New-Mid Market Airplane Program, The Boeing Company

PUBLICATIONS

Ngo, M. and Kim, H., "Investigation of Delamination Initiation and Growth Behavior at Fastener Locations in Primary Composite Structures," Proceedings of the 32nd Annual American Society for Composites Technical Conference, October 23-25, 2017, West Lafayette, IN.

Ngo, M. and Kim, H., "A Comparative Study on Pin Bearing Effect Under Bearing Static and Fatigue Failure," Proceedings of the 33rd Annual American Society for Composites Technical Conference, September 24-26, 2018, Seattle, WA.

Ngo, M. and Kim, H., "Investigation of Delamination Initiation and Growth Behavior at Fastener Locations in Primary Composite Structures," Manuscript in preparation.

ABSTRACT OF THE DISSERTATION

Investigation of Delamination Initiation and Propagation in the Vicinity of Fastener Locations in Primary Composite Structures

by

Mimi Ngo

Doctor of Philosophy in Structural Engineering

University of California San Diego, 2019

Professor Hyonny Kim, Chair

Primary aerospace composite structures are commonly assembled with bolted joints due to their ability to transfer high loads and ease of assembly. However, when bolted joints are used beyond their originally intended design life, joint strength can be significantly reduced due to the accumulation of internal damage, necessitating frequent inspections. Furthermore, internal damage in composites (delamination, matrix cracks)

can continue to propagate without visual indications, thus nondestructive testing is required. As a result, maintenance can become very costly, particularly for aircraft that are in-service beyond their designed life expectancy. By establishing a comprehensive understanding of damage propagation behavior, engineers can determine which damage modes to inspect for and reduce inspection frequency. This research aims to support and improve maintenance operations, fleet management, and aircraft design practice by investigating delamination initiations and propagations in the vicinity of fastener holes within fiber-reinforced composite materials.

Static and fatigue bearing were performed using novel test methods developed as part of this research for countersunk fastener joints: the modified countersunk double lap shear (DLS), single lap shear (SLS), and semi-circular notch (SCN) test configurations. DLS and SLS static and fatigue experimental test results were compared to study joint configuration, laminate stacking sequence, and loading condition effect on bearing damage initiation and growth under both static and fatigue loading. From static and fatigue tests, it was observed that major bearing damage accumulates in the straight shank region of the countersunk hole indicating most of the bearing load is carried by the straight shank region. Fatigue bearing test data showed that when the bolted hole elongates, stiffness decreases and internal delamination damage area growth becomes detectable through C-scan. Stated in reverse, if no measurable hole elongation is found, significant delamination is not expected. Complex damage morphology forms in this region, emanating from the loaded bearing face, and creating large wedge-shaped regions that drive delamination propagation with additional loading cycles. Additionally, optical microscopy observations indicated that pin bending might have affected bearing damage

growth. In order to understand the effect of pin bending, a custom designed semi-circular notched experiment was performed on the countersunk hole geometry and compared to the DLS static experiments. Results indicated that the pin bending had no strong effect on the bearing failure morphology for the selected diameter to thickness ratio.

Finite element analysis using Virtual Crack Closure Technique (VCCT) and Hashin failure criteria in Abaqus was used to further understand the internal stress state of the specimen configurations and to investigate the rate of delamination growth and arrest in the SCN and DLS configurations. Results from FEA were used to more comprehensively understand the observations from static and fatigue experiments and to verify hypotheses formulated to explain these observations.

1 INTRODUCTION

1.1 MOTIVATION

Advanced composite materials have been used in many aerospace structures, including primary structures (fuselage and wing) on commercial aircraft, military aircraft, and space structures. Since any large structure is rarely built as one single piece, composites sub-structures are often assembled through bolted joints and/or adhesively bonded joints. It is these complex joint locations, in general, where failure in structures usually originates. Despite the many advantages of adhesively bonded joints, mechanical fasteners are often more desirable due to inherently allowing for assembly and disassembly, visual inspections, repairable reliability, immediate load-bearing ability, and high load carrying capability. However, drilling many holes onto an aircraft can cause stress concentrations throughout the structure. This is a concern, particularly for composite structures, where delamination (separation of plies) may initiate around the bolt hole and propagate during flight. Figure 1.1 shows an example of a single bolt-hole bearing damage in a composite bolted joint assembly that was subjected to cyclic loading.

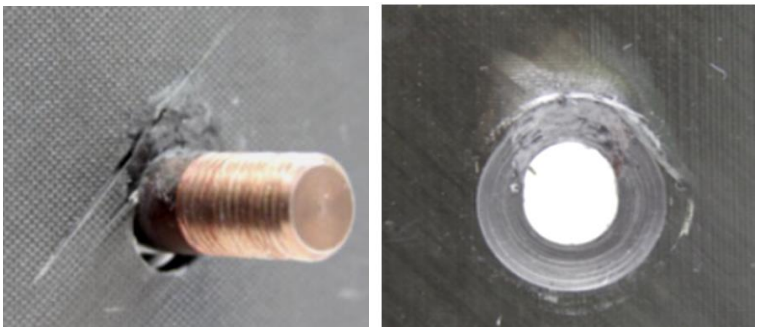

Figure 1.1: Bearing failure due to cyclic loading of a countersunk bolted joint.

Delamination is a failure mode that occurs between the individual plies within the composite laminate, thus it is typically not detectable with a naked eye and requires nondestructive equipment to detect this type of damage. Delamination initiation may be induced during manufacturing through improperly drilling composites, and during operation from taking off, hard landing, accidental impacts, sharp maneuvers, etc. Particularly, composite fighter jets, such as the F/A-18, experience extreme environmental conditions, repetitive impacts, and maneuvers that make it more prone to delamination growth. In order to mitigate risks of delamination propagation during flight, aircraft are often inspected by nondestructive testing techniques such as ultrasonic C-scan. However, using ultrasonic inspections may take days to perform on one aircraft since transducers used are typically 12.7 mm in diameter and depending on the aircraft geometry, it may sometime require different types of transducers and operator skill levels to scan the entire plane. Since composite failure modes, such as delamination initiating and growing at fastener holes, is not comprehensively understood, there is an increase in the need for recurring inspection, retrofit and engineering analysis. As a result, it is very costly to sustain a composite aging aircraft without degrading mission readiness and

capability. Therefore, to aid in the monitoring/inspection and safety assurance of composite aircraft structures, the objective of this research is to develop a comprehensive understanding of bearing failure in countersunk composite bolted joints under both static and cyclic load.

1.2 OBJECTIVE

The main objective of this research is to comprehensively understand delamination initiation and propagation in the vicinity of fastener holes within fiber-reinforced composite bolted joints subjected to static and fatigue loading. In addition, this research intends to establish quantitative and qualitative descriptions of the phenomena governing delamination growth using nondestructive investigation (NDI) and destructive sectioning (optical microscopy). This research focuses heavily on experimental studies of double lap shear, single lap shear and semi-circular notch test configurations. All experiments were performed on three different laminate layup types to investigate the effect of stacking sequence on the bearing damage of composites. Results from experiments will assist in developing methods for predicting bearing damage and delamination growth under fatigue loading. Finite element modeling with the software Abaqus was used in conjunction with experimental results and observations to gain a deep-level understanding of damage modes observed in the experiments.

Chapter 2 provides background on previous work on bearing damage of composites and parameters that may influence bearing strengths. Chapter 3 describes the experimental setup for the three different test configurations, drilling of the composite

bolt holes, ultrasonic C-scan, and MTS test machine. Chapter 4 presents all static and fatigue test results and discussions, beginning with bearing strength definition, damage progression of bearing failure, double lap shear versus single lap shear and double lap shear versus semi-circular notched test. Chapter 5 explains the modeling technique used to better understand experimental results and predict delamination growth and arrest.

1.3 Novel Contribution

Bearing strength of advanced composite materials have been studied for many years. However, past research studies mainly focused on static failure of bolted joints, particularly protruding head fastener (i.e., non-countersunk). Although there are some contributions on the fatigue behavior of composite bolted joints, there is still lacking a comprehensive understanding on fatigue failure of countersunk bolts in composites. Countersunk fasteners are desired in aerospace structures for preserving smooth exterior surfaces needed for being aerodynamically efficient. This research aims to provide experimental observations and prediction methodology for delamination growth under fatigue loading. Various test parameters that influence bearing strengths, such as stacking sequence orientation, clamping pressure, hole geometry and test configurations were investigated to provide a general understanding of damage initiation and growth, including delamination. The outcome of this research provides key observational information and quantitative data about internal damage in composite bolted joints, which is critical for development of detailed model-based prediction capability. This research also provides engineers with understanding of expected failure modes and damage

growth rates with cyclic loading, which can support maintenance operations and fleet management through reducing overall cost from recurring inspection and repair. Understanding the behavior of delamination propagation can also assist engineers on improving aircraft design practice and developing quality verification protocols for composite aircraft.

2 BACKGROUND

This chapter provides a literature review on topics that are directly related to this research. First, a description of common bolted joint failure modes will be discussed. Then, the focus will be on previous work that has been studied to better understand parameters that influence bearing failure.

2.1 BEARING FAILURE OF CARBON FIBER COMPOSITES

Common bolted joint failure modes in composite structures include shear-out, net-section, bearing and bolt failure [1]. Net-section failure is caused by tensile loading on composite components with a small width-to-hole diameter ratio (see Figure 2.1A). Shear-out failure occurs when there is a small edge-to-hole diameter ratio (see Figure 2.1B). Bearing failure is due to compressive stresses acting on the hole surface under loading and failure occurs progressively with increasing load (see Figure 2.1C). Lastly, bolt failure is caused by both shear stresses and bending stresses in the fastener (see Figure 2.1D). In bolted composite joint design, the desired failure mode is bearing failure, with shear-out and net-section failure modes prevented by increasing the width-to-hole diameter and edge-to-hole diameter ratio, as well as selecting appropriate laminate configurations. Since bearing damage is progressive and is an accumulation of local compressive failure at the bearing surface, it is favorable in industry as a failure mode for bolted joints in composite structures, as damage stays localized at the holes and load can redistribute to surrounding fasteners or other load paths. Therefore, this research will primarily focus on investigating the modes of damage behavior resulting when a joint undergoes what is referred to as bearing failure.

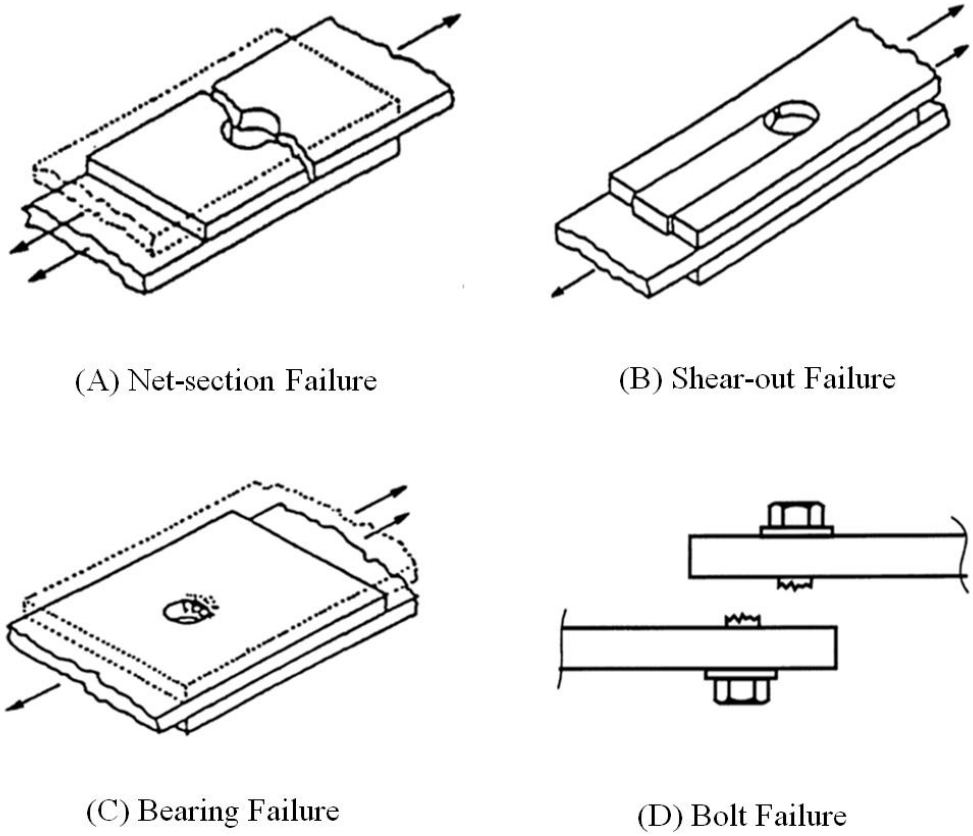

Figure 2.1: Common bolted joint failure model [1].

Bearing failure occurs gradually under compressive loading on the bolt-bearing surface, which involves several failure modes at the micro scale. Typically, bearing failure begins with matrix cracking then followed by buckling of destabilized fibers [4]. Fiber buckling starts in the bearing plane at the 0-degree plies, due to its great stiffness in the loading direction. As loading increases, shear cracks in matrix form, which leads to delamination and kink bands of buckled fibers (see Figure 2.2) [4]. Bearing strength can be affected by many parameters such as bolt clamping pressure, laminate stacking sequence, hole clearance, joint geometry, and washer size. Work that has been studied on these parameters will be discussed in the following sections.

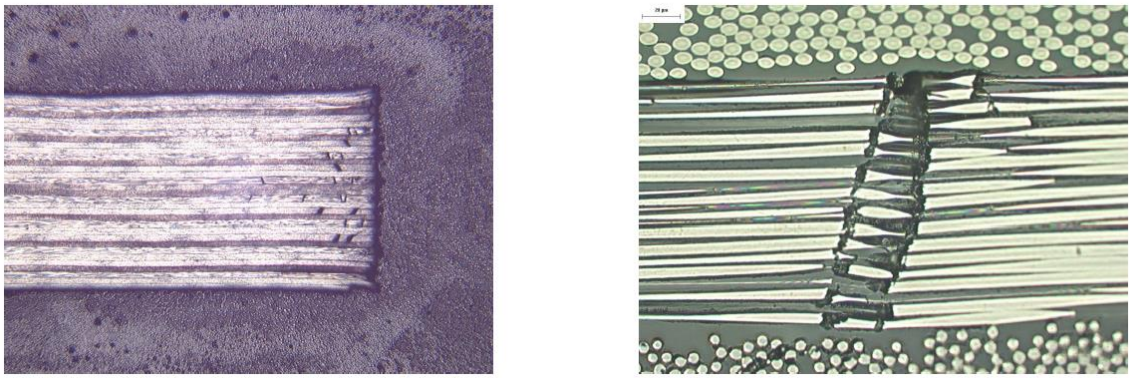

Figure 2.2: Bearing failure of joint loaded to 23 kN (left) and formation of kink bands in bearing plane (right) [4].

2.2 Effect of Bolted Joint Configurations on Bearing Failure

- **Double-Lap Shear vs. Single-Lap Shear.** Composite structures are often joined together in a double lap or single lap joint configuration (see Figure 2.3). For instance, bolting of wing skins to internal structure, connecting sections of the fuselage and assembling the ailerons to the wing box are all joined through either a single lap or double lap joints. A single lap shear joint configuration consists of two members that are bonded by fasteners, which are typically countersunk or protruding heads. The geometry of these fasteners makes this lap joint non-symmetric with respect to the center of the joint. Thus, the eccentricity of the loading on the joint will cause out-of-plane deformation known as secondary bending (see Figure 2.4). When load is applied, the fastener experiences a bending moment, which is reacted by the contact between the fastener and the members. This causes non-uniform stress distribution through the thickness of the

joint, resulting in a non-uniform contact stress profile on the bolt-hole surface (see Figure 2.5). The magnitude of this stress concentration may be influenced by stiffness mismatch from the plates and bolt-hole clearance [4].

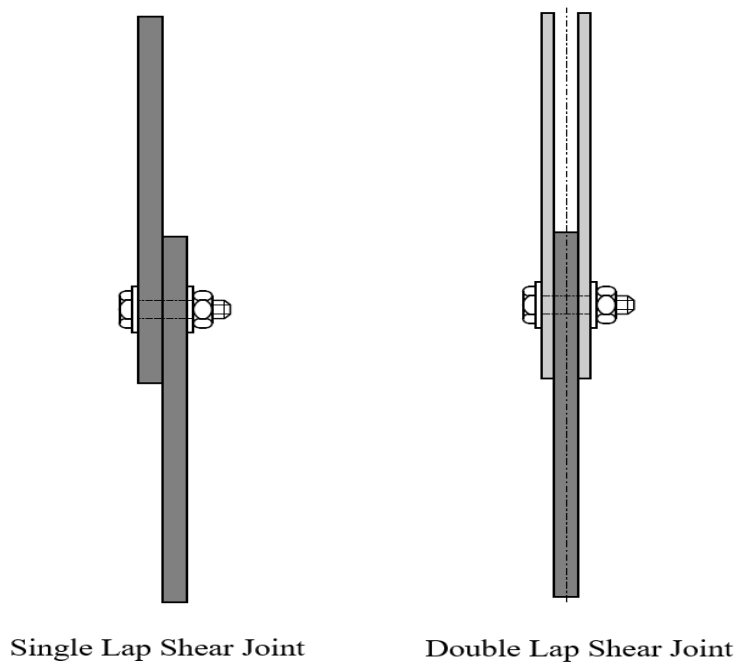

Figure 2.3: Typical joint configurations on aerospace structures [4].

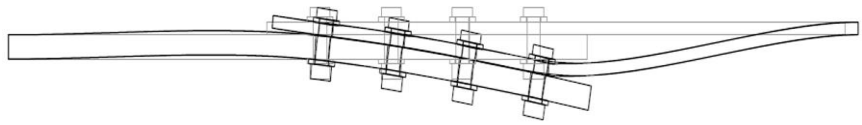

Figure 2.4: Out-of-plane displacement caused by eccentric load path in single lap joint [4].

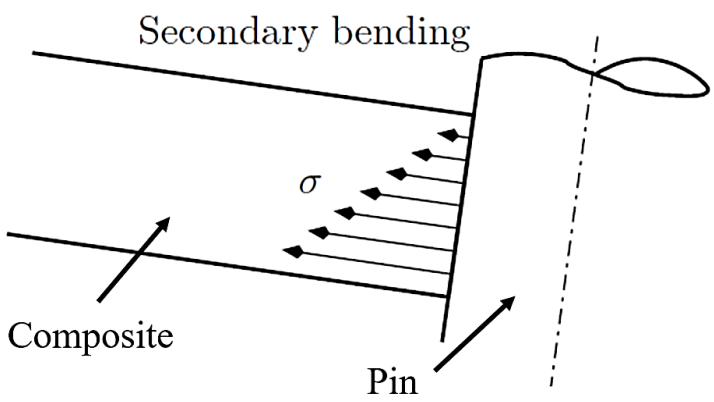

Figure 2.5: Contact stress due to secondary bendingpin [4].

The double lap bolted joint configuration consists of three members bonded together with fasteners, which provides a more symmetric joint compared to the single lap. This is not truly symmetric with respect to the center of the middle member because of the fastener head is often protruding head or countersunk. The fastener geometry is not symmetric about the centerline (see Figure 2.6). However, since there is an additional member on the double lap joint, it minimizes the secondary bending effect. Two outer members resist the load that is applied to the inner member, which prevent the fastener from rotating (see Figure 2.7) globally, although there is still bending of the fastener that occurs which can contribute to the non-uniform bearing stress (e.g., in Figure 2.5). Since two outer members are pressed together to the middle member, some of the load is transferred between the members through friction instead of only in the bolt-hole contact. Additionally, researchers found single-lap joints have lower bearing strengths compared to a double-lap joint due to secondary bending, which results in non-uniform stress distribution the bolt-hole surface [2] and [4].

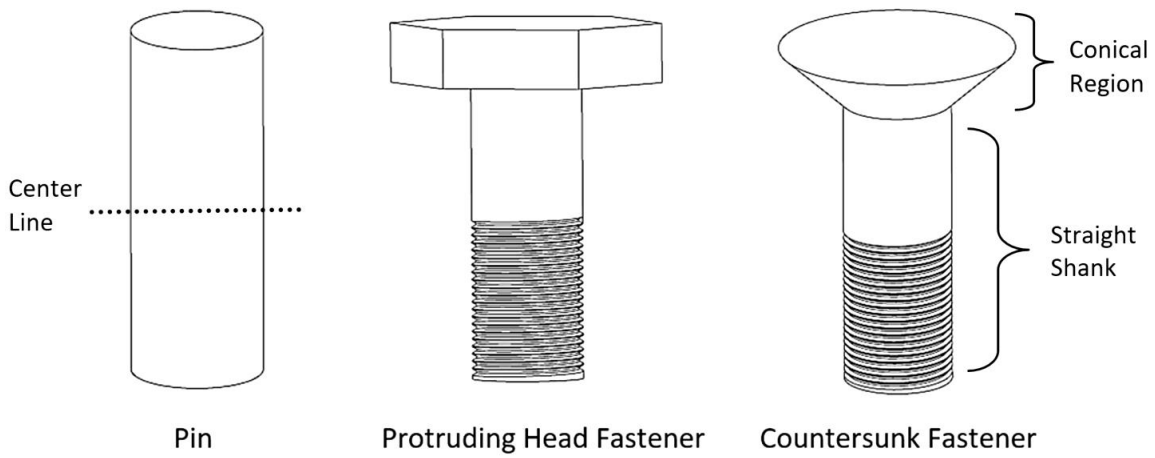

Figure 2.6: Typical pin and fasteners used in bolted joints. Pin is used for pure bearing test since it is geometrically symmetric about pin's length direction. Pure bearing test eliminates factors taht can influence bearing strength, such as clamping pressure.

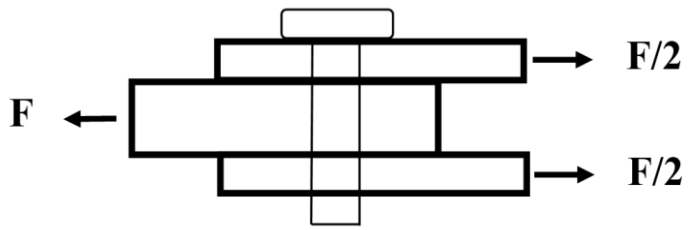

Figure 2.7: Double lap shear joint configuration cross-sectional view.

- **Countersunk vs. Straight Through-Hole Bolted Joints.** Countersunk fasteners are often used rather than protruding head fasteners in aerospace application because of its smooth outer surface (see Figure 2.6). Although study on countersunk fasteners are limited, some researchers found that it produces higher stress concentration at the bolt-hole compared to a straight hole because of the

reduced length from the cylindrical bolt shank [4-8]. The stress concentration from the reduced shank length causes nominal bearing stress to be higher compared to the protruding head [4]. McCartney et al. [6] found that the conical region of the laminate is ineffective in transmitting load, thus bearing damage is found to occur in the straight shank region of the countersunk hole (see Figure 2.8). This is where stress concentration is localized. They also found that the countersunk fasteners produce a greater radial stress distribution (by about 1.7 times) at the hole boundary in the laminate compared to the protruding-head joint (see Figure 2.9). This image show stress concentration at the most outer surface of the laminate and decreases in stress near the conical region. Additionally, T. Qin et al. [7] performed static tests and discovered that the initial stiffness for countersunk and protruding head joints are the same, up until reaching initial failure, which was observed in stage 1 and 2 (see Figure 2.10). Results also show countersunk fastener has a lower initial failure load (about 13.5 kN for countersunk and 16.3 kN for protruding head joint), shown in 3rd stage. Load at 4th stage for the protruding head joint is almost constant, whereas the countersunk joint continues to increase before failure. Lastly, data shows that protruding head has about 4.5% higher final failure load compared to countersunk joint.

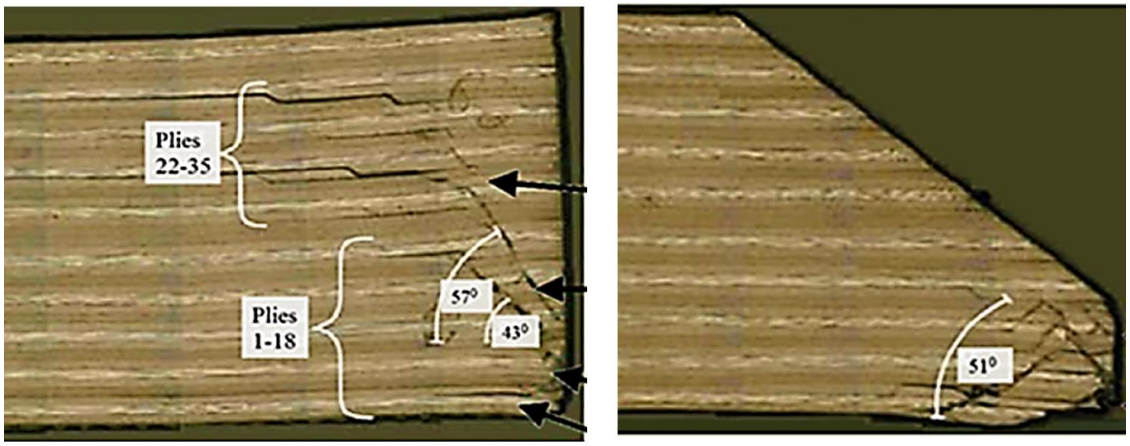

Figure 2.8: Microscopy of composite material experiencing bearing load with a protruding head (left) and countersunk (right) fastener [6].

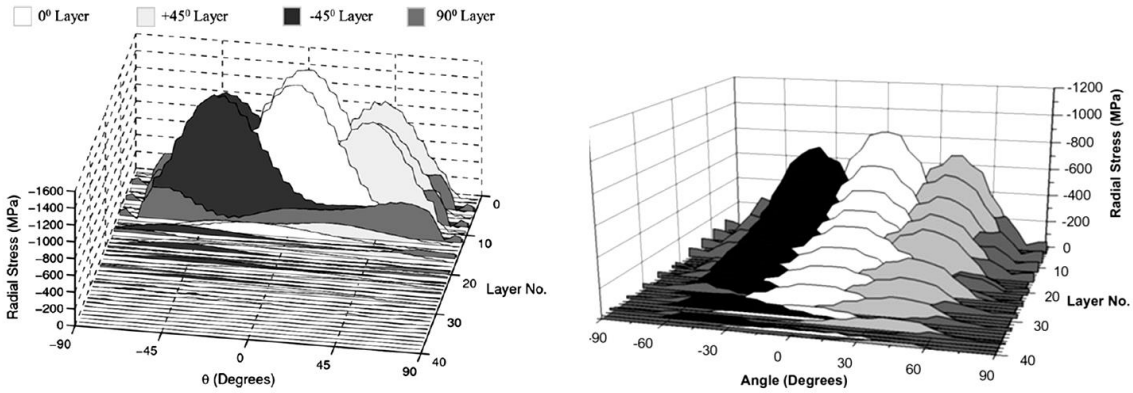

Countersunk **Protruding Head**

Figure 2.9: Radial stress distribution at the hole boundary of the composite having a countersunk (left) and protruding head (right) fastener [6].

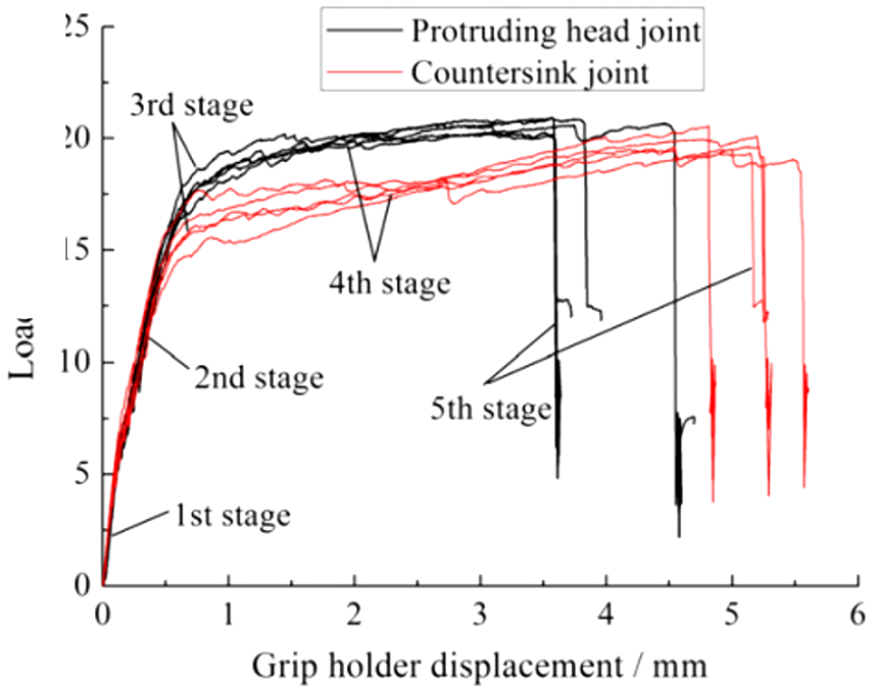

Figure 2.10: Bearing static test results for protruding head joint versus countesunk joint [7].

2.3 Composite Damage Due to Drilling

Performing drill operations on composite structures can introduce many defects such delamination (ply separation), chip-out of fiber and matrix, and matrix overheating. Research has shown damage induced during drilling operation reduces material strength, which affects fatigue life of the structure [9]. Delamination is one of the most critical flaw types and it is a common reason for rejecting a part in aerospace industry [11]. This drilling-induced defect occurs when the drill peels up at the entrance of the hole or pushes out as it exits the composite. During the hole machining process, the drill bit pulls the cut material away and along the flute direction even before the machining process is

complete. This causes the uncut material to spiral upwards, which can induce delamination in the upper most half of the laminate (see Figure 2.11). As the drill tool exits, the uncut thickness of the laminate is more pliable, thus the thrust force from the tool will become greater than the inter-laminar strength causing delamination to initiate. This defect can be resolved by adding a supporting and sacrificial material to the back of the composite, which will provide local stiffness to the laminate as the drill exits.

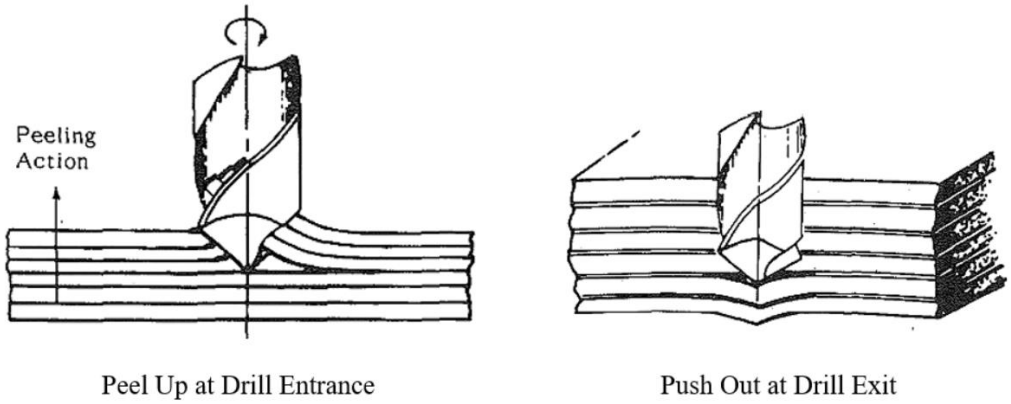

Figure 2.11: Peel up delamination when drill enters (left) and push out delamination when drill exits (right) [12].

Numerous research studies have been performed to investigate parameters that would induce defects while drilling composite materials and found that damage could be caused by tool wear, thrust force, drill type, and feed and speed rates [9]. Persson E. et al. [9] found delamination could because by overheating of the tool and using a blunt drill. A sharp drill bit tip will puncture through the last couple of plies of the laminate over a smaller area compared to a blunt tip (see Figure 2.12). Thus, those plies would be

subjected to a smaller bending force from the tip and produce less delamination. Furthermore, drilling-induced defects, such as fiber and matrix chip-outs are caused when the drill does not cut the fiber, instead it is torn out of the hole surface causing the surface to be rough [9]. In addition, overheating of the tool occurs when the drill speed rate and or thrust force is too high, such that friction between the tool and composite will generate heat and result in matrix damage. Continuously removing the cut material from the hole and using effective cooling methods can assist on achieving a good hole quality.

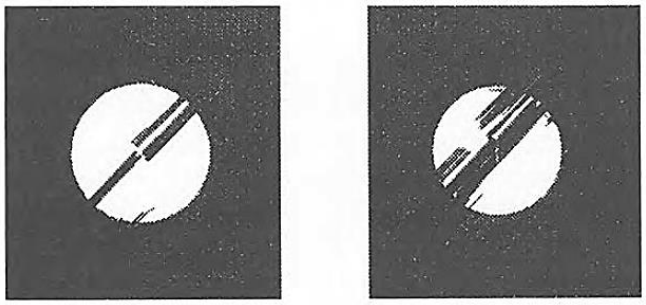

Figure 2.12: Uncut fibers at the exit side caused by a sharp drill (left) and blunt drill (right) [9].

Thrust force is a critical parameter to control, as it causes delamination initiation and propagation in composite drilled holes [13]. Krishnaraj et al. [14] performed an experiment relating thrust force and speed and feed rates (see Figure 2.13). While they found thrust force decreases with a decrease in feed rate and increase in spindle speed rate, this can cause the hole diameter to different from desired nominal diameter (see Figure 2.14. This was found to be caused by self-induced vibration when the tool enters the material. The tool vibrates during the drilling process and if the feed rate is slow and

speed rate is high, the vibration and heating from friction between the tool and composite can lead to a larger hole diameter. Another researcher experimentally tested feed rate versus bearing stress and found that bearing strength increases with a decreased feed rate (see Figure 2.15) [15]. By decreasing feed rate, the thrust force from the tool onto the composite is lower, which decreases delamination. However, as stated earlier, low feed rate can enlarge the hole diameter due to vibration of the tool. All of these investigations on the drilling composites show that it is a very challenging task to attain a damage free hole. Through experiment, Krishnaraj et al. [14] found that the optimal spindle speed and feed rate for drilling thin carbon fiber composite laminates are 12,000 rpm and 0.137 mm/rev, respectively.

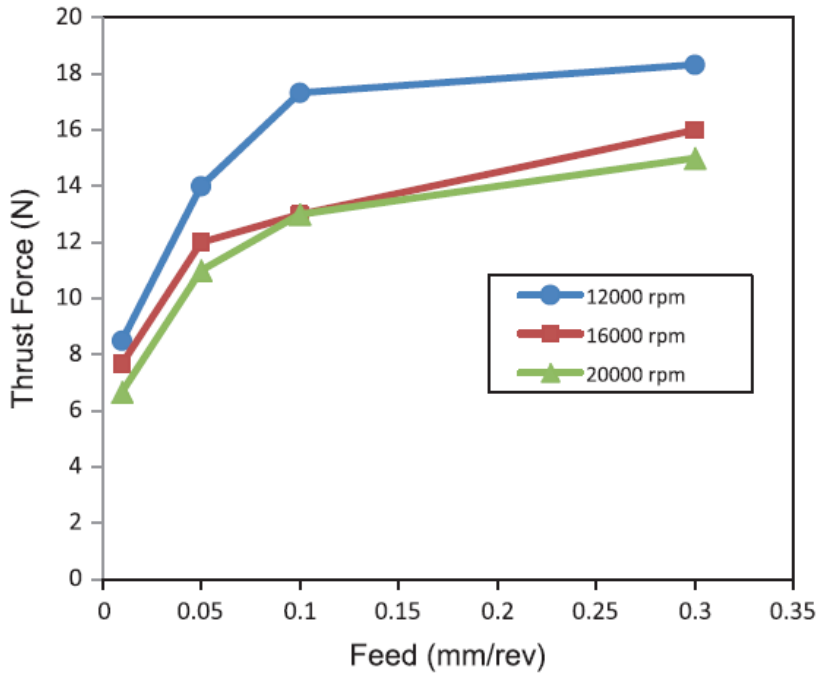

Figure 2.13: Effect of speed and feed rate on thrust force [14].

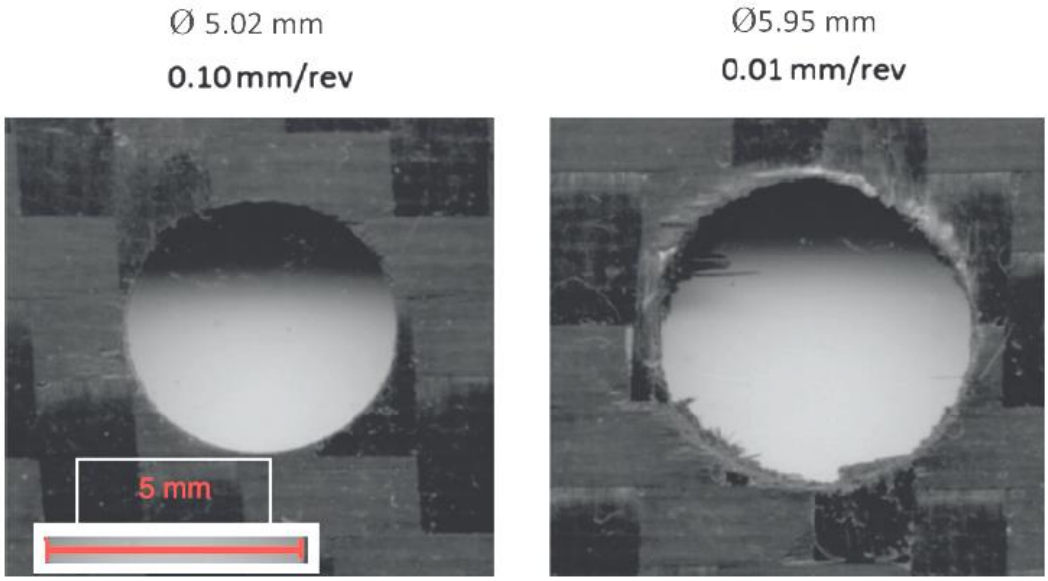

Figure 2.14: Hole size from different feed rates at 12,000 rpm [14].

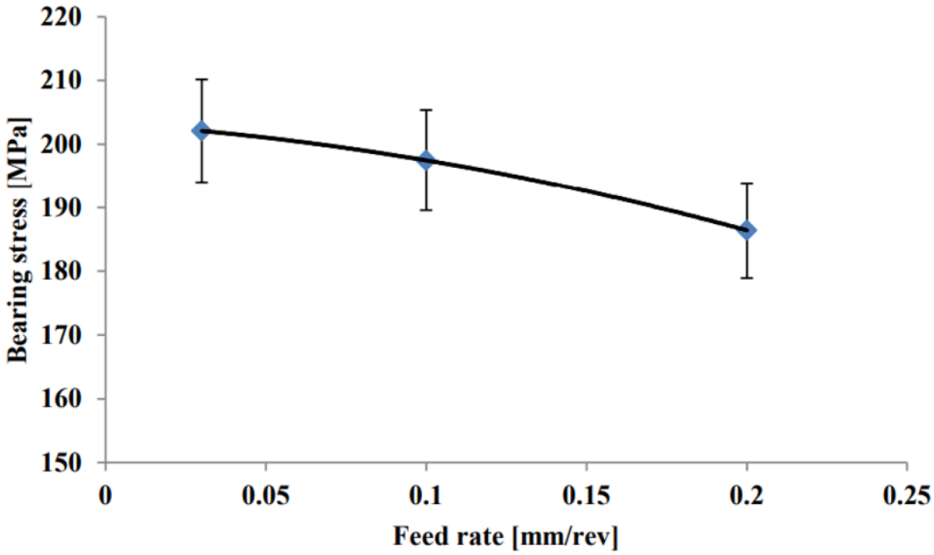

Figure 2.15: Bearing stress due to various drilling feed rates [15].

2.4 Effect of Clamping Pressure on Bearing Failure

Clamping pressure on bolted joints have been investigated by many researchers who all found that increasing clamping pressure will also increase bearing strengths (see Figure 2.17) [16-21]. Clamping pressure is defined as a torque load applied to the nut when assembling the bolted joint. The applied torque load will transfer from the nut to washer and washer to the composite laminate through frictional forces at the interface between those components. The amount of torque applied to the bolted joint can be translated to clamping pressure that the composite experiences, by dividing the load to the washer surface area. This clamping pressure applies lateral constraint to prevent out-of-plane deformation at the bolted joint (see Figure 2.16).

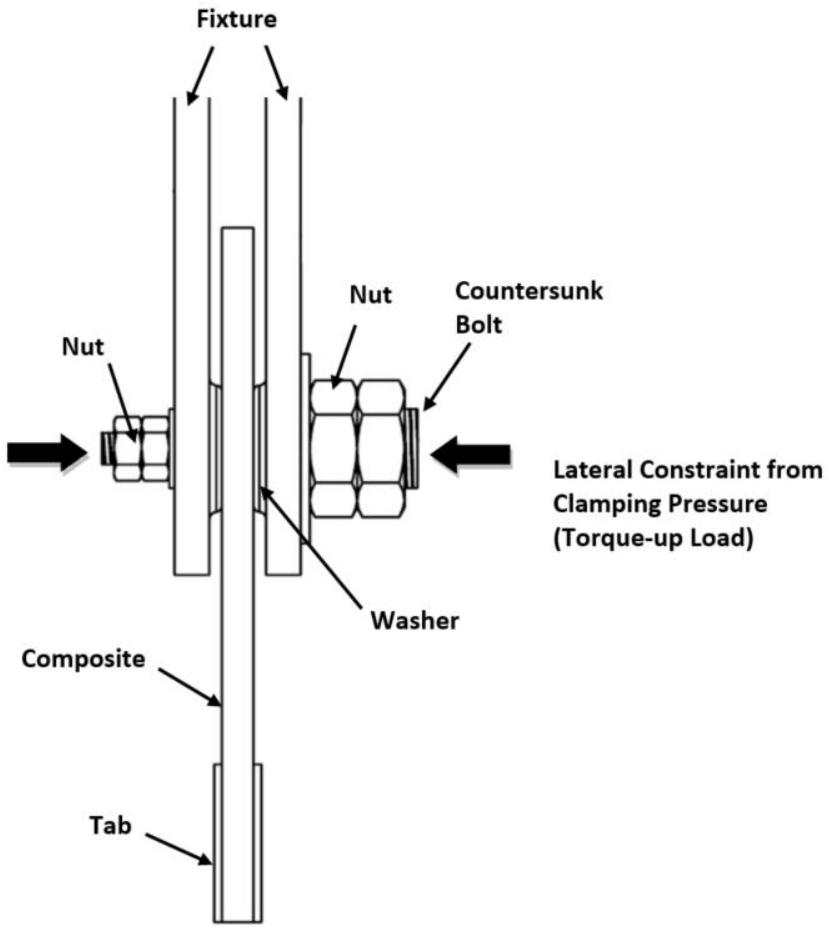

Figure 2.16: Double lap joint fixture and specimen assembly. The applied torque-up load on the nut and transferred to the washers to provide lateral constraint (out-of-plane deformation).

Wang et al. [16] experimentally characterized bearing failure with various clamping pressure and concluded that bolted joints can fail catastrophically if there is no lateral support (see Figure 2.18). An accumulation of bearing damage caused by compressive bearing stress of the pin would lead to shear crack growth. However, lateral supports could suppress shear cracks propagation and change the failure mode from catastrophic to progressive. Crews [17] performed static and fatigue bearing tests on a double lap shear configuration with a protruding head fastener, on various clamp-up

torques. He found that clamping pressure affects bolted joint failure modes. In a simple pin-bearing joint, when there is no clamping pressure, the resulting failure mode would have a “brooming” type characteristic near the hole edge (see Figure 2.18). However, at a high clamp-up torque, specimens fail in shear-out, tension, and then bearing failure and small clamp-up torque shifts the failure mode to shear-out then bearing (see Figure 2.19). Eriksson [18] studied lateral constraint effect on ultimate bearing strength and found specimens clamped at 5.4 N-m yielded 1.5 times higher strength than finger-tightened specimens, and 2.4 times higher strength than the specimen with no lateral constraint (i.e., pin-loaded). Xiao et al. [19] studied bearing strength and failure behavior of bolted composite joints. They concluded clamping forces from washer and bolts cause damage accumulation to expand along the in-plane direction, inside the washer region, in a gradual manner until the delamination extends beyond the edge of the washer, then joint response rapidly decreases. Lastly, Khashaba et al. [20] tested various clamp up torques and washer sizes on a double lap joint configuration and found that increasing washer size may improve contact pressure from the torque to improve bearing strength of the joint. However, if the washer size is too large, the bearing strength decreases because of the lower contact pressure. The optimal washer size was stated to be 18 mm for a 6 mm hole size. Much research was conducted to study the effect of lateral constraints from various washer sizes and clamp-up torques on bearing strength. This shows that there are many parameters to consider when developing a comprehensive understanding of bearing failure in composites.

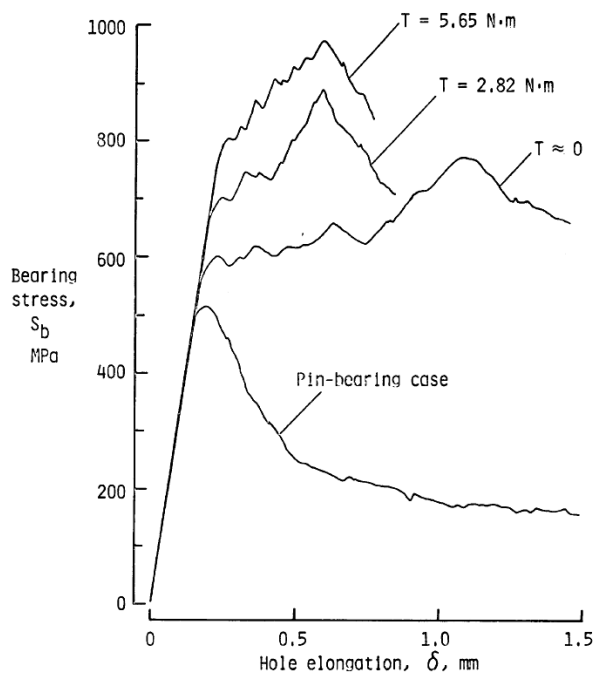

Figure 2.17: Effect of clamping pressure on bearing strength and hole elongation [16].

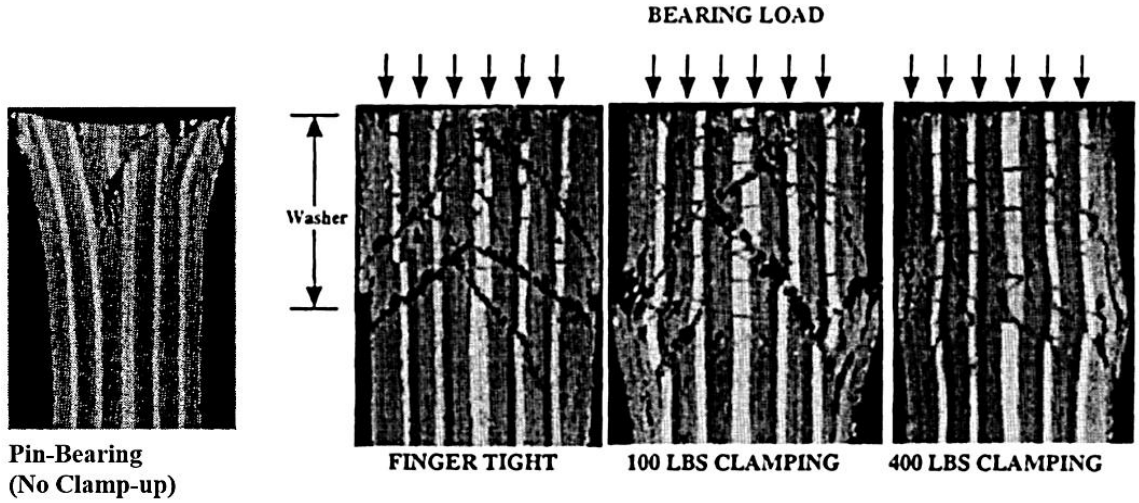

Figure 2.18: Optical microscopies of bearing damage in bolted joints with various clamping pressure [16].

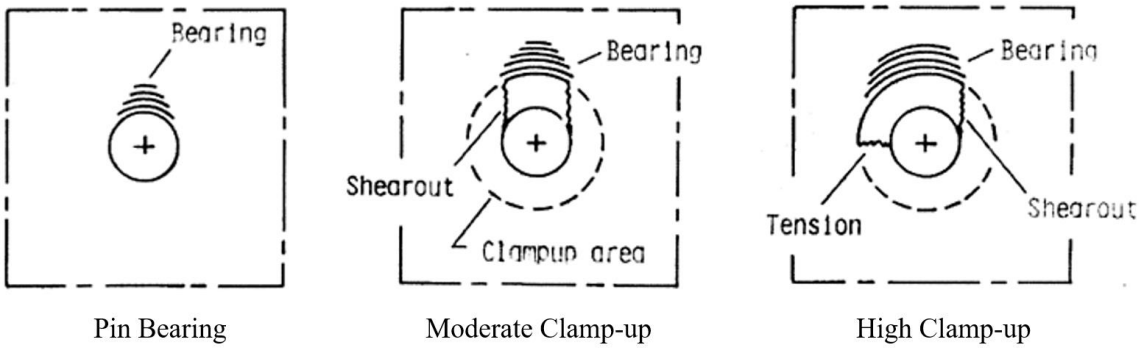

Figure 2.19: Bearing failure modes due to clamping pressure [16].

2.5 Effect of Composite Layup on Bearing Failure

Stacking sequence effect on bearing strengths were investigated and it was found that placement of certain plies can affect bearing strengths and failure modes of bolted laminates [4]. Irisarri et al. [21] studied three different layup orientations with increasing clamping force. The three laminates included quasi-isotropic, quasi-isotropic that is prone to delamination (high angle change 45°/-45° interface), and quasi-isotropic with 0°/90° interface. They concluded that bearing strengths of the quasi-isotropic layup is greater than the other two laminates because those laminates are more prone to delamination due to high Poisson ratio mismatch. The quasi-isotropic laminate with 0°/90° interface has the lowest bearing strength because there are more 90° plies than 0° plies and their interface is more likely to cause delamination. Quinn and Matthews [22] performed pin-bearing tests on glass fiber reinforced polymers with eight different stacking sequences and found that placing 90° plies at or near the surface of the laminate increases the bearing strength (see Figure 2.20). On the contrary, placement of 90° plies in the mid-laminate lowers the

bearing strengths. Laminates with 0° plies on the outer layers often fail in fiber splitting on the surface. Whereas, placing them in the interior of the laminate will show more delamination as the failure mode [23]. Wang et al. [16] and Park [24] also stated the same conclusions from their experimental research. In addition, Baba [25] studied the effect of having more 90° plies versus 0° plies and found that a layup of $[0/90/0]_s$ increases bearing strength by about 24% compared to $[90/0/90]_s$ (see Figure 2.21). The additional 0° ply increases the bearing strength. Although conclusions from these experimental studies show bearing strengths are affected by the stacking sequence, more research is necessary to develop a better understanding of how ply placements affect bearing strengths because there are wide variations in the stacking sequence of composite laminates.

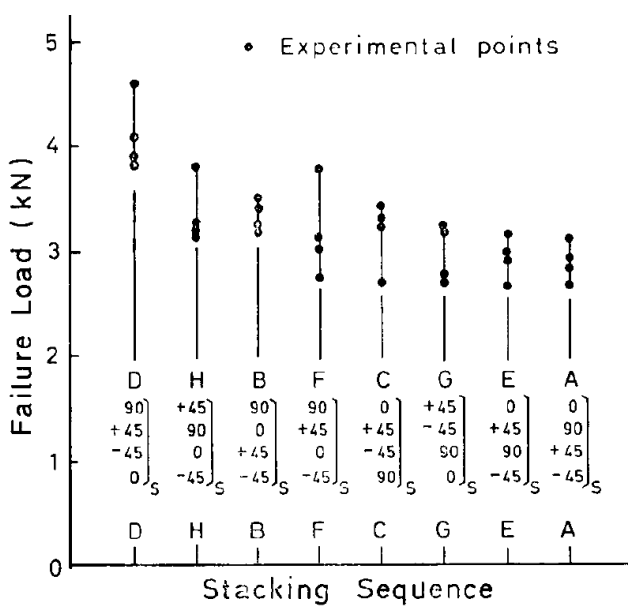

Figure 2.20: Effect of stacking sequence on bearing failure load [22].

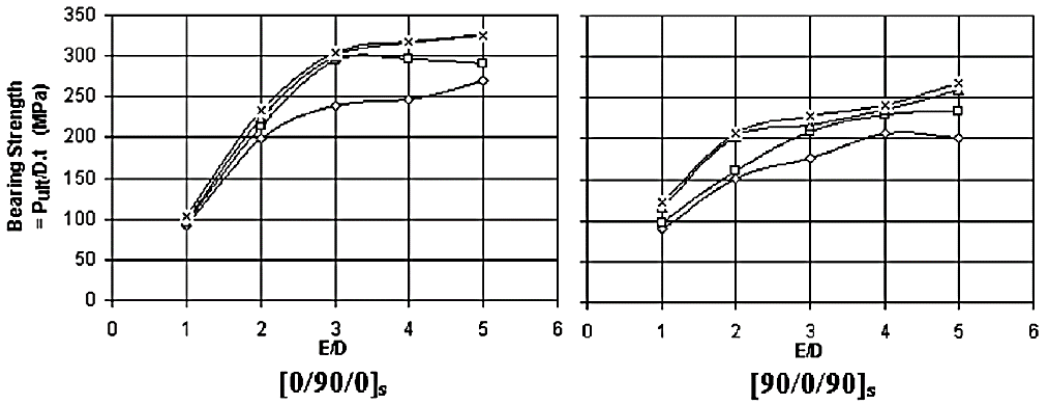

Figure 2.21: Effect of 0° plies versus 90° plies on bearing strength [25].

2.6 FATIGUE BEHAVIOR OF COMPOSITES

In an aircraft's lifetime, it experiences many flight hours, which is often converted to structural cyclic loading from take-off, in-flight maneuvers, fuselage pressurization, and landing. Every time a structure is loaded or unloaded, it can initiate and propagate damage around fastener holes. Common fatigue damage around the holes may include hole wear (material degradation), delamination, material erosion, and fastener yielding. An accumulation of fatigue damage can lead to a structural failure, which can be catastrophic if damage is undetected and/or unrepaired. Thus, it is not only critical to study composite bolted joint in static test, but also fatigue. Saunders D.S. et al. [26] experimentally performed fatigue tests on a thick graphite/epoxy laminate with two countersunk fasteners in a single lap joint configuration. They concluded erosion of matrix is caused by hole wear produced by movement of the bolt during cyclic loading (see Figure 2.22). Fastener movement was found to increase measurably throughout the

fatigue loading. Additionally, erosion of the matrix occurs most readily in the 0° ply orientation, because it is unable to redistribute stress laterally away from the fastener contact area. This leads to crushing of matrix and fibers (see Figure 2.23).

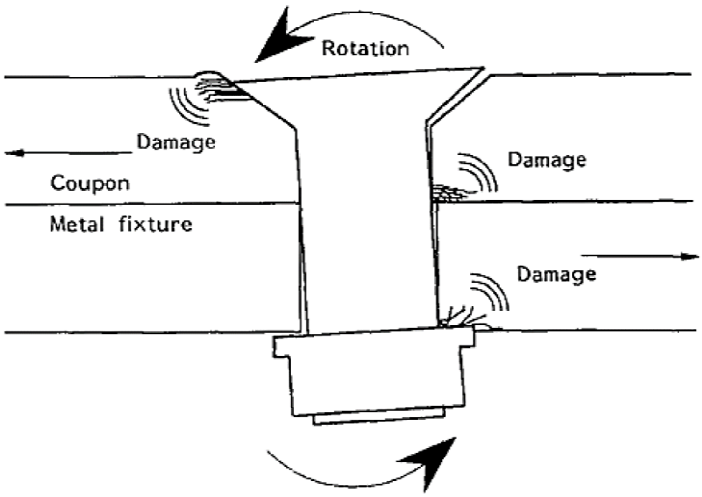

Figure 2.22: Movement of bolt during fatigue loading [26].

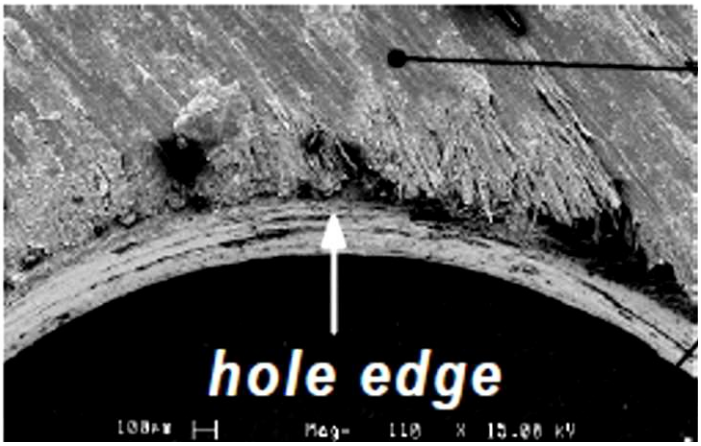

Figure 2.23: Hole wear caused by fatigue loading in composite bolted joint [27].

Sypt et al. [28] performed fatigue tests on a pin-bearing joint and characterized fatigue failure to occur in three stages. In the first stage, which consists of several thousand cycles, the asperities generated by the drilling process are detached from the hole surface and the stiffness of the joint is steady. As the number of loading cycles increase in stage 2, the mechanical damage and hole wear appears, which creates crushed particles of carbon fibers and matrix. Further increase in cycles would increase the area of the worn hole and decrease joint stiffness, leading to ultimate failure. During this time, a significant amount of energy is dissipated, which creates bearing damage (delamination, kink band and cracks) and increased hole elongation (see Figure 2.24). The three stages of fatigue failure is summarized in Figure 2.25, where (a) shows the hole surface when asperities are removed from the hole surface in the first thousand cycles, (b) shows the damage developed during the stabilized sequence and (c) shows the damage state at final failure.

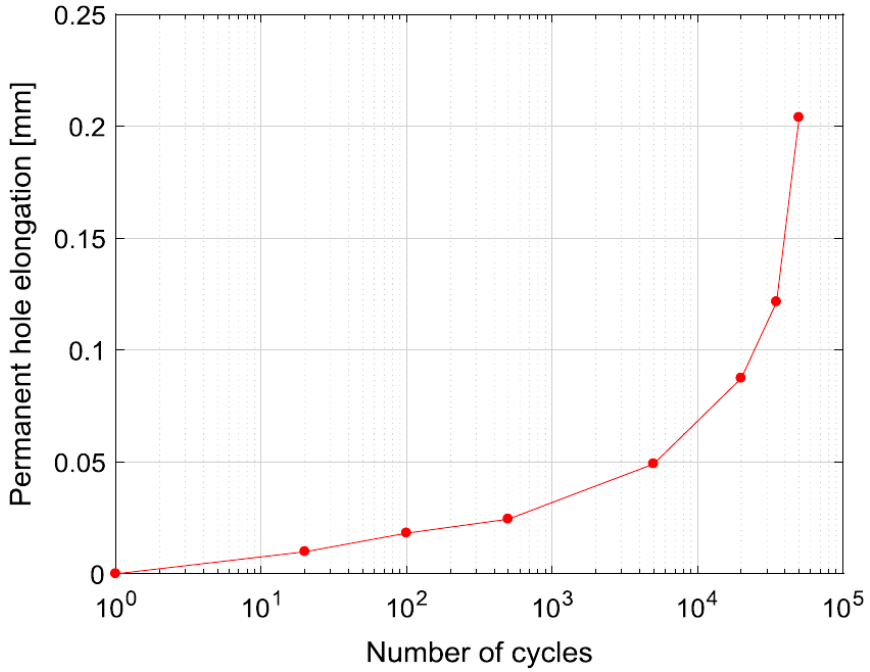

Figure 2.24: Hole elongation during pin-bearing fatigue test [28].

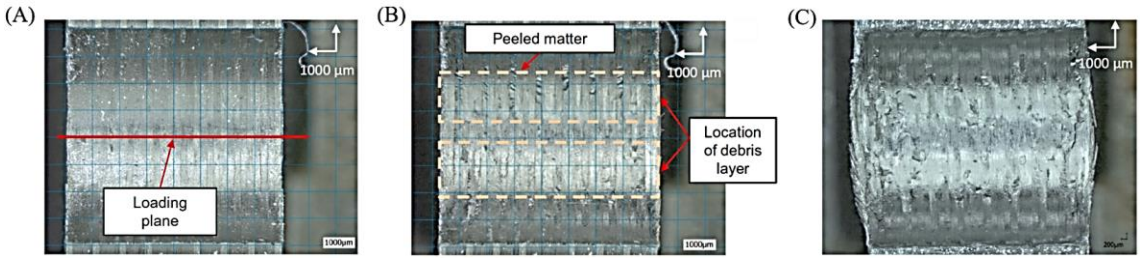

Figure 2.25: Fatigue test of pin-bearing failure sequence [28].

In summary, many parameters influence bearing strengths and damage morphologies. Some topics not discussed in this thesis, but that are also important to bearing failure are thermal effects, laminate thickness, loading types, and bolt-to-hole

clearance. All of the literature review discussed in this section provided important information on developing a deep-level understanding of bearing failure. Many studies indicated that delamination failure mode is observed in the development of bearing failure, but the formation and growth of delamination has not been fully understood. Therefore, the research presented in this dissertation project aims to establish quantitative and qualitative descriptions of the phenomena governing delamination behavior in bolted joints when subjected to fatigue loading.

3 EXPERIMENT TEST SETUP

Three different experiments were performed to develop a comprehensive understanding of bearing damage. Bearing failure in composite material is an accumulation of damage caused by compressive loading, which consist of matrix cracks, delamination, fiber fracture, and fiber kinking. Though these failure modes are related, the focus of this research is to understand delamination initiation and propagation.

The first experiment will be performed with a double lap shear (DLS) test configuration, which does not exhibit secondary bending compared to the single lap shear configuration (SLS). Additionally, this bolted joint will have a finger-tight torque of 0.5 N-m, which will not introduce clamping pressure effects on the joint. DLS is an ideal test setup to study bearing damage because the parameters that influence bearing strength can be isolated. A typical bolted joint that has a DLS configuration can be found joining sections of fuselage on an aircraft.

Results from DLS will be compared to the data from single lap shear (SLS) test configuration to study joint effect on bearing damage. SLS joints are more commonly found on an aircraft structure, such as in the assembly of wing sections and spar to fuselage skins. Bearing damage from DLS bolted joint are not the same as SLS due to the secondary bending effect and torque-up load. Thus, it is important to understand bearing damage behavior of this type of joint, in order to provide thorough information to assist engineers on aircraft future design, maintenance, and repairs.

Lastly, data found from cyclic loading of DLS specimens show pin bending may have an effect on bearing damage development. Thus, the semi-circular notched (SCN)

experiment was designed to study this phenomenon. Since the test setup and the geometry of the specimen is not typically found on an aircraft structure, it cannot be used to make conclusions on bearing strength. The results from this experiment will only be used to making conclusions on whether the pin affects delamination growth.

3.1 Specimen Design

The bearing specimens were fabricated using AS4/3501-6 carbon fiber-reinforced epoxy in three different 48-ply layups. Each of the three layups, have the same percentage of 0°, 90° and ±45° plies (see Table 3.1). The laminate labeled "Reference Laminate" was chosen as the baseline for all study cases. This was selected from an in-service aging aircraft wing layup design. The other laminates had their ply orientation rearranged such that in one laminate there were large groupings of 0° plies and in the other were large changes in angle between adjacent plies. These specimens have a single 9.53 mm bolt-hole located at an edge-to-hole diameter (E/D) distance of 4 for semi-circular notched and 4.6 for single and double lap shear specimens to avoid shear-out failure (see Figure 3.1). All holes were drilled, reamed and countersunk in one operation using the CNC milling machine. The quality was verified through visual inspection, C-scan and dye penetrate test. The conical height portion of the countersunk hole was machined to half the thickness of the specimen (see Figure 3.2). Double lap shear and single lap shear specimen overall dimensions were sized at 88.9 x 139.7 mm, whereas the semi-circular notched specimen was sized at 88.9 x 38.1 mm (see Figure 3.1).

Table 3.1: Bearing specimens layup information

Specimen Type	Layup	Thickness Range (mm)
Reference	$[\pm45/0_2/90/0_2/-45/0_2/+45/0/-45/90/0/+45/0/+45/0/-45/90/0/\pm45]_s$	7.26-7.76
Large 0° Groupings	$[\pm45/0_2/90/0_2/-45/0/+45_2/-45_2/0_2/90_2/0_4/+45_2/-45]_s$	7.23-7.65
Large Angle Change	$[\pm45/0_2/90/0_2/-45/+45/0_2/90/0_2/-45/+45/0_2/90/0/\pm45_2]_s$	7.22-7.58

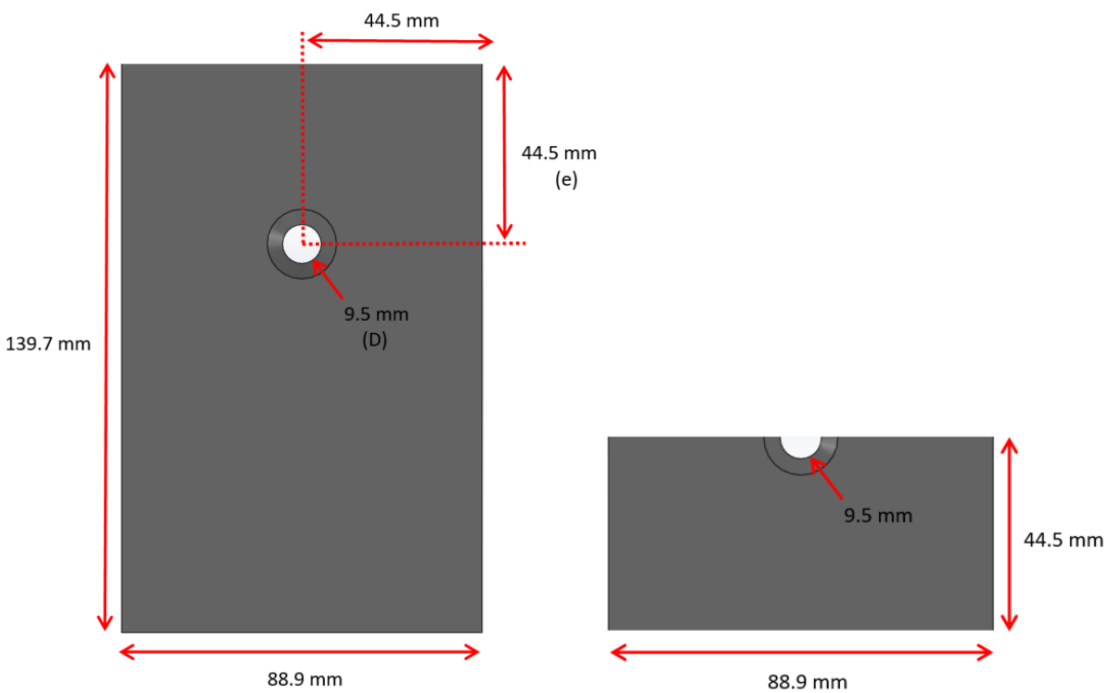

Figure 3.1: Bearing Specimens for DLS and SLS (left) and SCN (right).

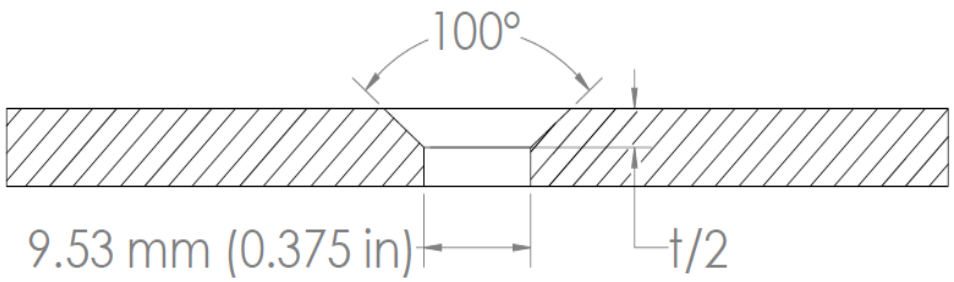

Figure 3.2: Bearing specimen cross-sectional view.

3.2 Composite Specimen Drilling

All composite holes were drilled, reamed and countersunk in one operation using a CNC machine. A portable vacuum with a hose extension was used in place of liquid lubricant to cool the tool and vacuum the carbon debris during the drilling process (see Figure 3.3). Liquid lubricant was not used since liquid can penetrate and be entrapped inside the composite if flaws (i.e., delamination and matrix burnt-out) develop during the drilling operation. Additionally, in the hole drilling set up, FR4 fiberglass was used as a backing material and replaced after completing each hole. This allowed the drill to penetrate through the fiberglass material each time the drill exits to prevent delamination. As concluded by researchers [9-11], flaws induced during the drilling process can reduce bearing strength and the composite's fatigue life. Thus, a study of tool pecking and feed and speed rates was performed to determine the most optimal procedure for drilling composites without creating fiber pull-out, matrix burn-outs, and/or delamination.

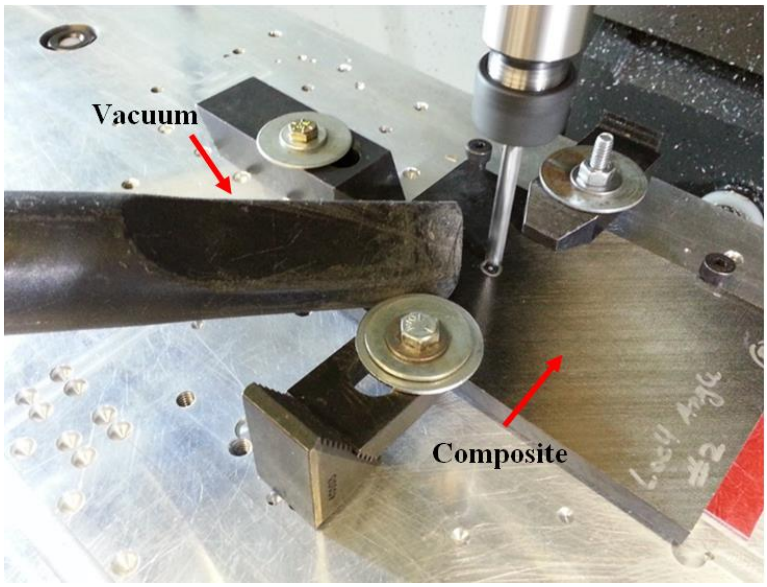

Figure 3.3: Composite hole drilling setup on the CNC millimg machine.

Every hole fabricated on the composite specimens used a titanium-nitride coated high speed steel drill bit, carbide-tipped tool steel reamer and titanium-nitride coated triangular carbide countersunk cutter (see Table 3.2). The drill bit removed the majority of the composite material (9.13 mm) and the reamer created the exact hole diameter of 9.53 mm. Since the drill removed most of the composite material, it dulled rapidly. Through experiment, it was concluded that the drill was only able to produce five quality holes before becoming dull. Thus, it is highly recommended to use a carbide tip drill to increase the life of the drill when drilling composite material. The conical region of the countersunk hole was carefully fabricated using a 100° degree angle countersunk cutter and cut to half the laminate thickness. Prior to drilling, each laminate was meticulously measured at the drill location to ensure that the conical depth would stop at mid thickness of the laminate.

Table 3.2: Tools used to dril, ream and countersink a 9.53 mm hole on all composite specimens.

Tools	Description	Supplier, Model #
	Short-length Drill Bit	McMaster-Carr Model # 2908A52
	Carbide-Tipped Round-Shank Reamer	McMaster-Carr Model # 3025A19
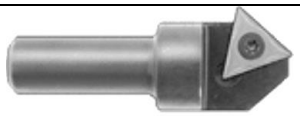	Replaceable Carbide-Insert Countersinks for 100 Degree Angle	McMaster-Carr Model # 29245A81
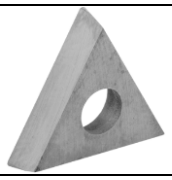	TiN Coated Triangle Carbide Insert	McMaster Carr Model # 29245A71

Upon selecting the optimal parameters to fabricate the countersunk holes, a few experiments were performed. The baseline of speed and feed rates for fabricating holes in composite material was provided by NAVAIR (see Table 3.3). However, following those parameters did not produce a desirable hole quality for the experiments performed in this research. Optical microscopy was performed to the finished hole and there was evidence of rough spots on the hole surface, which may indicate that the feed rate was too high (see Figure 3.4). The tool was traveling through the thickness of the laminate fast enough that the drill did not have time to cut the material to produce a smooth hole surface. In the second attempt, the speed rate was increased to 2100 rpm and the feed rate was reduced from 50.8 mm/min to 12.7 mm/min for the drill and countersunk cutter. The reamer speed rate was increased to 250 rpm and the feed rate was reduced to 6.4 mm/min (see

Table 3.4). The optical microscopy image shows a smoother finished hole surface but there were many gouges, which may indicate that the tool was overheating. When the tool becomes too hot, it can burn the matrix, causing gouges to the surface of the drilled hole (see Figure 3.5). Through these experiments and lessons learned, the parameters to drill, ream and countersink all tested specimens were developed (see Table 3.5). Overheating of the tool was resolved through implementing a pecking operation in the drill and countersink cutting, since this is where most of the material is removed. Optical microscopy and fluorescent dye penetrate tests were performed to verify hole quality (see Figure 3.6). Figure 3.7 shows that there are no gouges or delamination on the surface of the hole. Though the side of the laminate had large holes, it was not caused by the drilling process. Destructive sectioning of the specimen was performed using a wet tile saw to view the hole surface quality from the drilling process.

Table 3.3: Baseline drilling procedure for fabricating a countersunk hole on a composite laminate.

	Drill	**Ream**	**Countersink**
Speed Rate	2000 rpm	200 rpm	2000 rpm
Feed Rate	50.8 mm/min	50.8 mm/min	50.8 mm/min
Pecking Depth	No Pecking	No Pecking	0.076 mm

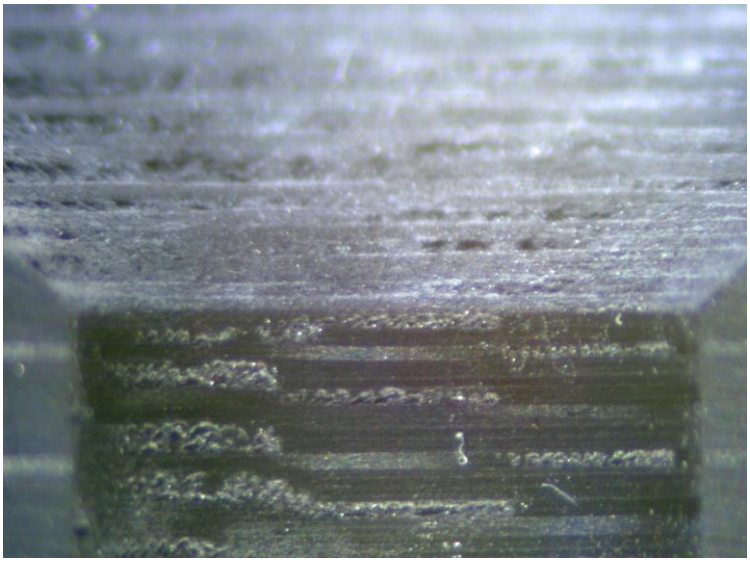

Figure 3.4: Optical microscopy image of a countersunk hole drilled from using the baseline drill parameters. Rough surfaces were created due to fast feed rate, which does not allow enough time for tool to cut the composite.

Table 3.4: Drilling procedure with increasing speed rate and decreasing feed rate.

	Drill	**Ream**	**Countersink**
Speed Rate	2100 rpm	250 rpm	2100 rpm
Feed Rate	12.7 mm/min	6.35 mm/min	12.7 mm/min
Pecking Depth	No Pecking	No Pecking	0.076 mm

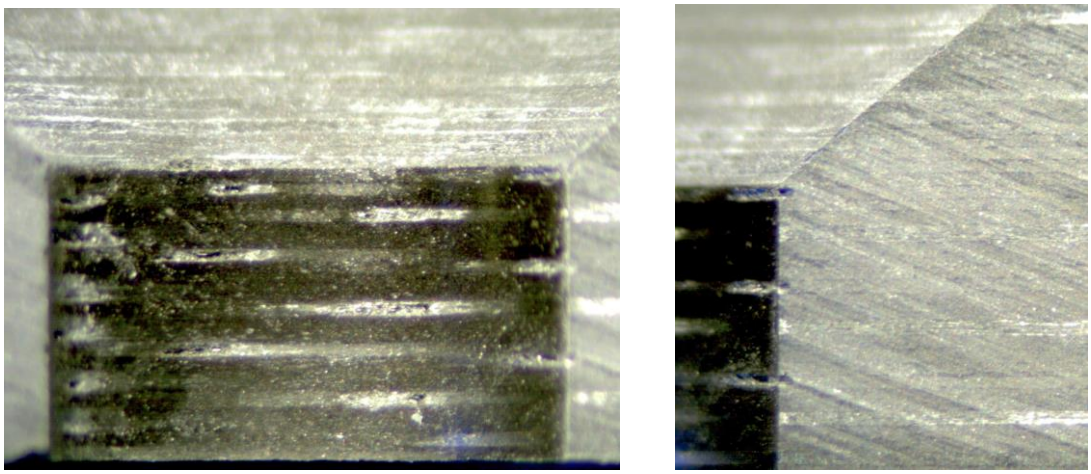

Figure 3.5: Optical microscopy of countersunk hole with slow feed rate. The tool overheats due to friction causing gouches from matrix burn-out.

Table 3.5: Parameters used to drill a 9.53 mm countersunk hole on all composite specimens using the CNC machine.

	Drill	**Ream**	**Countersink**
Speed Rate	2100 rpm	250 rpm	2100 rpm
Feed Rate	12.7 mm/min	6.35 mm/min	12.7 mm/min
Pecking Depth	0.254 mm	No Pecking	0.0762 mm

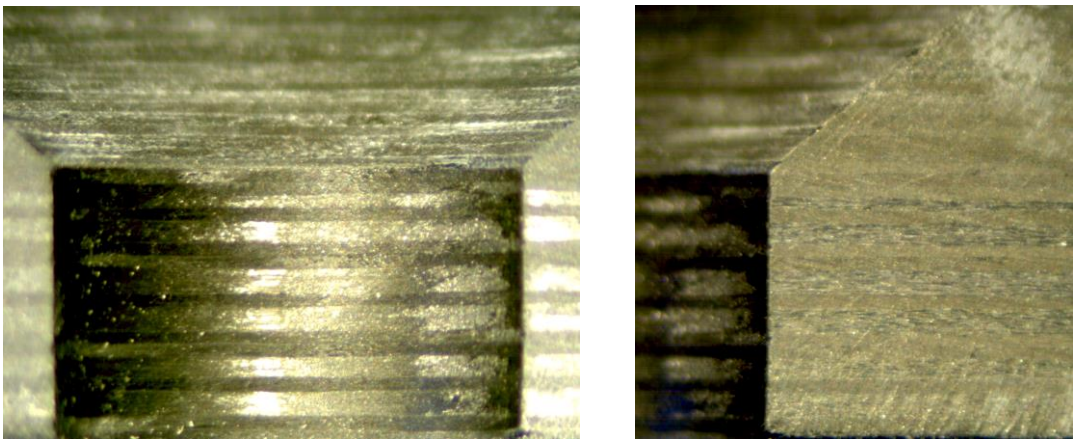

Figure 3.6: Optical microscopy of countersunk hole showing no flaws (i.e., delamination and gouges from matrix burnt-out). Drill parameters used to create this hole was used to fabricate all 9.53 mm countersunk hole for tested specimens.

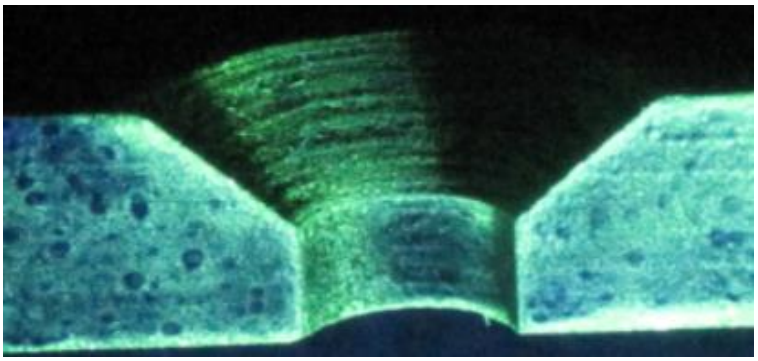

Figure 3.7: Flourescent dye penetrant test performed on the specimen that was fabricated with the optimal drill, ream and countersunk paraemters. No matrix burnt-out or delamination on hole surface. Gouges on the side of specimen was due to sectioning the specimen with a wet tile-saw.

Through testing the variations of drill parameters, it was found that pecking through the depth of the laminate during the drilling and countersinking prevents over-heating and gouges on the surface of the drilled hole. These tools can easily generate heat due to friction, particularly when drilling a thick laminate. Additionally, increasing the

speed and feed rates can reduce the contact time between the composite material, which may also help with over-heating of the tool. However, if the feed rate is too high and the laminate is thin or has no stiff backing material where the drill exits, then it may introduce delamination (see Figure 3.8). Detailed instructions on the drilling process for all holes fabricated in this research are shown in Appendix A.

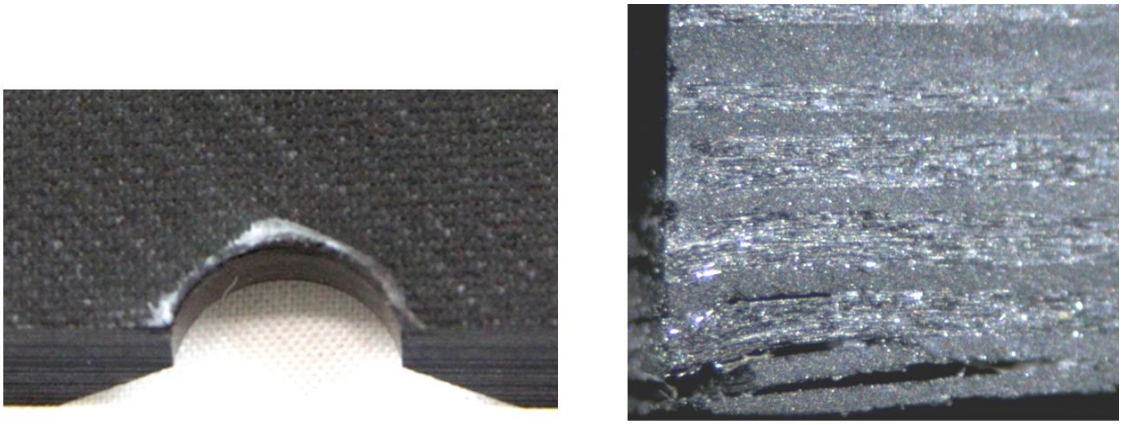

Figure 3.8: Delamination induced due to high drill feed rate and no stiff support where the tool exits.

3.3 Single Lap Shear (SLS) and Double Lap Shear (DLS) Test

The modified double lap shear (DLS) and single lap shear (SLS) test fixtures were designed based on the ASTM D5961, a standard test method for bearing response in polymer matrix composite laminates [3]. The DLS fixture was modified from the standard to use a custom-designed countersunk pin with a 9.53 mm diameter shank (see

Figure 3.9). The single lap shear test fixture used an off-the-shelf Hi-Lok fastener (HL21PB12-16), which has a 9.53 mm diameter shank and a countersunk head (see Figure 3.10). Both the DLS custom designed pin and bearing fixtures were fabricated using high strength 17-4 PH stainless steel. However, only the pin was heat treated to H900 to increase material strength. Detailed drawings are shown in Figure 6.1 through Figure 6.3 in Appendix B. The DLS final fixture and specimen assembly includes a double nut mechanism on both sides of the pin to prevent loss of the initial "finger-tight" clamping pressure prior to testing. This was applied using a torque wrench to ensure a uniform initial torque of 0.50 N-m for every specimen. The Hi-Lok fastener also used a double nut mechanism and a torque-up load of 45 N-m was applied. This load was selected based on the torque off load from the collar (HL86-12), which was designed to be used with the SLS Hi-Lok fastener. Replacing a new collar for each test is very costly, thus three collars were tested for the torque-off load and the average of them, which was 45 N-m, was applied to all the SLS experiments in this research. All static and fatigue experiments were performed on a 22 kip MTS hydraulic machine.

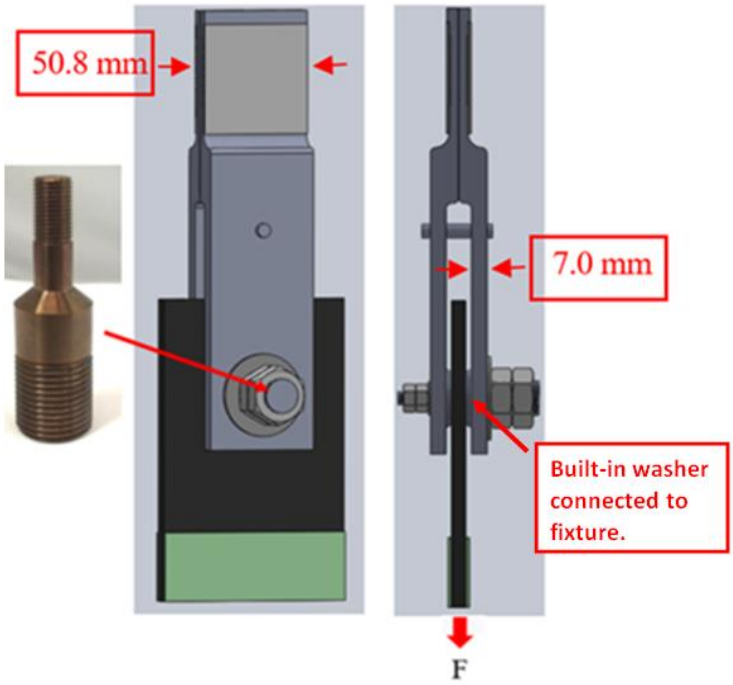

Figure 3.9: Double lap shear test configuration using a cusom designed countersunk bolt. A torque load of 0.50 N-m (finger-tight) was used in this setup.

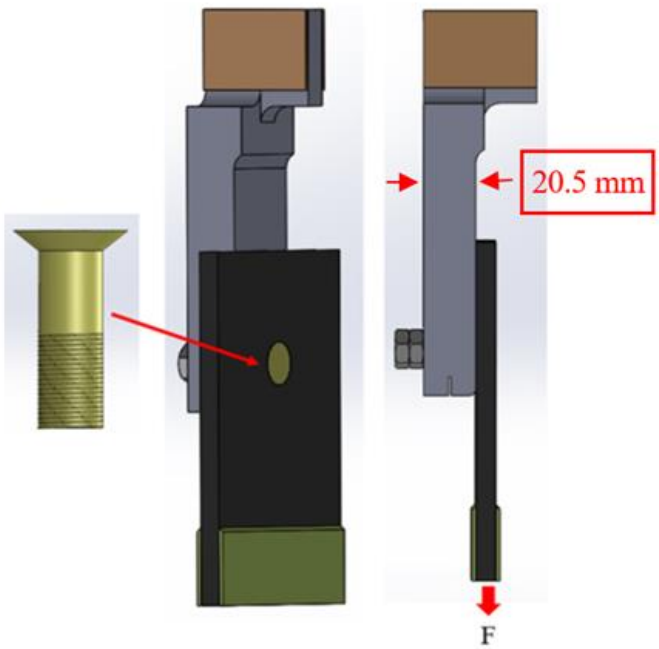

Figure 3.10: Single lap shear test configration with hi-lock fastener. Torque up load of 45 N-m was applied to this joint configuration.

Bearing static tests were performed for both DLS and SLS test configurations. All three laminate types were tested at a loading rate of 0.50 mm/min until the force versus crosshead displacement plot showed significant nonlinear behavior and then were unloaded. After testing, hole elongation was measured using a hole gauge and micrometer and a final destructive optical microscopy was performed (see Figure 3.11).

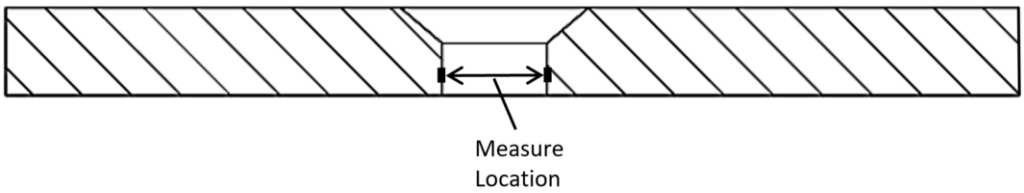

Figure 3.11: Location of where the hole elongation is measured using a hole gauge and micrometer. Measurements were taken three times and the averaged.

All DLS and SLS bearing fatigue tests began with a pristine specimen, where ultrasonic C-scans and initial static stiffness tests were performed prior to cyclic loading. Each specimen was statically loaded to the maximum load that it would experience during the fatigue test, in order to obtain the initial stiffness value and verify that the quality of hole would not cause strength reduction before testing. After the initial static test, the specimen was cyclically loaded for a desired number of cycles (e.g., 2,000 cycles) without disassembling it from the fixture. The fatigue test was performed under constant peak load (load control) at a stress ratio of 0.05 (tension-tension). Before removing the specimen from the MTS machine, another static test was conducted to measure the stiffness change value of the joint. Hole elongation was physically measured

using a hole gauge and a micrometer and then the specimen was ultrasonic C-scanned to monitor delamination growth. This fatigue procedure was repeated for several increments of cycles until there was significant hole elongation observed. Lastly, after all testing was complete, destructive sectioning and optical microscopy were performed.

3.4 SEMI-CIRCULAR NOTCH (SCN) TEST

Microscopy images from DLS experiments indicated that pin bending may influence delamination propagation in bearing failure. Thus, the semi-circular notch (SCN) experiment was designed to investigate the effect of pin bending on bearing damage. SCN specimens consist of a semi-circular hole that is either countersunk or through-hole (see Figure 3.12). A stainless steel dowel pin was bonded to a fixture along the length of the pin to provide a uniform compressive loading on the specimen (see Figure 3.13). Through the DLS experiment, it was found that the straight shank region of the countersunk hole carried most of the bearing load. Thus, a straight dowel pin was used to load both the countersunk and through-hole SCN specimen in the shank region only (see Figure 3.14).

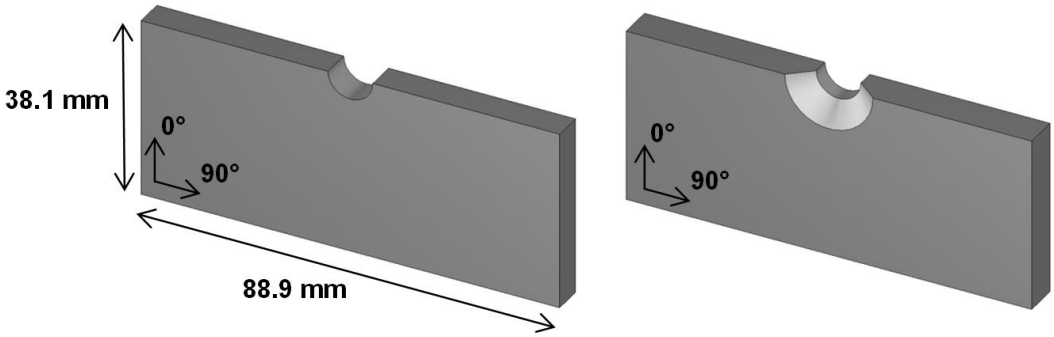

Figure 3.12: SCN through-hole and countersunk specimen geometry.

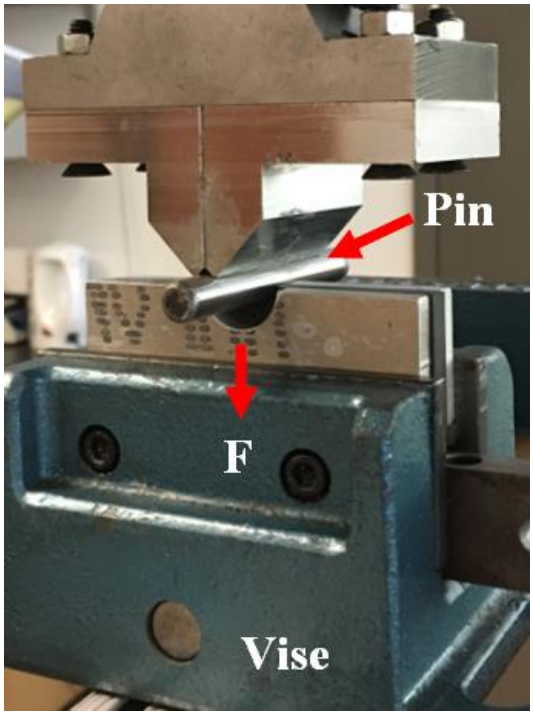

Figure 3.13: SCN specimen and fixture assembly for bearing test on the MTS machine.

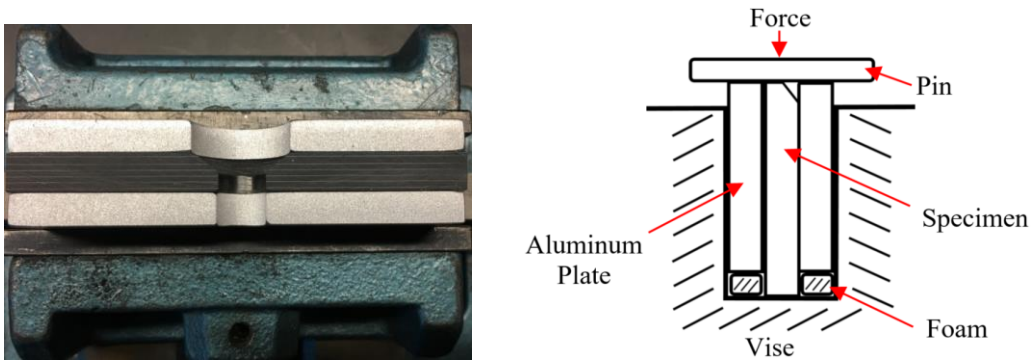

Figure 3.14: Top view (left) and side view (right) of SCN specimen and fixture assembly.

A total of 18 specimens were tested for the different laminate and hole types using a hydraulic MTS test machine. Two aluminum plates were placed on both sides of the specimen before inserting them into the vise, similar to the washers in the DLS fixture. In order to achieve the "finger tight" torque that was used in the DLS experiment, the vise was tightened such that the specimen and aluminum plates remained stationary, but could still move with a small amount of hand-applied force. The static load was applied at a rate of 0.50 mm/min until the force versus crosshead displacement plot reached an initial load drop, which defines the ultimate bearing failure load. Some specimens were loaded beyond this ultimate bearing failure load to study the progression of damage over displacement (i.e., large hole elongation). Prior to testing, each specimen was ultrasonically C-scanned to ensure there was no induced damage due to the drilling process. When the test was completed, all the specimens were C-scanned again to capture the delamination growth and then sectioned to perform optical microscopy.

3.5 NONDESTRUCTIVE INVESTIGATION (NDI)

The ultrasonic pulse-echo method was used as a nondestructive testing technique for all bearing specimens to detect defects in the composites. In this research, the ultrasonic C-scan system consist of a Mistras UPK-T10 automated tabletop scanner and an immersion tank with a scanning envelope of 254 mm length by 254 mm width (see Figure 3.15). The specimen was fully immersed in a water tank with a single immersion transducer, serving as both a transmitter and a receiver. For this particular transducer, the optimal focal length is one inch away from the scanning surface of the specimen. In the ultrasonic pulse-echo C-scan method, ultrasonic waves transmit through the thickness of the material and reflects back to the receiver when there is an inhomogeneity in the material, such as a flaw, or when waves reach the back wall of the specimen (see Figure 3.16). The immersion transducer used was a 12.7 mm diameter, 5 MHz spherical focused longitudinal wave transducer (Mistras Group Inc., Part # IU5G2) that uses water as a couplant. There are typically three forms of immersion transducers including unfocused, spherically focused, and cylindrically focused. The spherical focus transducer was used because it can improve detection of small flaws compared to the other types of transducers. Detailed C-scan settings when using this particular transducer are shown in Appendix C.

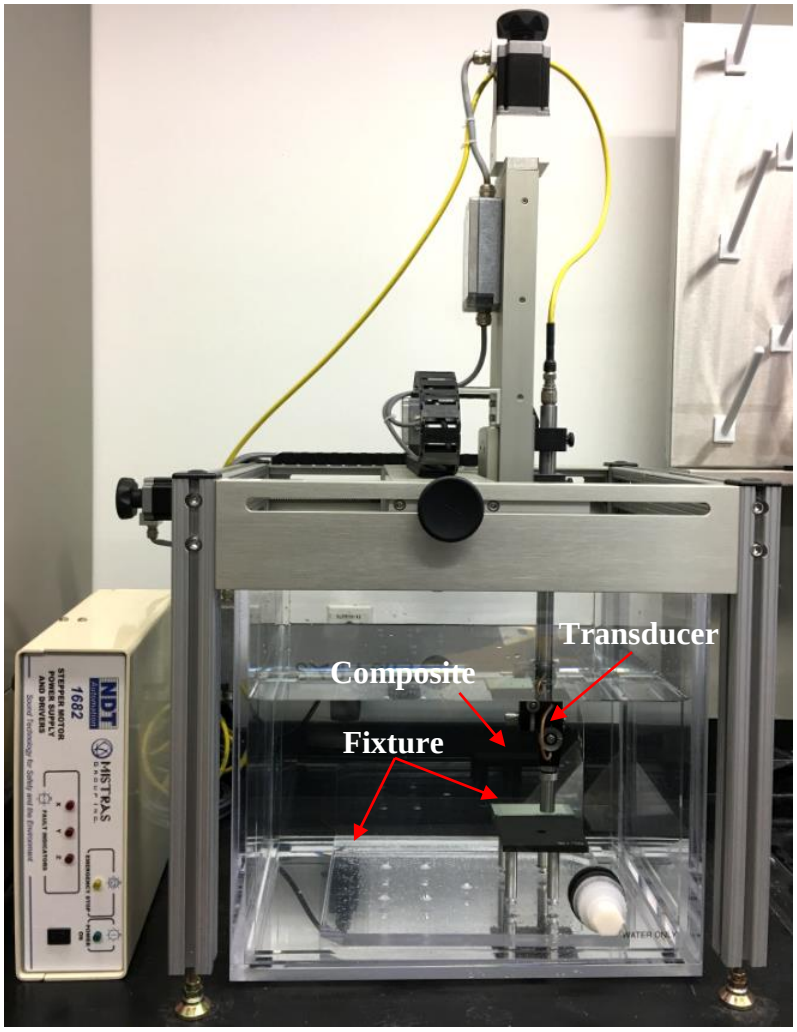

Figure 3.15: Ultrasonic C-scan system.

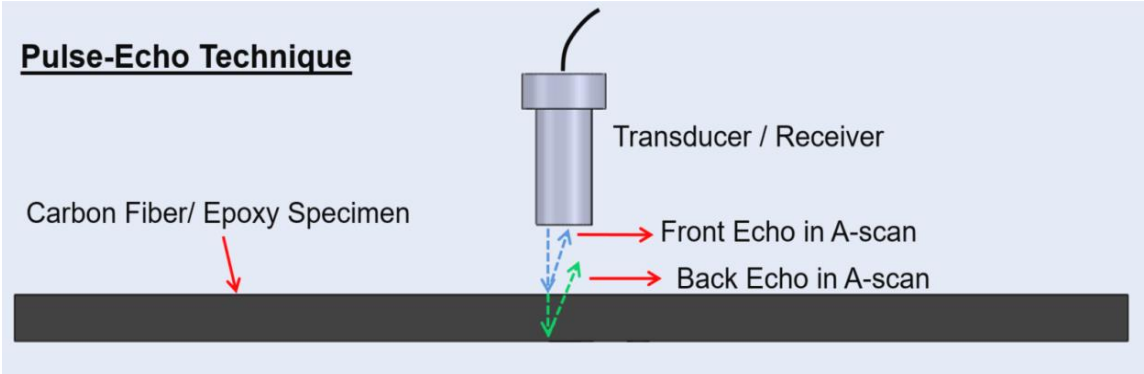

Figure 3.16: Ultrasonic pulse-echo technique.

Data acquired from the pulse-echo method produces A-scan plots based on the time-of-flight (TOF), material velocity (V_L) and material thickness (D) (see Figure 3.17). Equation 3.1 was used to determine the location of flaws through the thickness of the specimen. When there is a flaw in the material, ultrasonic waves reflect sooner than when it travels through the entire thickness of the material (i.e., no flaw) before reflecting back to the transducer. A collection of A-scan plots produces a C-scan image, which was used to visualize flaws in a 2D view of the specimen area (see Figure 3.17). Thus, an A-scan plot represents a single pixel on the C-scan. Each color on the C-scan image represents a different thickness in units of inches, thus providing information on flaw size and location. When ultrasonic waves reflect one wave or have no wave reflection, then the C-scan image define it as missing data points. In this research, all C-scan images showing white color near the hole edge indicates loss of wave signal reflecting back to the transducer and black color for water.

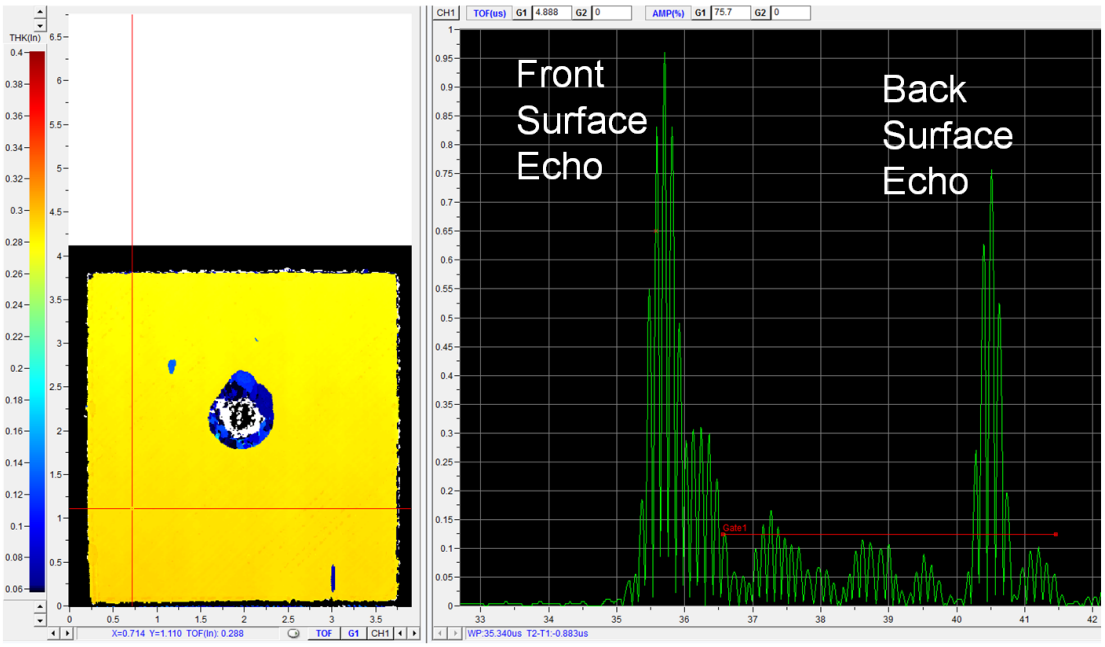

Figure 3.17: C-scan (left) and the corresponding A-scan (right) for one pixel on the C-scan image.

$$D = V_L \times \Delta TOF \tag{3.1}$$

3.6 MTS Hydraulic Test Setup

All static and fatigue bearing tests were performed at the University of California San Diego using a 22-kip capacity MTS hydraulic test machine. All static tests were performed under displacement control at a rate of 0.50 mm/min and unloaded upon reaching the desired load. Specimens were unloaded to near zero load before removal from the test machine to perform ultrasonic C-scanning. For fatigue bearing tests, the MultiPurpose TestWare (MPT) software was used to program both cyclic loading and the

stiffness check in one continuous test procedure. Detailed procedure for performing this experiment is shown in Appendix D. Before beginning the fatigue test, the specimen and fixture assembly was inserted into the MTS machine and the load cell was set to zero. This ensures the gripping pressure does not generate pre-load to the bolted joint prior to testing. After gripping, the specimen was gradually pre-loaded to 50% of the peak load. All fatigue bearing tests were performed using load control at a stress ratio of 0.05 (tension-tension). After reaching the pre-set number of cycles, the MPT software stopped at the average force and decrease load to near zero before beginning the stiffness check. The stiffness check was a static test, where the same specimen was loaded to the maximum cyclic load and then unloaded. The slope of the load versus crosshead displacement is determined to be the current stiffness of the joint. Figure 3.18 illustrates the test procedure for performing cyclic loading. All fatigue tests were cycled until either reaching 4 times a typical aircraft life cycle (defined as 30,000 cycles per one life time), bearing failure, or if there was no significant growth of delamination observed from C-scan images.

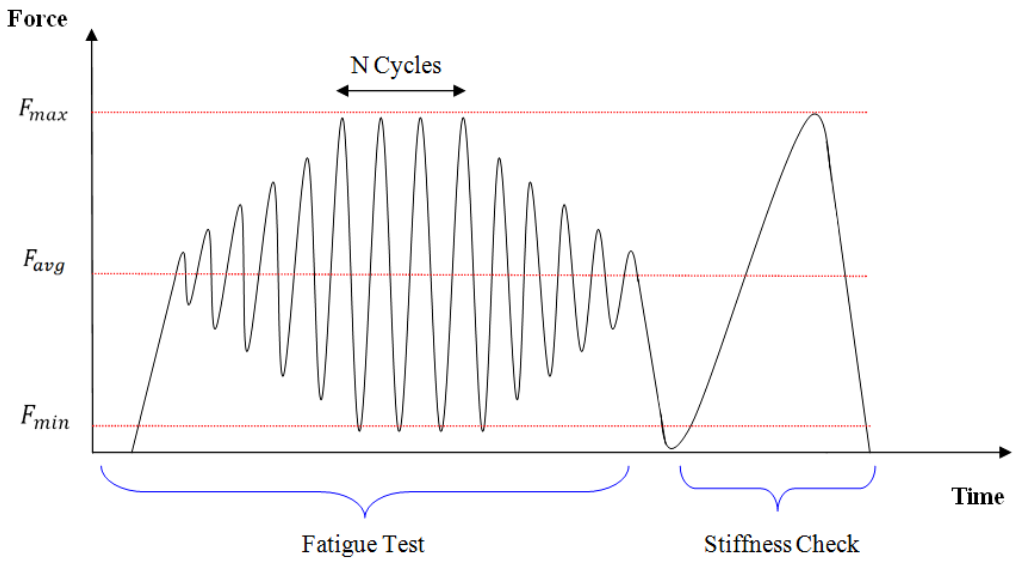

Figure 3.18: Illustration of cyclic loading procedure.

Chapter 3 includes material as it appear in the Investigation of Delamination and Growth Behavior at Fastener Locations in Primary Composite Structures, 2017. Ngo, Mimi and Kim, Hyonny, Proceedings of the 32nd Annual American Society for Composites Technical Conference, 2017 and A Comparative Study on Pin Bearing Effect Under Bearing Static and Fatigue Failure, 2018. Ngo, Mimi and Kim, Hyonny, Proceedings of the 33rd Annual American Society for Composites Technical Conference, 2018. The dissertation author was the primary investigator and author of this paper.

4 EXPERIMENTAL RESULTS

4.1 BEARING STRENGTHS

Static bearing tests were performed for both double lap and single lap shear test configurations to understand the effect of joint configuration on bearing strength and damage morphologies. Bearing failure of composite materials is a complex phenomenon, thus studying the damage morphologies may assist in determining the root causes for bearing failure and thus permit accurate models to developed. A series of DLS static tests were performed to investigate damage at low, mid and ultimate bearing failure load levels. At the low bearing load level, joint stiffness remains linear, which is shown in the joint load versus crosshead displacement plot (see Figure 4.1). Specimens tested to mid load were stopped when the plot became nonlinear before reaching ultimate failure load. The onset of bearing damage was determined through a 5% deviation from the linear fit line from the bearing stress versus crosshead displacement data (see Figure 4.2). This criterion was chosen based on experimental results, where static tests were stopped when the bolted joint began to lose its stiffness by 2-5%. Bearing stress was calculated using Equation 4.1, where *P* is the applied load, *k* is force per hole factor (1.0 for single-fastener), *t* is the total thickness, and *D* is the diameter of the bolt. In this equation, it was assumed that the shank region carried most of the load, thus the thickness was multiplied by one-half.

$$\sigma_{brg} = \frac{P}{k \times D \times \frac{t}{2}} \tag{4.1}$$

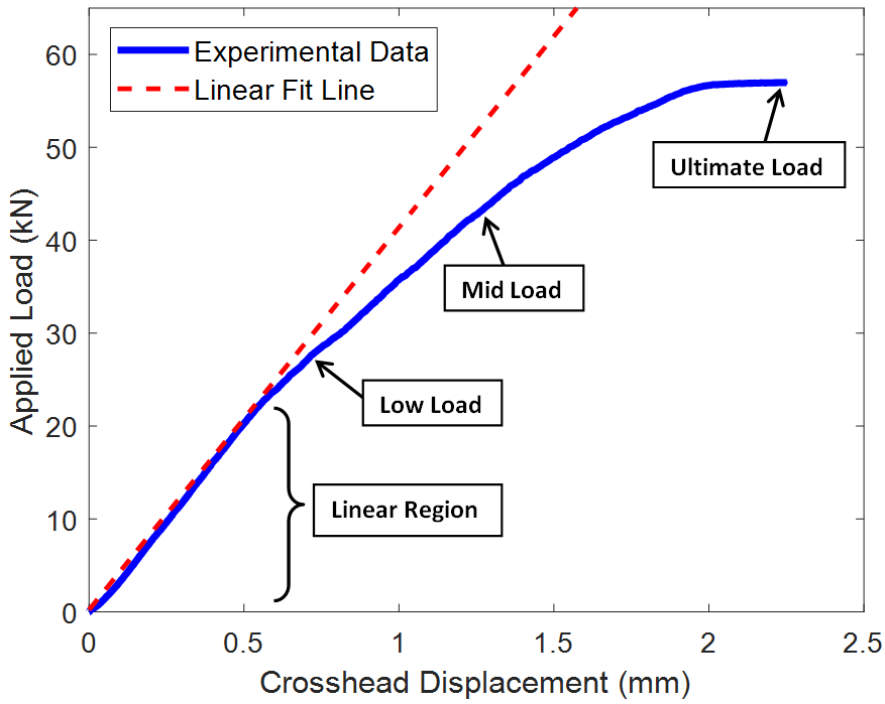

Figure 4.1: Typical bearing load vs. displacement plot form a static test. Load level definitions used to study progressive damage of composite specimens are indicated.

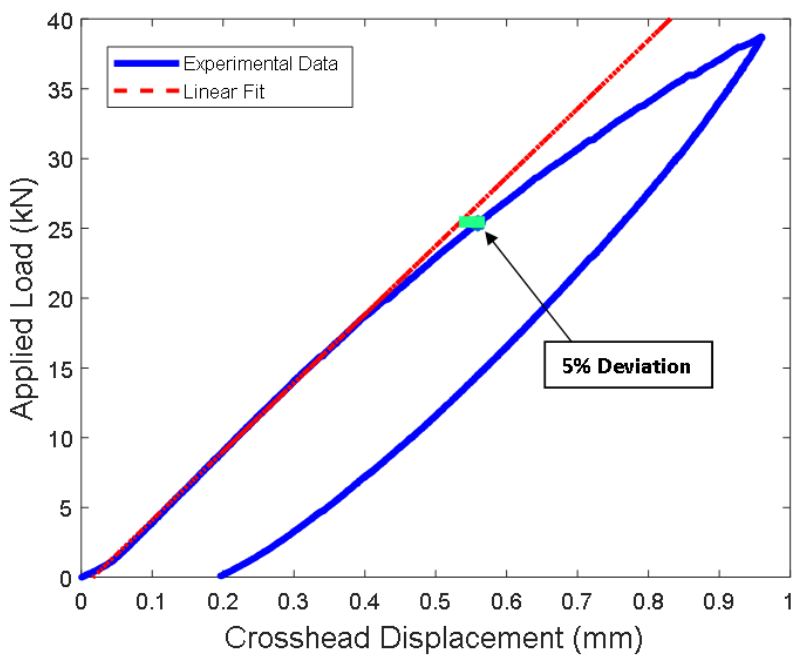

Figure 4.2: Onset of bearing damage defined by 5% deviation from the experimental results.

4.2 BEARING PROGRESSIVE DAMAGE OF COMPOSITE MATERIALS

Progressive damage of bearing failure in composites was studied through the double lap shear test configuration. Three specimens from each laminate types were loaded to low, mid, and ultimate loads and optical microscopy were performed. Bearing stress versus crosshead displacements were plotted for each laminate types at each load level. Applying low load to the specimen provide information on bearing damage initiation, whereas the mid load demonstrates damage progression before leading to ultimate failure. Specimens tested at low load were stopped when there was a slight decrease (~2-5%) in joint stiffness (see Figure 4.1). The initial joint stiffness was calculated as the slope of the applied load versus crosshead displacement in the linear region.

Figure 4.3 shows results plotted from the reference laminate type at these different load levels. The joint stiffness for the specimen tested at a low bearing load is about 8% greater than the one tested at ultimate bearing load. On the contrary, the other two laminate types have slightly lower joint stiffness when the specimens experience low load compared to ultimate load. Figure 4.4 shows results from static testing of three specimens with large groupings of 0° plies. Their joint stiffness are all within 5% difference from the largest to smallest change in stiffness from the same laminate type. Figure 4.5 shows the specimen with large change in angle plies. Specimens tested at the mid and ultimate loads were unloaded at the same load levels even though it was following the criteria for when to end the experiment (see Figure 4.1). This may be caused by the difference in the joint stiffness. Since the specimen tested at mid level is

stiffer than the one tested to ultimate load, the joint was able to carry a greater load before exceeding linear region of the load versus crosshead displacement plot. Table 4.1 tabulates all of the initial joint stiffness from the static test for all laminate types. Table 4.2: Peak load applied to the static DLS test specimens Table 4.2 summarizes the loads applied to each of the specimen types for the low, mid, and ultimate load categories. These values vary because each test was unloaded manually based on the applied load versus crosshead displacement plot provided by the MTS software during the experiment.

The small variations in the joint stiffness may be due to using a new specimen for each test, thus there can be slight variation in the manufacturing process that can influence the joint stiffness (i.e., laminate thickness). Another possible cause may be the slight change in clamping pressure. Although a torque wrench was used in an attempt to apply constant finger-tight clamping pressure on the bolted joint for all experiments, there may be some slight variation when the specimen and fixture assembly are placed in test machine. Since the clamping pressure is very low, the specimen could have moved a little while gripping pressure from the test machine was applied.

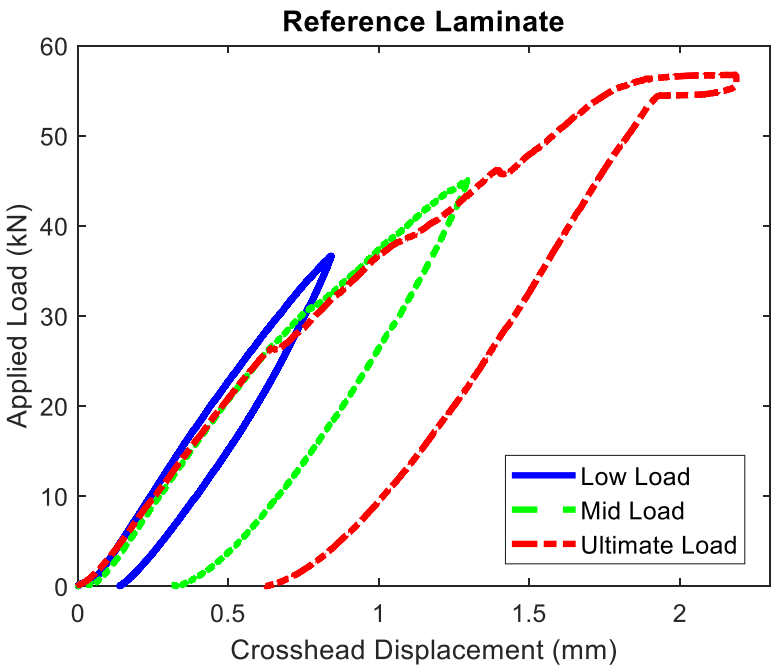

Figure 4.3: DLS static test of three Reference laminate tested at low, medium and ultimate loads.

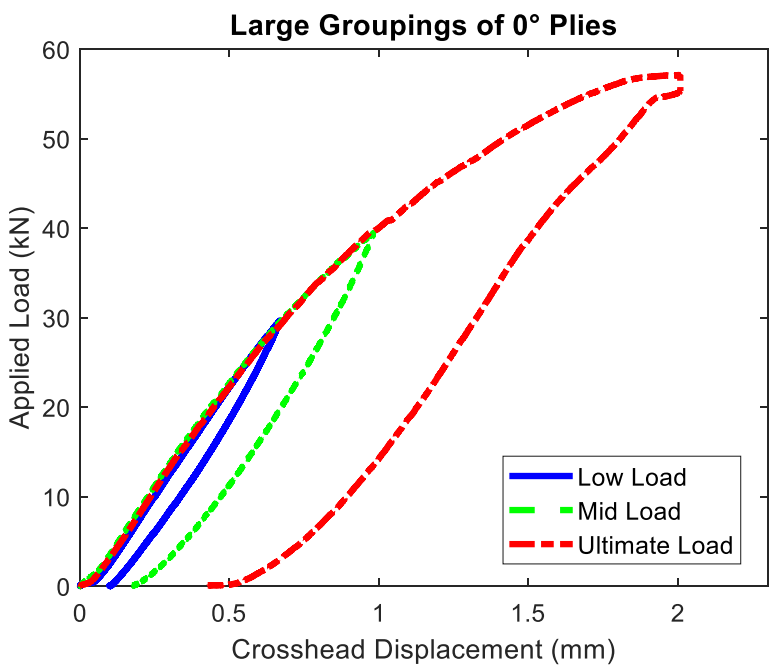

Figure 4.4: DLS static test of three laminates from the specimen type with large groupings of 0° plies tested at low, medium and ultimate loads.

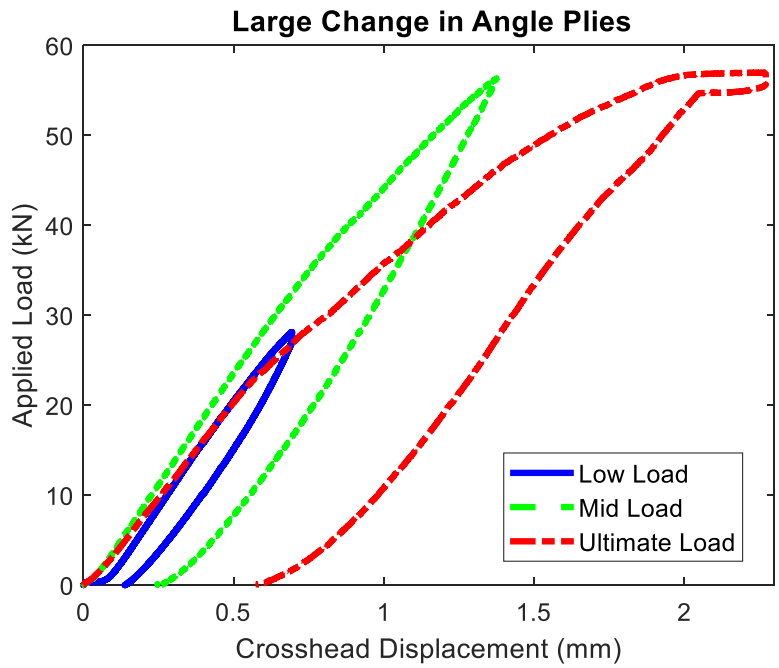

Figure 4.5: DLS static test of three laminates from the specimen type with large change in angle plies tested at low, medium and ultimate loads.

Table 4.1: DLS joint stiffnesses from static tests.

	Bolted Joint Stiffness		
Specimen Types	**Low Load**	**Mid Load**	**Ultimate Load**
Reference Laminate	45.0 kN/mm	40.5 kN/mm	41.3 kN/mm
Large Groupings of 0° Plies	43.5 kN/mm	45.9 kN/mm	44.9 kN/mm
Large Change in Angle Plies	39.8 kN/mm	46.4 kN/mm	40.4 kN/mm

Table 4.2: Peak load applied to the static DLS test specimens.

	Peak Load Levels		
Specimen Types	**Low Load**	**Mid Load**	**Ultimate Load**
Reference Laminate	36.7 kN	45.1 kN	56.8 kN
Large Groupings of 0° Plies	28.6 kN	39.4 kN	57.1 kN
Large Change in Angle Plies	28.1 kN	56.4 kN	56.9 kN

Optical microscopy performed on all static specimens were sectioned at a plane passing through the center of the bolt-hole and along the 0° plies, in the direction of loading (see Figure 4.6). A summary of these microscopies are shown in Figure 4.7. Each image represents a new tested specimen with damage accumulation from applying low, mid, or ultimate load levels for each of the specimen types. The columns represent the different load levels that the specimen experienced and the rows show the different laminate type that were investigated.

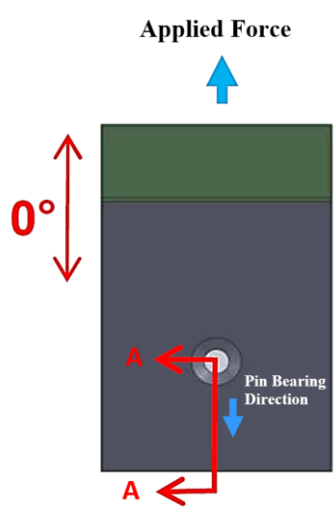

Figure 4.6: Schematic view of microscopy sectioning.

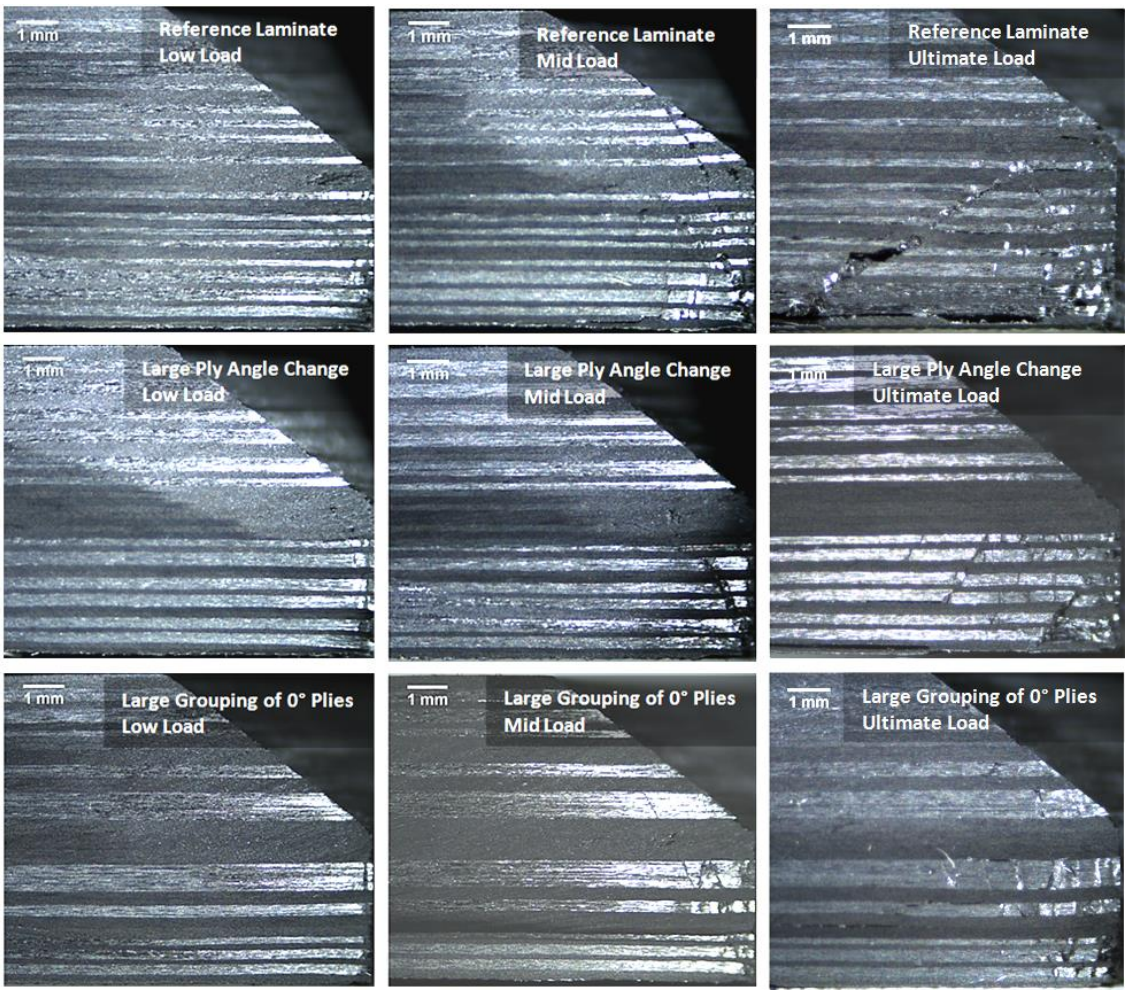

Figure 4.7: Optical microscopies of DLS static specimens tested at low, mid and ultimate failure loads.

For all specimen types, it was observed that the majority of bearing damage accumulates in the shank region of the bolted hole, which corroborates the assumption made when calculating bearing stress (see Figure 4.7). Equation 4.1 only takes into account half of the laminate thickness, which represents the shank region. Additionally, shear cracks grow in the conical countersunk section and the outer surface of the laminate with increasing loads. At a low load level, it is evident that fibers fail due to fracturing at the bolt-bearing surface, where cracks form perpendicular to the laminate through-

thickness direction (see Figure 4.8 through Figure 4.10). This can be observed for all three laminate types, indicating that matrix cracks initiates after the load versus displacement plot deviates from its linear region and cause the fibers to fracture. These fiber fractures do not shear in a diagonal direction or deeper in the length of the composite in the bearing direction, compared to the fiber fractures that occur at a higher load (see Figure 4.11 through Figure 4.13). When increasing the applied load, matrix cracks propagate through the length of the specimen, in the direction of pin bearing and cause a longer length of fiber to become unsupported. Thus, the combination of compressive loading and the naturally misaligned fibers, will lead to micro-buckling of the fibers causing it to shear. This phenomenon is known as fiber kinking. A group of fibers kinking in one region of the laminate is known as a kink band. When the specimen is initially loaded, the matrix crack is extended to a small distance on the very edge of the hole, thus fibers are unlikely to buckle. Additionally, it was observed that matrix cracks grows toward the interface of the fibers and arrest, initiating delamination. Delamination is often found to occur between the interfaces where there is a change in angles due to the Poisson's ratio effect [21]. When specimens are tested to ultimate load, it is more visible where delamination initiates and propagates due fiber fracture (see Figure 4.14 through Figure 4.16). Once the fibers fracture, the bearing loads are carried by the adjacent fibers. The bright silver lines in all the microscopy images are the 0° plies and the adjacent plies are either the 90° plies or a ±45° ply. Fiber fracturing causes a discontinuous load transfer in the direction of loading, thus a hypothesis is that some of the load spreads to the neighboring plies, pushing outwards from the fiber direction (see Figure 4.17). This may cause delamination to initiate and with greater load, it would propagate. From these

microscopy images, it can be concluded that fiber fracture, fiber kinking and matrix cracks were the main failure mechanisms observed at the boundary of the bolted hole.

Damage in the specimen that have large groupings of 0° degree ply was not as severe as compared to the other two specimen types (see Figure 4.14 through Figure 4.16). Since the 0° degree plies carried majority of the applied stresses, the larger groupings of 0° plies provide a higher local stiffness compared to a single 0° degree ply. The reference type specimen has smaller groupings and wider distributions of the 0° degree plies, which has lower local stiffness and result in having the greatest damage accumulation. The local compressive loads and inter-laminar stresses cause shear cracks to occur through the thickness of the laminate. Due to the complex nature of composite laminates, the direction of these shear cracks can vary significantly, as shown in Figure 4.11 and Figure 4.14, where the reference laminate with mid and ultimate load levels show different directions of shear cracks. The specimen with a large change in angle plies have larger sections of 0° degree plies on the bottom of the shank region, thus the shear cracks do not propagate upwards towards the conical section of the specimen. This indicates that matrix cracks often branch in the direction of the stiffer region through the thickness of the specimen, and are likely not bridging across the relatively thick set of non-zero degree plies at the specimen center.

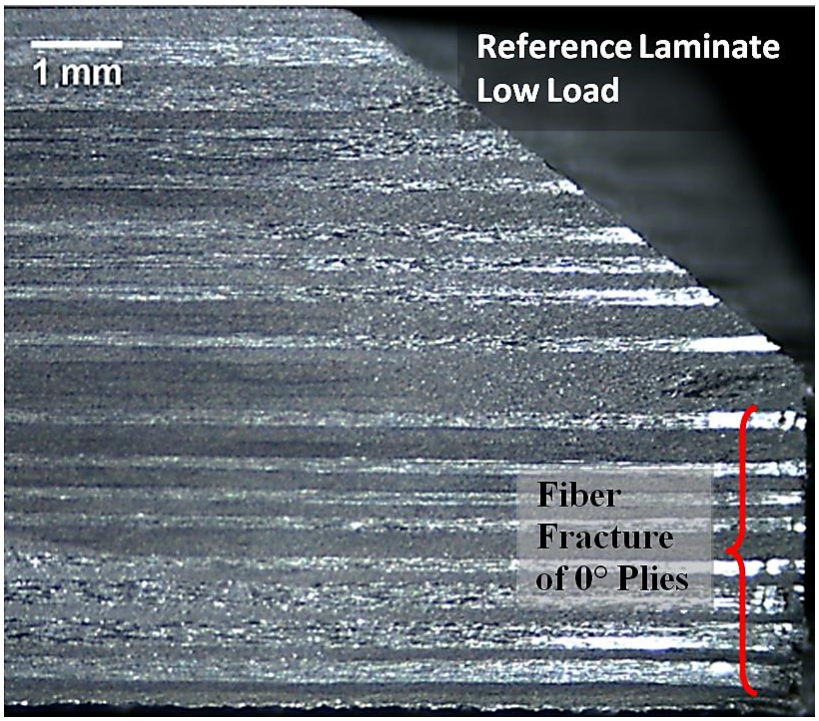

Figure 4.8: Microscopy of the DLS specimen from the reference laminate after loaded to low load (28.6 kN).

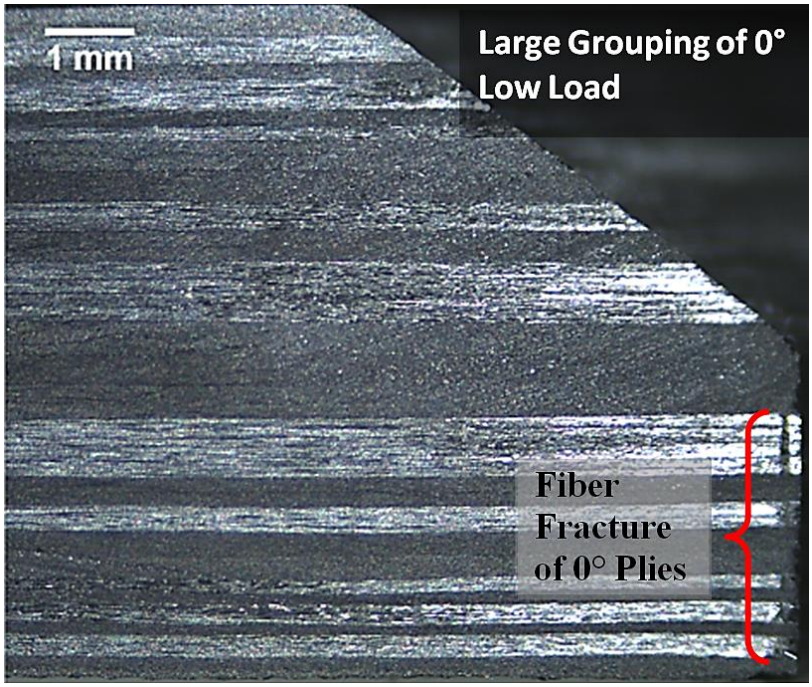

Figure 4.9: Microscopy of the DLS specimen with large grouping of 0° plies after experiencing low load (36.7 kN).

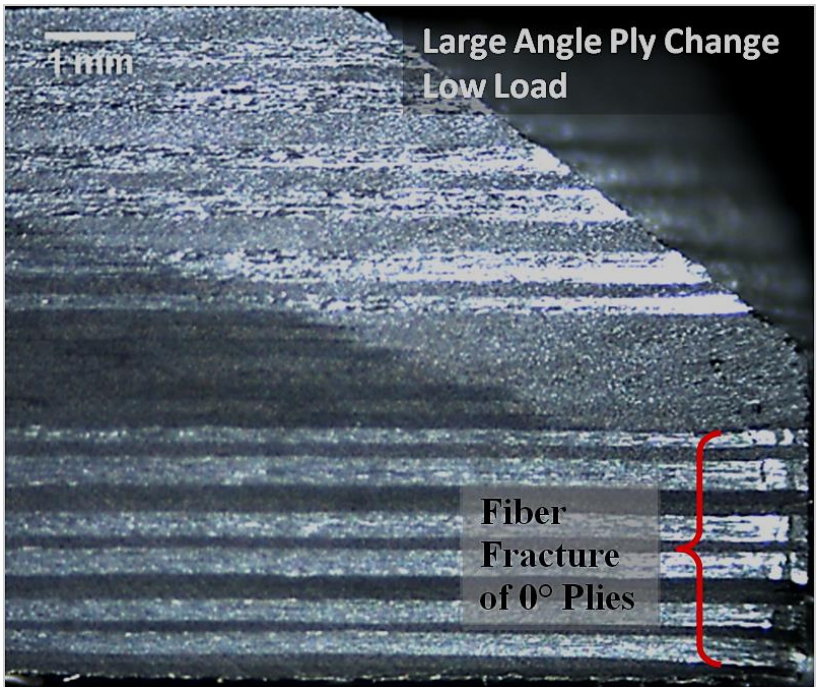

Figure 4.10: Microscopy of the DLS specimen with large change in angle plies after experiencing low load (28.1 kN).

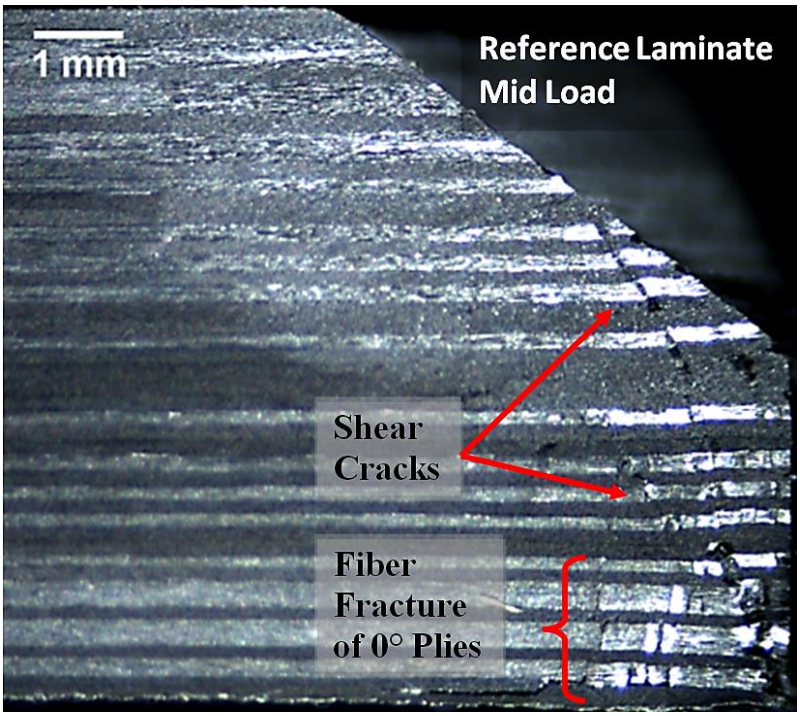

Figure 4.11: Microscopy of the DLS specimen from the reference laminate after stopping the experiment at mid load (45.1 kN).

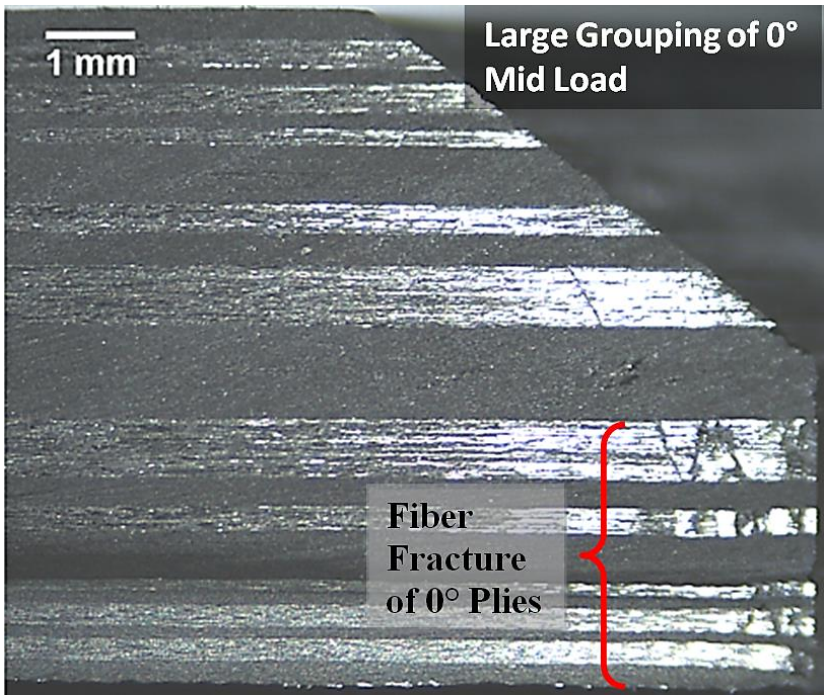

Figure 4.12: Microscopy of the DLS specimen with large grouping of 0° plies after experiencing mid load (39.4 kN).

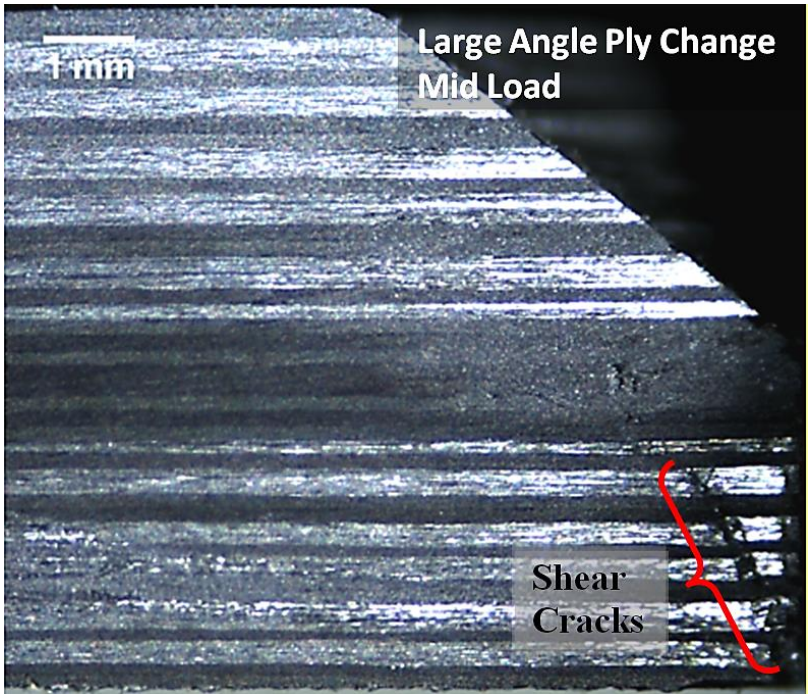

Figure 4.13: Microscopy of the DLS specimen with large change in angle plies that was stopped at mid load (56.4 kN).

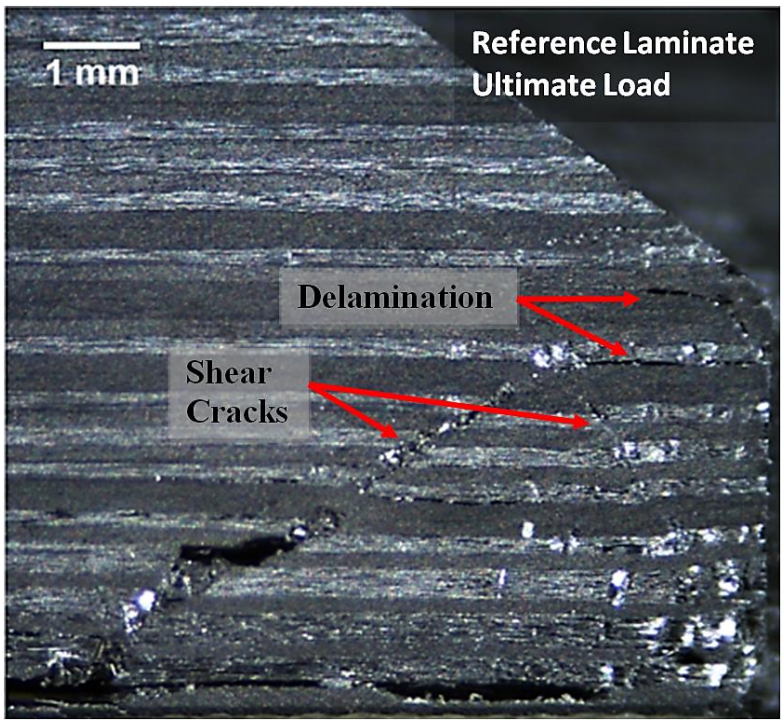

Figure 4.14: Optical microscopy of a DLS specimen from the reference laminate type that was loaded to 57.1 kN.

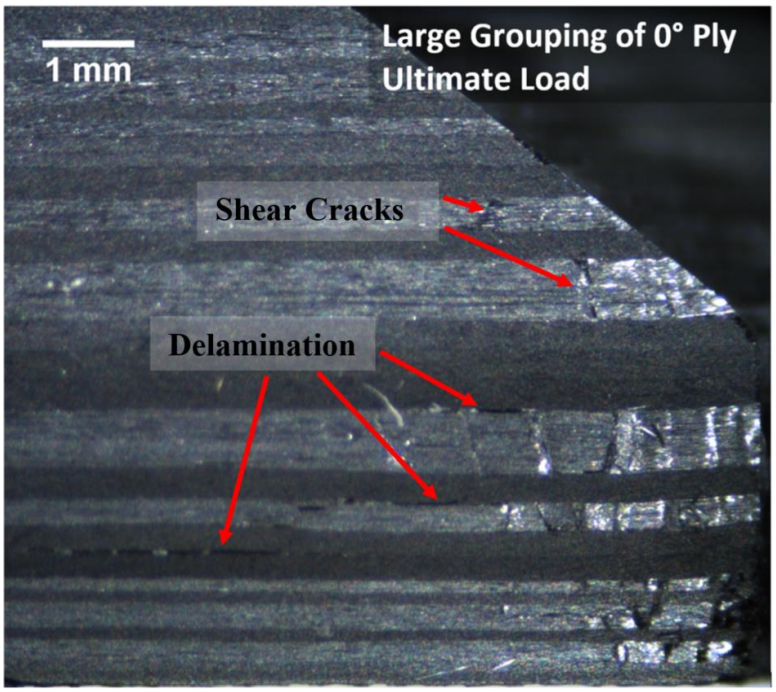

Figure 4.15: Optical mircoscopy of the DLS specimen with large grouping of 0° plies that was loaded to 57.1 kN.

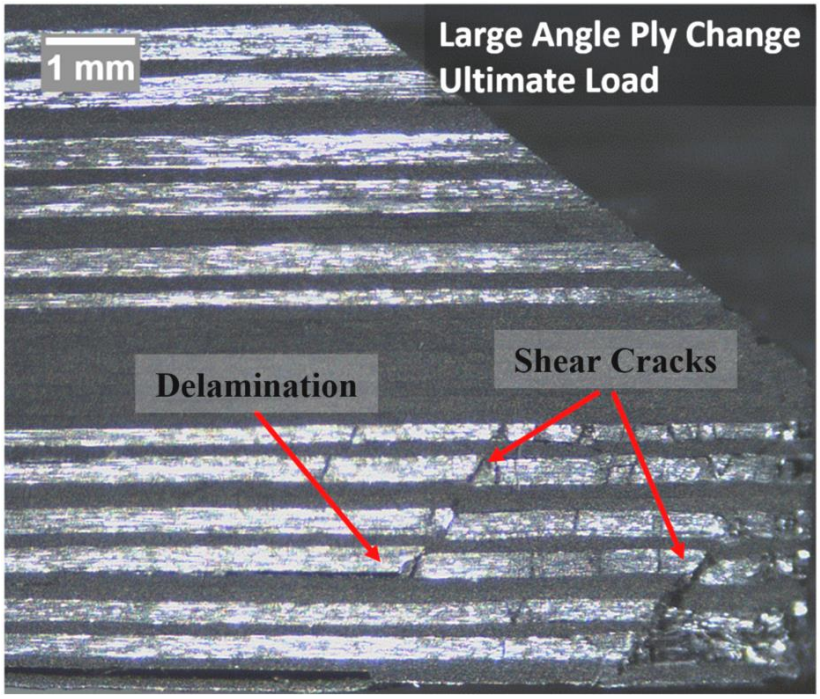

Figure 4.16: Microscopy of the DLS specimen type with large change in angle plies after experiencing 56.9 kN.

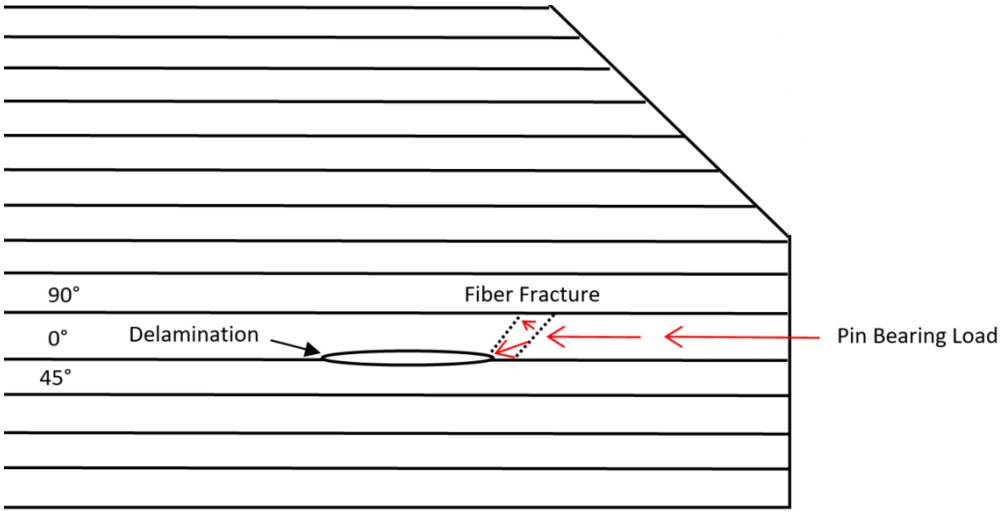

Figure 4.17: Demonstration of delamination initiation after fiber fracture.

4.3 Double and Single Lap Shear Static Test Comparison

Static tests were performed on the single lap shear (SLS) test configuration for all laminate types and results were compared to the DLS specimens. DLS results show that the initial damage occurs at a lower bearing stress for all specimen types compared to the SLS configuration by about a 5% difference (see Table 4.3). The values presented are averages of all static tests performed. Nine DLS specimens and three SLS specimens were tested to attain the initial bearing stress. Bearing stress data for all specimens tested under static loading can be found in Appendix E. Figure 4.18 through Figure 4.20 show the typical bearing stress versus crosshead displacement of each laminate types. Since the SLS test configuration used Hi-Lok fasteners with a pre-load of 45 N-m, SLS joint clamping pressure was higher than the DLS tests. Clamping pressure is likely responsible for the joint stiffening in the early stage of loading for all the SLS specimens plotted. From these plots, it was observed that SLS specimens had a larger final failure displacement and lower bearing stress than the DLS specimen for all specimen types. The lateral constraint also allowed the SLS specimens to more gradually accumulate damage until reaching ultimate failure, thus displacement is greater compared to DLS specimens. In addition, the SLS joint configuration induces both shear and bending loads on the fastener, whereas the DLS mostly produce shear loads. Thus, the SLS specimens to fail at lower ultimate bearing stress level compared to the DLS specimens (see Table 4.4).

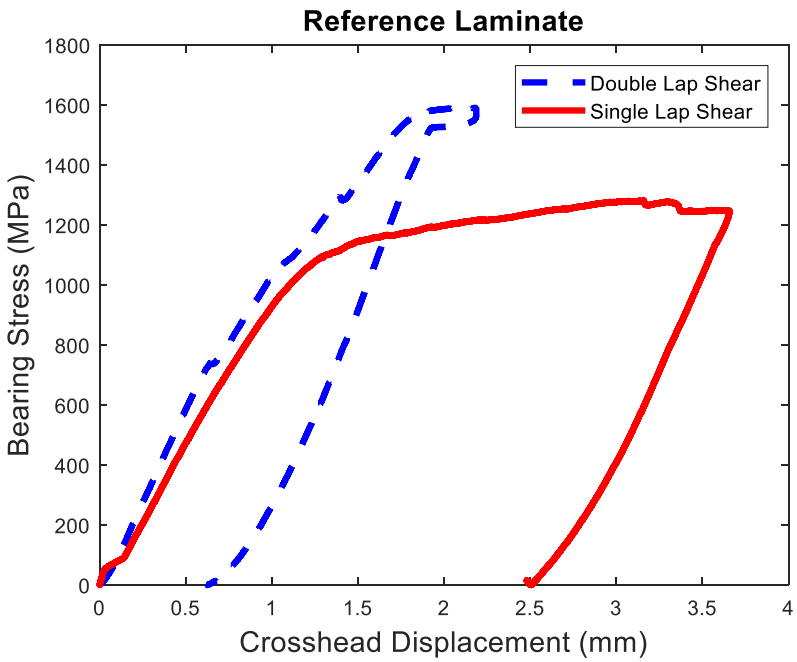

Figure 4.18 DLS versus SLS static test results for the reference type spcimen.

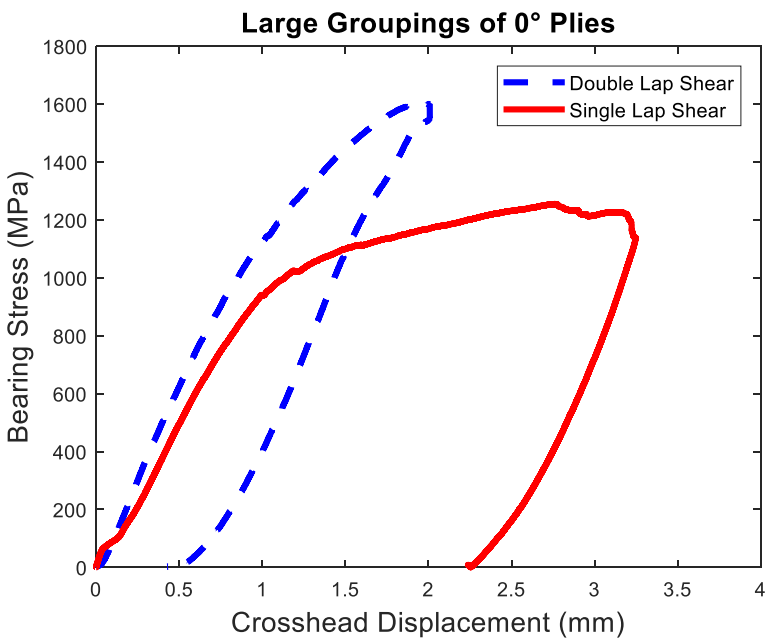

Figure 4.19: Static test results for DLS and SLS specimens with large groupings of 0° plies.

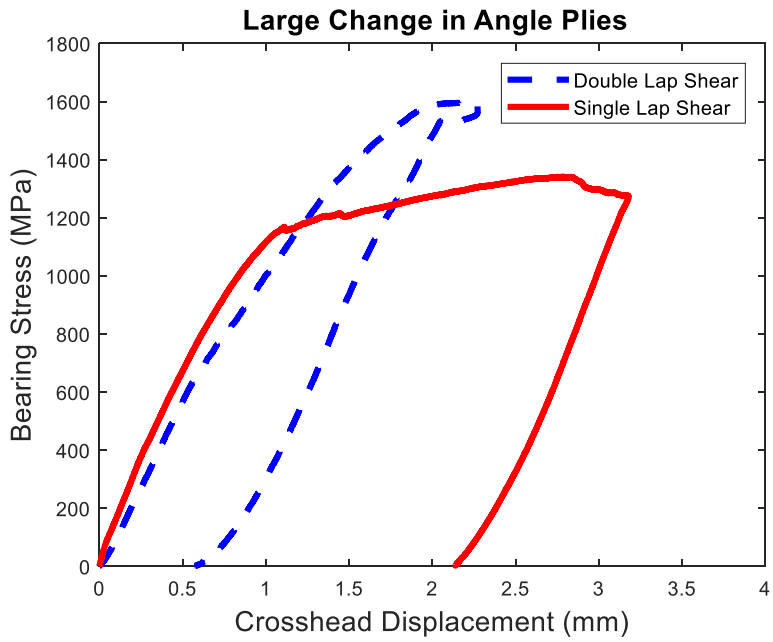

Figure 4.20: DLS and SLS static test results for specimens with large change in angle plies.

Table 4.3: Average initial bearing strength.

Specimen Type	DLS Initial Damage	SLS Initial Damage	% Deviation from DLS
Reference	822 MPa	861 MPa	+4.7 %
Large 0° Groupings	800 MPa	804 MPa	+0.5 %
Large Angle Change	884 MPa	922 MPa	+4.3 %

Table 4.4 : Average ultimate bearing strength.

Specimen Type	DLS Ultimate Bearing Strengths	SLS Ultimate Bearing Strengths	% Deviation from DLS
Reference	1564 MPa	1307 MPa	-18 %
Large 0° Groupings	1574 MPa	1212 MPa	-26 %
Large Angle Change	1570 MPa	1357 MPa	-15 %

The SLS static test microscopy images Figure 4.21 through Figure 4.23 significantly more damage accumulation compared to the DLS static test specimens even though the DLS specimen failed at greater ultimate bearing load. Shear crack formations from the shank to the conical region that were observed in the DLS specimens were also observed in the SLS reference specimen and the large groupings of 0° degree plies specimen. The root cause for greater damage may be due to the initial clamping pressure of 45 N-m from the Hi-lock pin, which suppresses bearing damage from growing in the early stage of loading. As load increases, cracks propagate toward the edge of the bolt head, and then fail in a brooming behavior. This failure type is similar to one that was observed by Wang et al., in a pin bearing failure experiment, where there were no lateral constraints [16]. Since bearing loads were mainly carried by the shank region, cracks propagate from the bolt-hole surface and travel towards the outer surface of the laminate. The conical section provides lateral support and local stiffness on the top half of the laminate thickness, thus preventing cracks from growing towards that direction, until greater load is applied. This corroborates the hypothesis that damage will nucleate at the

boundary of the shank region first (i.e., at transition between straight shank and conical countersunk region), and then with additional applied stress the matrix cracks, delamination, and fiber fracture will propagate to the conical section.

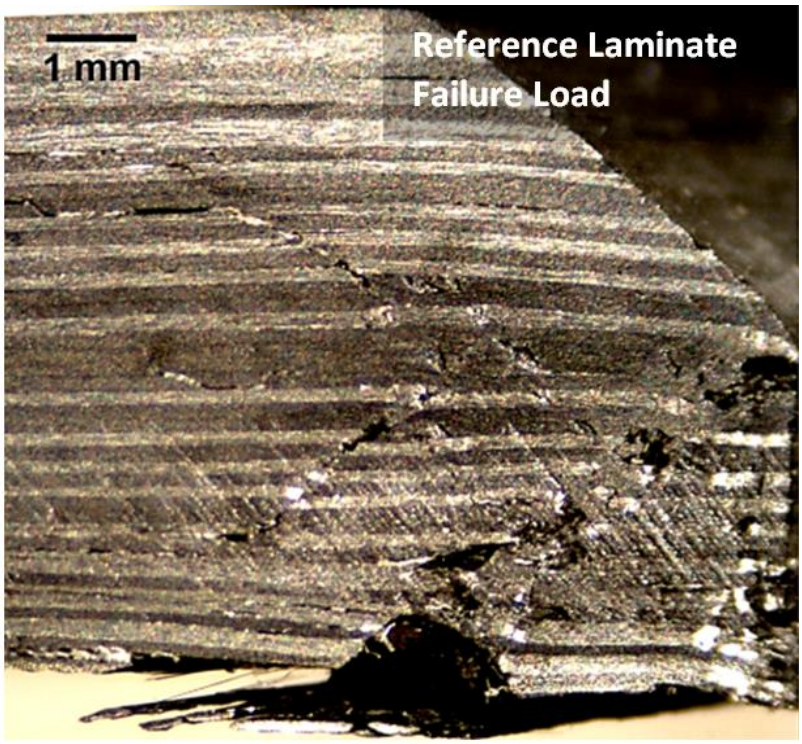

Figure 4.21: Microscopy of the SLS reference laminate that experienced 45.9 kN.

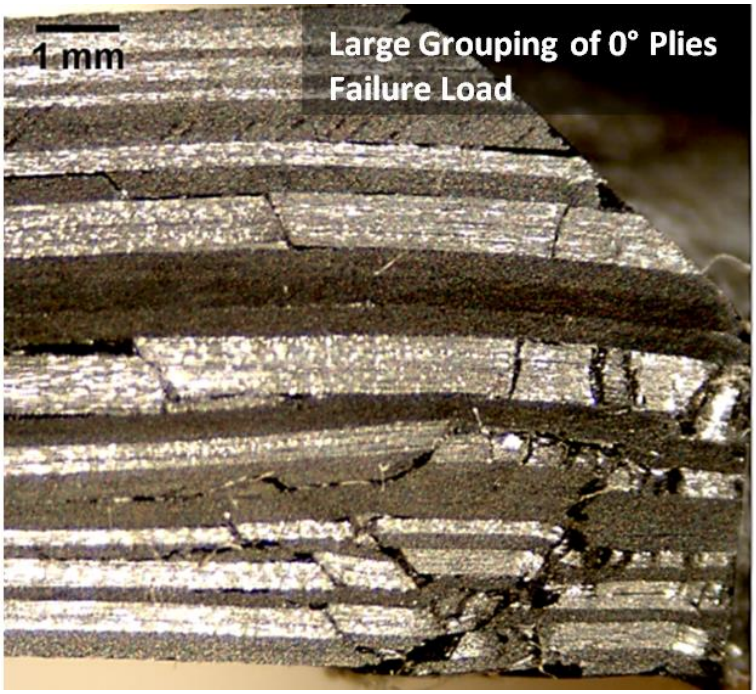

Figure 4.22: Microscopy of the SLS laminate with large groupings of 0° plies after experiencing 44.8 kN.

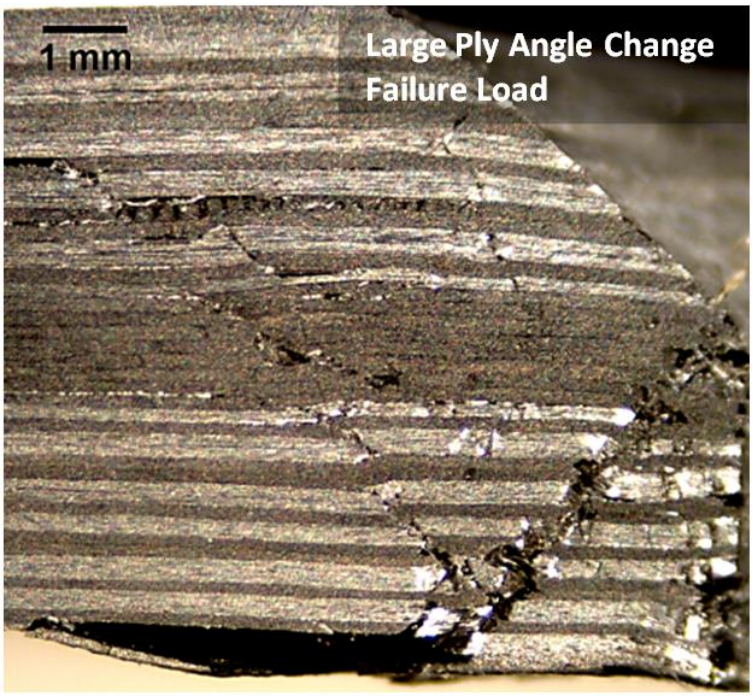

Figure 4.23: Microscopy of image from the SLS specimen with large change in angle plies that was loaded to 47.4 kN.

4.4 Double Lap and Single Lap Shear Fatigue Test

Fatigue bearing tests were completed for both double lap and single lap shear specimens. Delamination initiation and propagation, bolted joint stiffness and hole elongation were investigated through performing three different study cases. In all of these studies, delamination growth was monitored through ultrasonic (UT) C-scans after completing a desired number of cycles. Figure 4.24 shows an example of a C-scan of a countersunk specimen after completing a full fatigue test. Each color corresponds to a thickness value of the specimen. Yellow is about 0.30 inches (7.62 mm), which is the total thickness of the laminate. The various shades of blue represents the different depths of damage from the scanned surface (shank side facing transducer). The outer red circle represents the countersunk largest diameter, whereas the inner red circle is the straight-shank diameter. It should be noted that these holes were filled with putty material to prevent water from entering during the submerged C-scan process. Thus, there are missing data (white color) towards the center of the red circle because of the mismatch in material acoustic impedence causing high attenuation in the signal. Since using the pulse-echo UT technique to produce the C-scan images, the angle of the concial region reflects the return signal in different directions away from the transducer. Therefore, bearing damage within the countersunk diameter was not reliably measured with this method.

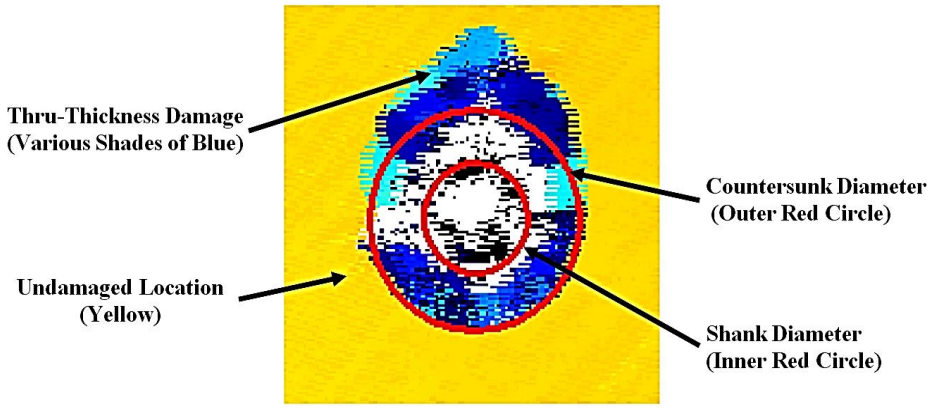

Figure 4.24: Example of a countersunk specimen C-scan image.

In the first fatigue test study, a double lap shear specimen was subjected to cyclic loading at 38% of the ultimate bearing stress and then perform cyclic test again at 50% of the ultimate bearing stress. This investigates the relationship between delamination propagation at increasing load levels and hole elongation. The specimen that has large groupings of 0° plies was subjected to 18 kN at 4 Hz for the first 78,000 cycles and then 24 kN at 2 Hz until a total of 178,000 cycles. This particular fatigue test was chosen to exceed the preset test condition of 4 times an aircraft life cycle to better understand damage propagation. Static tests were performed after completing a set number of cycles and the slope of the plots during up-loading was defined as the current stiffness state of the joint (see Figure 4.25). Joint stiffness versus number of cycles plotted in Figure 4.26 shows a sharp increase in stiffness at the very beginning, from 0 to 8,000 cycles, and then a slight decrease before being stable at 20,000 cycles. This corresponds to about 1% hole elongation. Joint stiffness remained roughly constant until 78,000 cycles during the 18 kN loading. Upon increasing the peak load to 24 kN, the hole elongation rate increased again with additional damage growth from 1.3% to about 9%. Delamination propagation

caused by the increased load can be observed as the difference between the UT C-scan images at 78,000 cycles and 98,000 cycles (see Figure 4.27). Then, the joint stiffness began to fluctuate as the specimen continued to be cyclically loaded, but the stiffness never reduced to the initial level. The stiffness increase during the initial loading cycles is thought to be due to the fact that some debris created during the test is compacted on the bolt-hole surface and therefore creating a tight bolt to hole clearance. McCartney et al. [29] experimentally tested clearance hole and found that increasing clearance between the bolt and hole can reduce the joint stiffness by 30%. Thus, explaining how stiffness can increase when debris from the fatigue test creates a more tight fit contact between the bolt and hole. Without increasing the fatigue load, the hole does not elongate and there is no significant growth in delamination. This type of joint behavior indicates the delamination may arrest if load does not increase beyond the initial loading in fatigue test. Additionally, measuring hole elongation may possibly reveal if there is delamination propagation within the composite without performing ultrasonic C-scan.

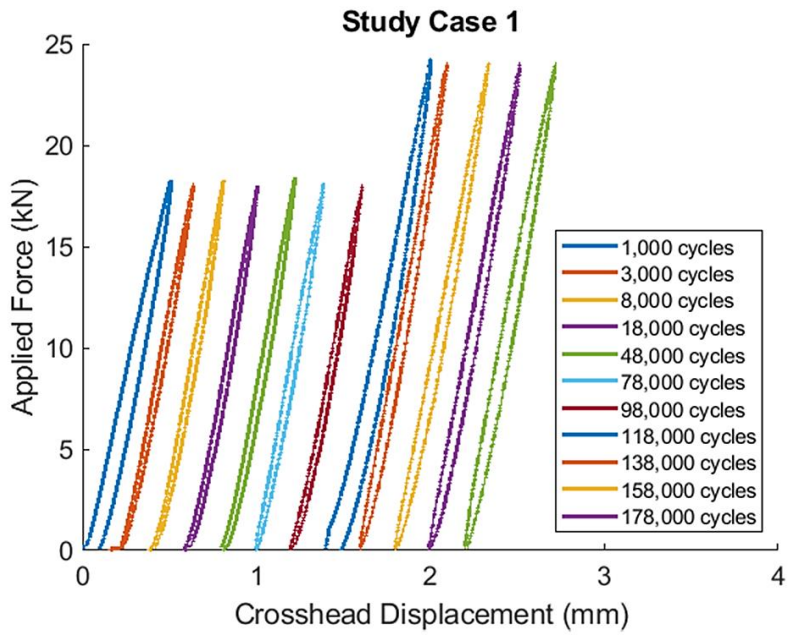

Figure 4.25: Static test plots performed after completing a set number of cyclic loading for a single specimen.

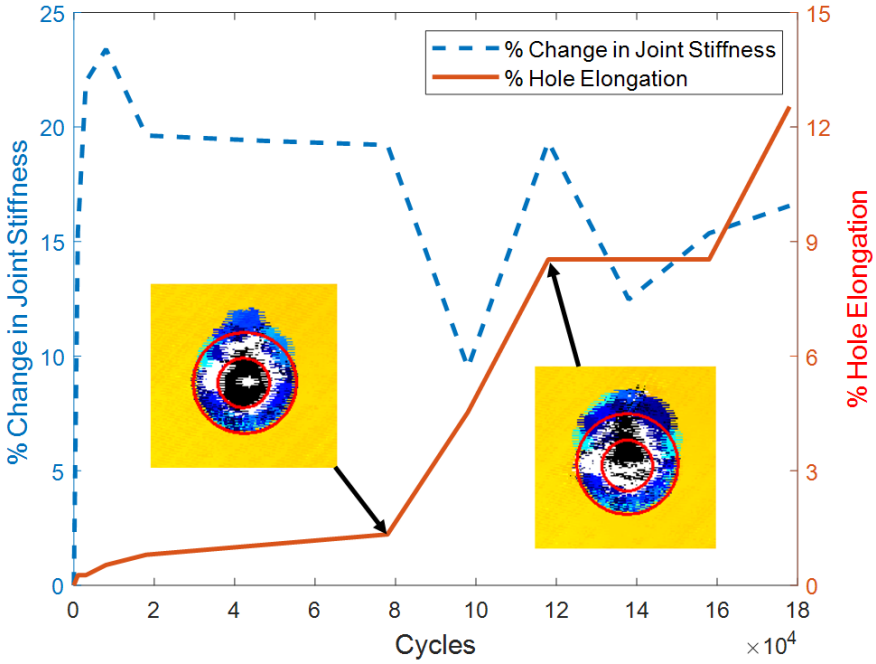

Figure 4.26: DLS fatigue test results illustrating percent change in joint stiffness and hole elongation verus number of cycles.

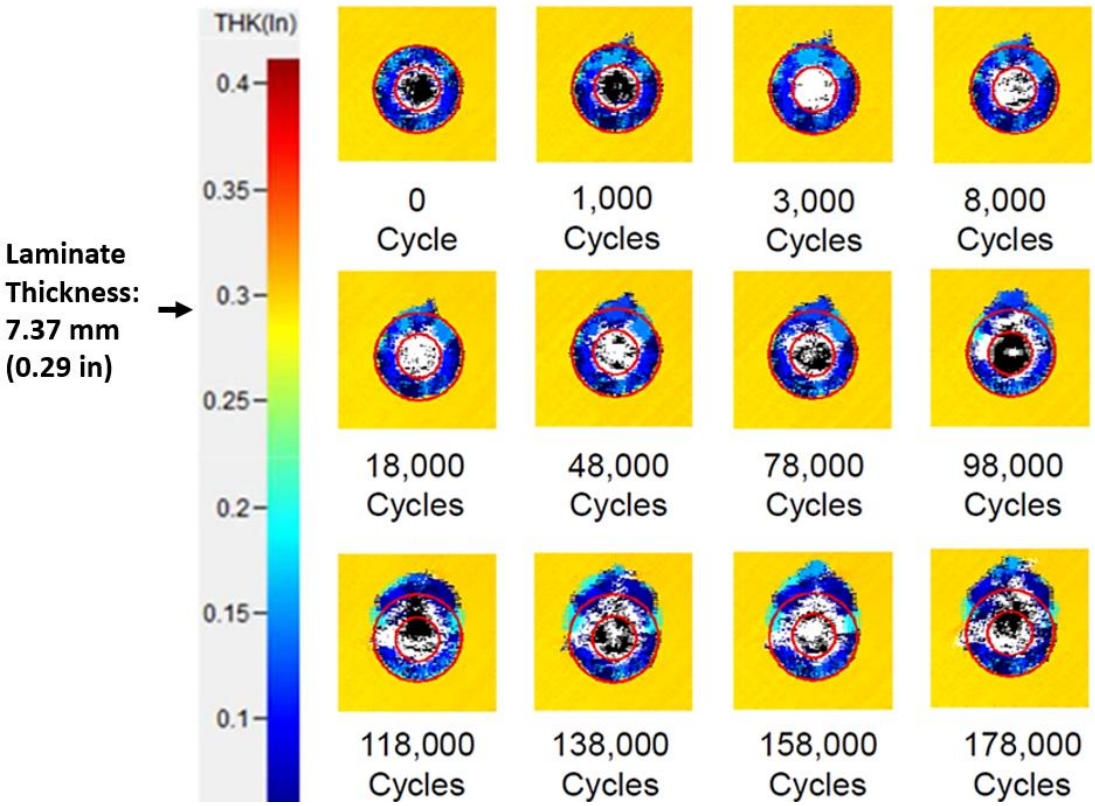

Figure 4.27: Ultrasonic C-scan images for a single DLS fatigue specimen used to monitor delamination propagation. There are no significant delamination growth until increasing load, which can be observed at 78,000 cycles and 98,000 cycles.

Optical microscopy was performed on the specimen after 178,000 cycles. Severe damage accumulated in the shank region and bottom half of the conical section where it intersects with the shank (see Figure 4.28). Failure mechanisms include fiber kinking due to compression-induced load from the pin bearing, delamination, and matrix cracking. Also, this image shows that when fibers undergo compressive fracture in the 0° plies, it is associated with shear cracking in the neighboring 90° and 45° plies. When opposite shear cracks join together, it forms wedge-shape features that promote delamination propagation during cyclic loading.

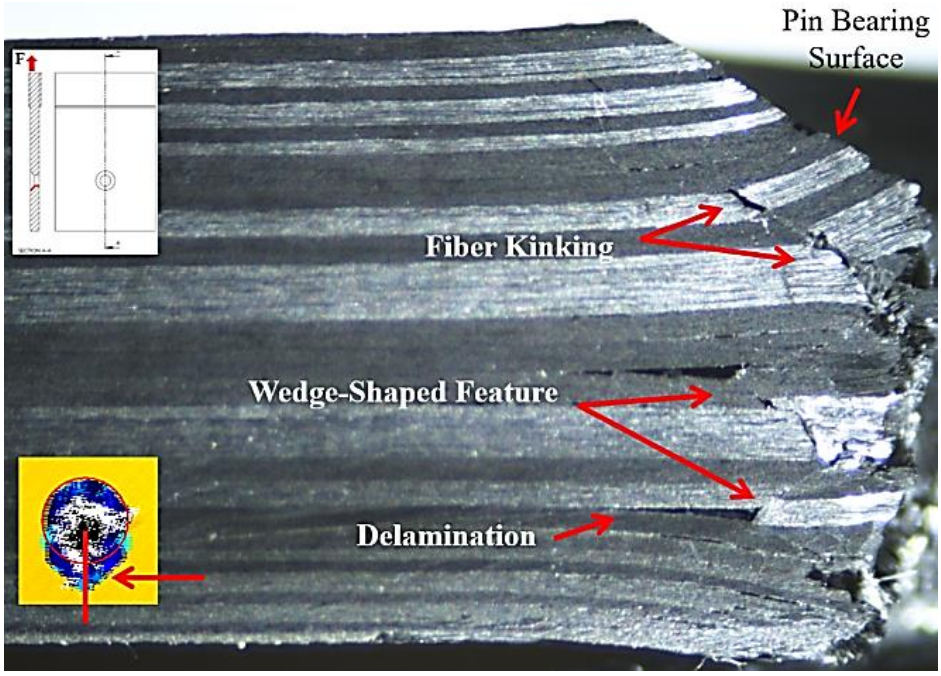

Figure 4.28: Optical microscopy of a DLS specimen after performing 178,000 cycles. Significant damage occurred in the straight shank region of the bolted hole.

The second fatigue study was performed on the DLS joint configuration to investigate the damage growth behavior when applying 66% and 50% of the ultimate load for all specimen types. Selecting 66% ultimate load to perform the fatigue test stems from using a 1.5 factor of safety, which is commonly used in the aerospace industry. The 66% of ultimate load is equivalent to the limit load, when using 1.5 factor of safety. However, fatigue test results from the high loading condition caused the hole to elongate and damage to propagate very early on (about 4,000 cycles) in the experiment (see Figure 4.29), thus making it challenging to investigate bearing damage behavior during the fatigue test. This outcome motivated the reduction of the load to 50% of the ultimate load in subsequent cyclic load tests to allow for a more gradual damage propagation. This behavior was observed for all the laminate types.

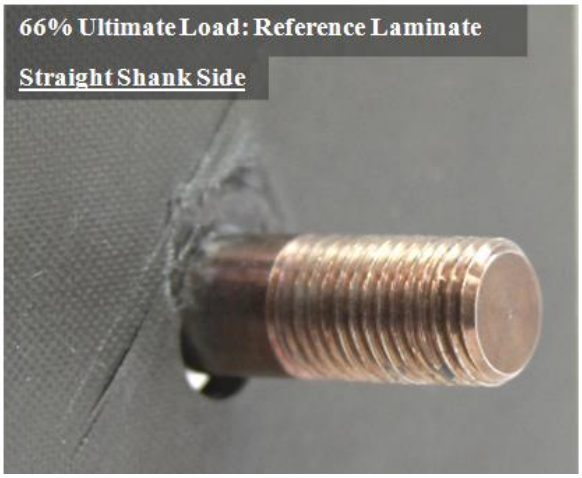

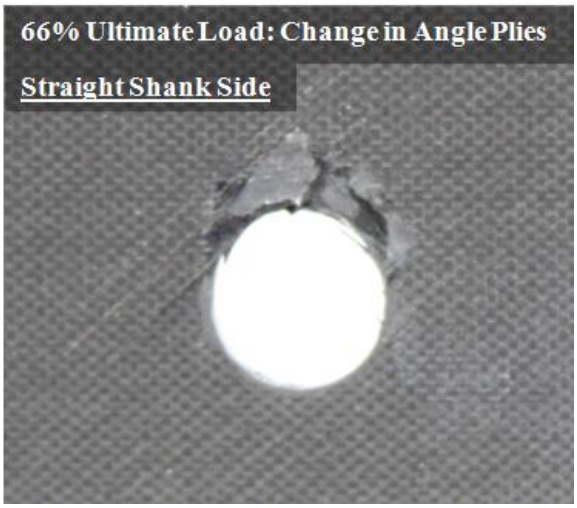

Figure 4.29: Bolted joint after 4,000 loading cycles at 66% of the ultimate bearing load.

Hole elongation was monitored after completing each set of cyclic loading using a small hole gage and a micrometer. Table 4.5 shows a summary of hole elongation measured from one specimen of each laminate type that were tested at 66% ultimate load. In total, there were two specimens tested per laminate types (see Appendix F). Comparing the three different laminates, it can be seen that the specimen type with large change in angle plies have much less hole elongation compared to the other two types. One possible reason for this large difference in hole elongation between the laminate types may be due to damage induced during the drilling process. As explained in the literature review section, drilling induced damages, such as delamination and matrix burn-out was found to reduce strength of the material [16], [10]. In comparsion to the specimens tested at 66%, the specimens tested at 50% ultimate bearing stress had much smaller hole elongation (see Table 4.6). At 2,000 cycles, the Reference laminate hole elongates to 1.32 mm at the high bearing stress compared to 0.051 mm from the low bearing stress, which is approximately 26 times larger. A comparison of all DLS fatigue tests are shown in the Figure 4.30 where these measured values are plotted for comparison.

Table 4.5: Hole elongation measured after completing a set number of cycles for a DLS specimen loaded at 66% of ultimate bearing stress from each laminate type.

Number of Cycles	Reference Laminate	Large Groupings of 0° Plies	Large Change in Angle Plies
1,000	1.32 mm	1.19 mm	0.27 mm
2,000	1.32 mm	1.30 mm	0.27 mm
3,000	1.32 mm	1.37 mm	0.30 mm
4,000	1.60 mm	1.50 mm	0.30 mm

Table 4.6: Hole elongation measured after completing a set number of cycles for a DLS specimen loaded at 50% of ultimate bearing stress from each laminate type.

Number of Cycles	Reference Laminate	Large Groupings of 0° Plies	Large Change in Angle Plies
2,000	0.051 mm	0.076 mm	0.051 mm
4,000	0.102 mm	0.152 mm	0.127 mm
6,000	0.127 mm	0.178 mm	0.152 mm
10,000	0.178 mm	0.254 mm	0.203 mm
26,000	0.178 mm	0.0279 mm	0.203 mm
41,000	0.203 mm	0.0279 mm	0.203 mm
61,000	0.229 mm	0.305 mm	0.203 mm
101,000	0.229 mm	0.330 mm	0.229 mm
120,000	0.254 mm	0.330 mm	0.254 mm

Figure 4.30 shows the hole elongation versus number of cycles for each of the laminate types. Specimen types from the large groupings of 0° plies and large change in angle plies have hole elongattion beyond 4%, which is typically considered bearing failure (or maximum permissible elongation) in the aerospace industry. Those particular specimens may have had drilling-induced damage that was not detected through ultrasonic C-scanning because it was within the conical diameter (see Figure 4.31). As discussed in the background chapter, having high feed rates, inadequate backing support or dull tools from the drilling process can all introduce flaws within the laminate.Although most holes were fabricated at UC San Diego lab facility, some specimens were sent to an external machine shop. Therefore, not all specimens that were tested under fatigue had this type of damage because of how the holes were fabricated. Half of the holes were meticuously machined in a machining lab at UC San Diego, which resulted in having a hole elongation below 4 percent, even after 80,000 cycles of loading. Some specimens were sent to a machine shop and their hole elongation measured were greater than 4 percent. Despite the larger change in percent hole elongation, the trend found in all laminate types are the same. By applying a fatigue load at constant amplitude, the hole would elongate in the early cycles and become steady. Hole elongation stops increasing after 50,000 cycles and continue to not grow until the test was stopped at 120,000 cycles, which is equivalent to four times the life cycle of an aircraft.

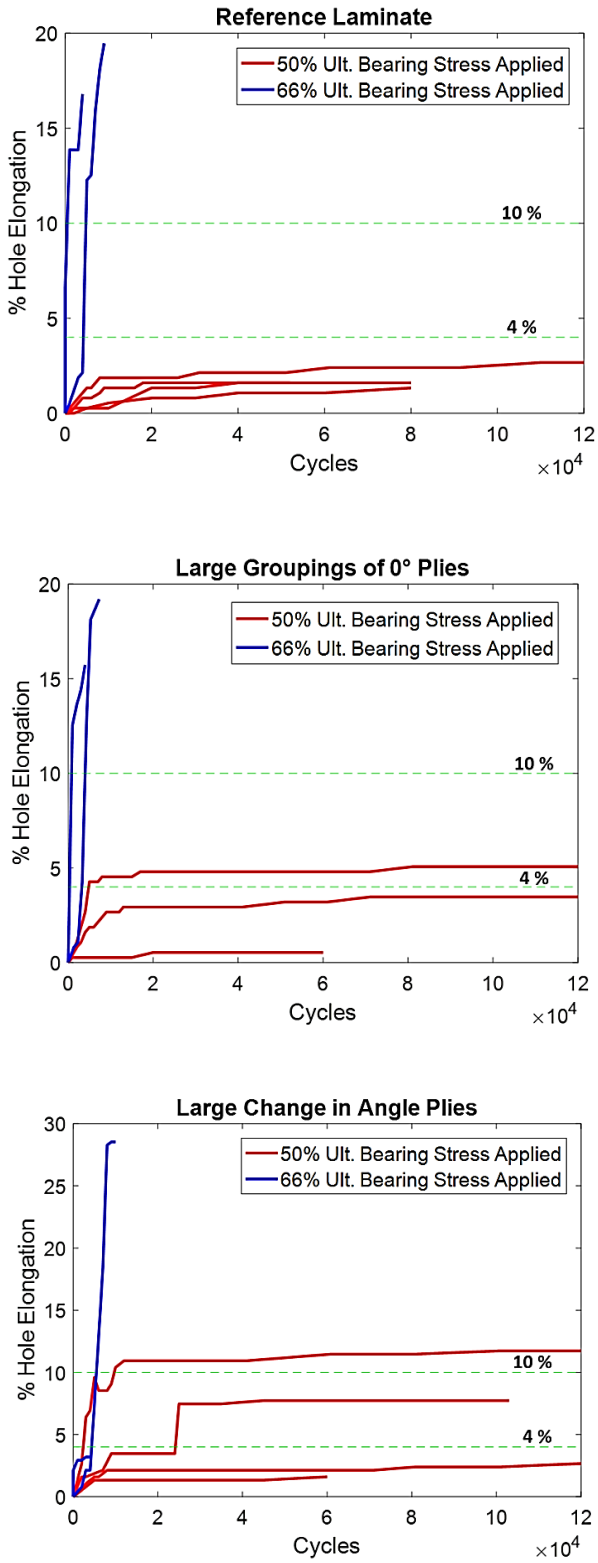

Figure 4.30: DLS fatigue test results for each laminate type comparing specimens loaded at 66% versus 50% ultimate bearing stress.

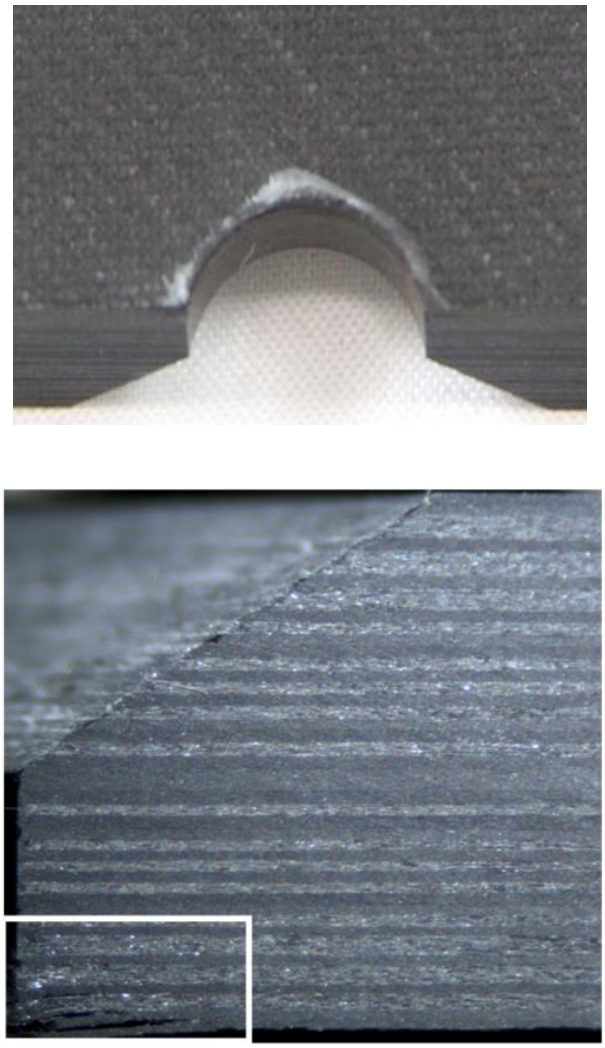

Figure 4.31: An example of a pristine specimen with delamination induced by drilling.

In total 17 specimens were tested for DLS fatigue test and their joint stiffness, hole elongation and delamination were monitored through performing static tests, hole gauge measurement, and UT C-scans. Figure 4.32 show all of the plots from a series of static test performed after completing a desired set of cycles. Each figure represent a laminate type that were loaded at 50% ultimate bearing load and completed 120,000

cycles. All bearing fatigue tests were stopped after reaching 120,000 cycles (4 times an aircraft lifetime) or when the pin fractures. The stiffness was calculated from the slope of the loading plot for each laminate types comparing joint stiffness versus the number of cycles are shown in Figure 4.33 through Figure 4.35. Those plots show that when hole elongates and the joint stiffens in the early cycles, up to 10,000-20,000. After the initial increase in joint stiffness, it fluctuates throughout the fatigue test. One key finding is that the joint does not return back to its original joint stiffness, which may be caused by debris accumulating on the bolt hole surface. Each time the pin was unloaded and then loaded again, the debris from the damage surface may be compacted on the hole surface. This creates a new and tighter clearance between the bolt and hole surface. Thus, when static test is performed immediately after a set number of cycles, the pin is bearing against a locally stiffened surface until damage significantly propagates. This phenomenon is similar to the conclusions made on bolt-hole clearance influence on bearing strengths. Researchers found that bolt-hole clearance affects load distribution when the joint is initially loaded, but not the ultimate bearing strength of the joint [29]. After each fatigue test, the debris changes the bolt-hole clearance and as a result changes the initial contact stress. Since the fatigue tests were performed under constant load, there were no significant damage observed beyond the initial growth. This indicates that delamination will eventually arrest under cyclic loading, until the applied load is increased. Additionally, Figure 4.33 through Figure 4.35 plots show that there is a relationship between the percent change of hole elongation and joint stiffness. When the hole elongation stops growing, then the joint stiffness change levels out. C-scan images on those plots show that delamination extends beyond the conical diameter, at the inflection

point where the hole elongation stops propagating and with increasing cycles, there was no significant change in the damage growth. Ultrasonic C-scans images in Figure 4.36 supports this conclusion. Each image is from the same tested specimen after completing a set number of cycles. This allows for delamination propgation to be monitored in one completed fatigue test. The greatest damage produced in the C-scan image shows dark blue color in the first 4,000 cycles before seeing light blue color. Colors shown on the C-scan images were produced based on the time it takes the ultrasonic wave to reflect back to the transducer after transmitting through the composite. This time is converted into measurement of depth through the thickness of the laminate. Based on the color scale in Figure 4.36, darker blue means it is closer to the outer surface of the laminate on the shank region. This shows that delamination may occur towards the bottom straight shank region, before propagating through the thickness of the laminate, towards the conical region. Shear cracks propagating through the thickness may indicate that there are more intra-laminar shear stress bridging cracks compared to the inter-laminar shear stress that initiates delamination. After 10,000 cycles, there is no significant delamination growth observed in the C-scan images. All specimen types show the same behavior. Although, the reference laminate in Figure 4.36 show dark blue lines around the laminate, indicating delamination, it is located on the outer surface. Thus, conclusions made about the bearing damage behavior under cyclic loading is still valid because it did not affect where the pin is bearing against the specimen.

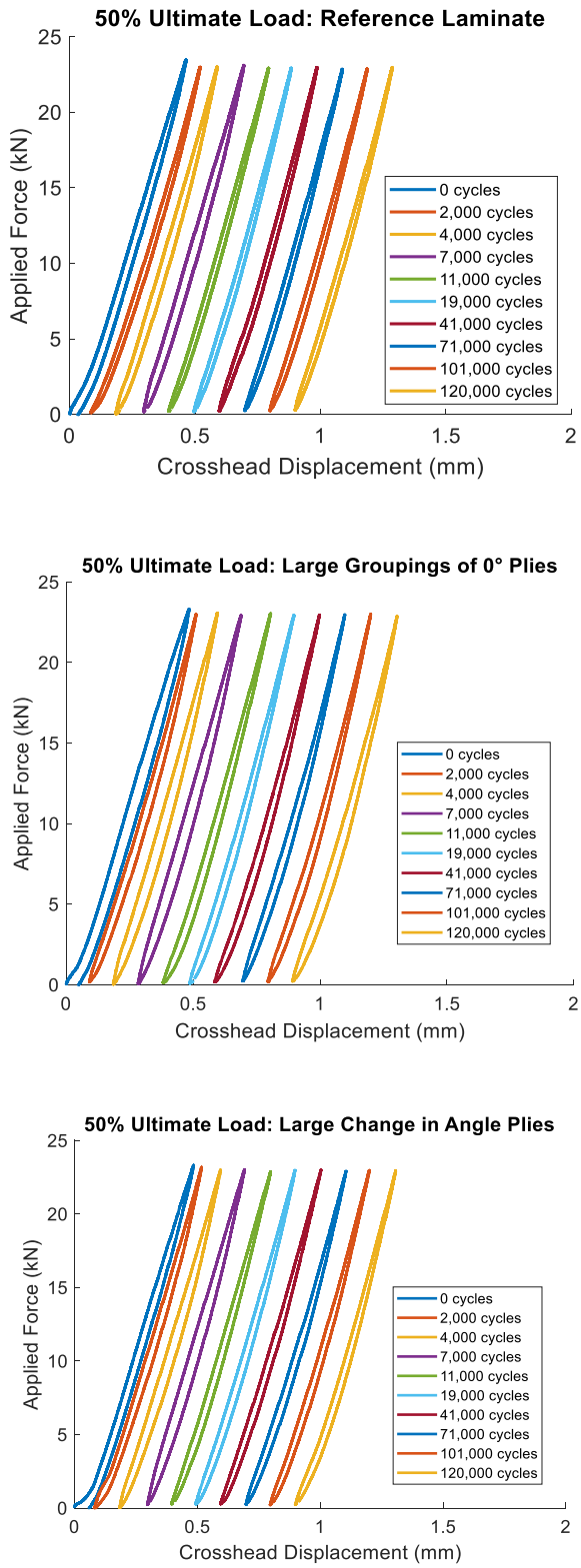

Figure 4.32: Static tests performed after completing a set of cyclic loading to monitor bolted joint stiffness for all lamiante types.

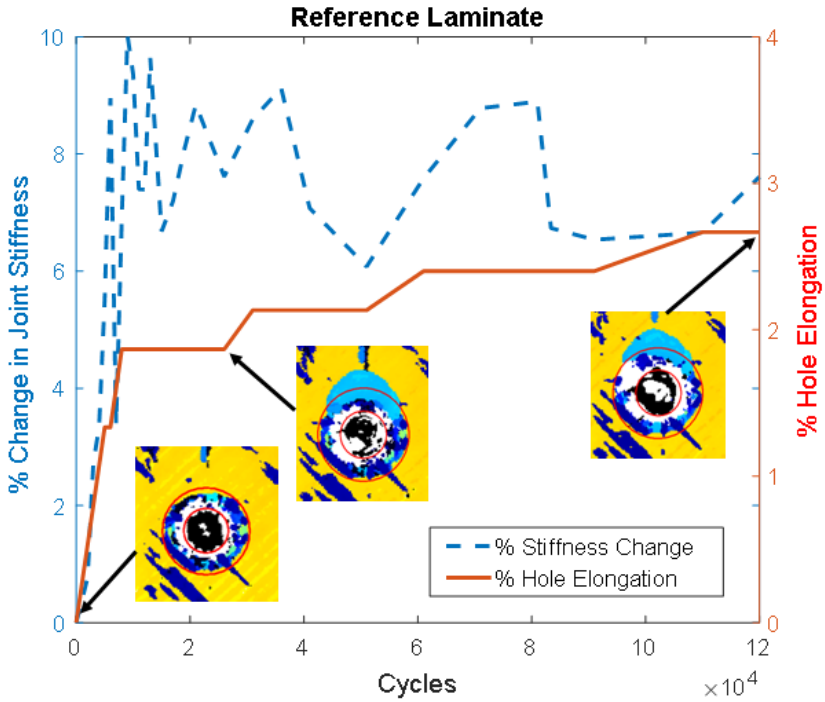

Figure 4.33: Change in joint stiffness and hole elongation for the reference laminate that was cyclic loaded at 50% ultimate bearing stress.

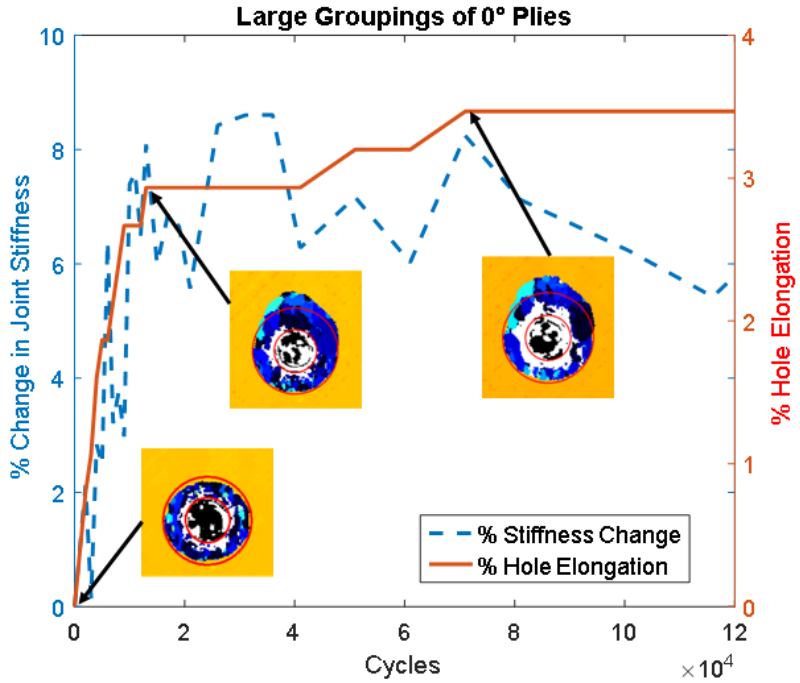

Figure 4.34: Change in joint stiffness and hole elongation for the laminate with large groupings of 0° plies that was loaded at 50% ultimate bearing stress.

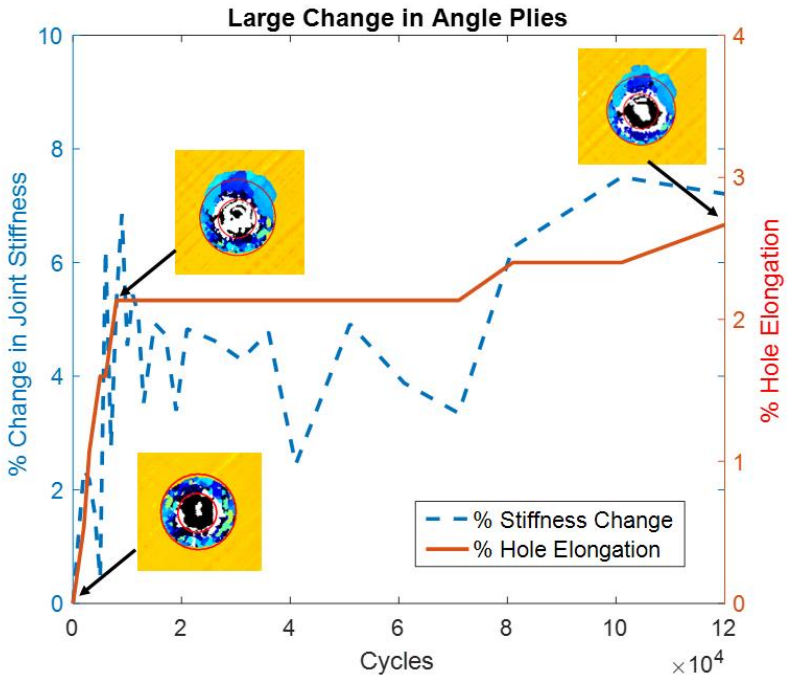

Figure 4.35: Percent change in hole elongation and joint stiffness versus cycles for for the specimen with large change in angle plies that was loaded at 50% ultiamte bearing stress.

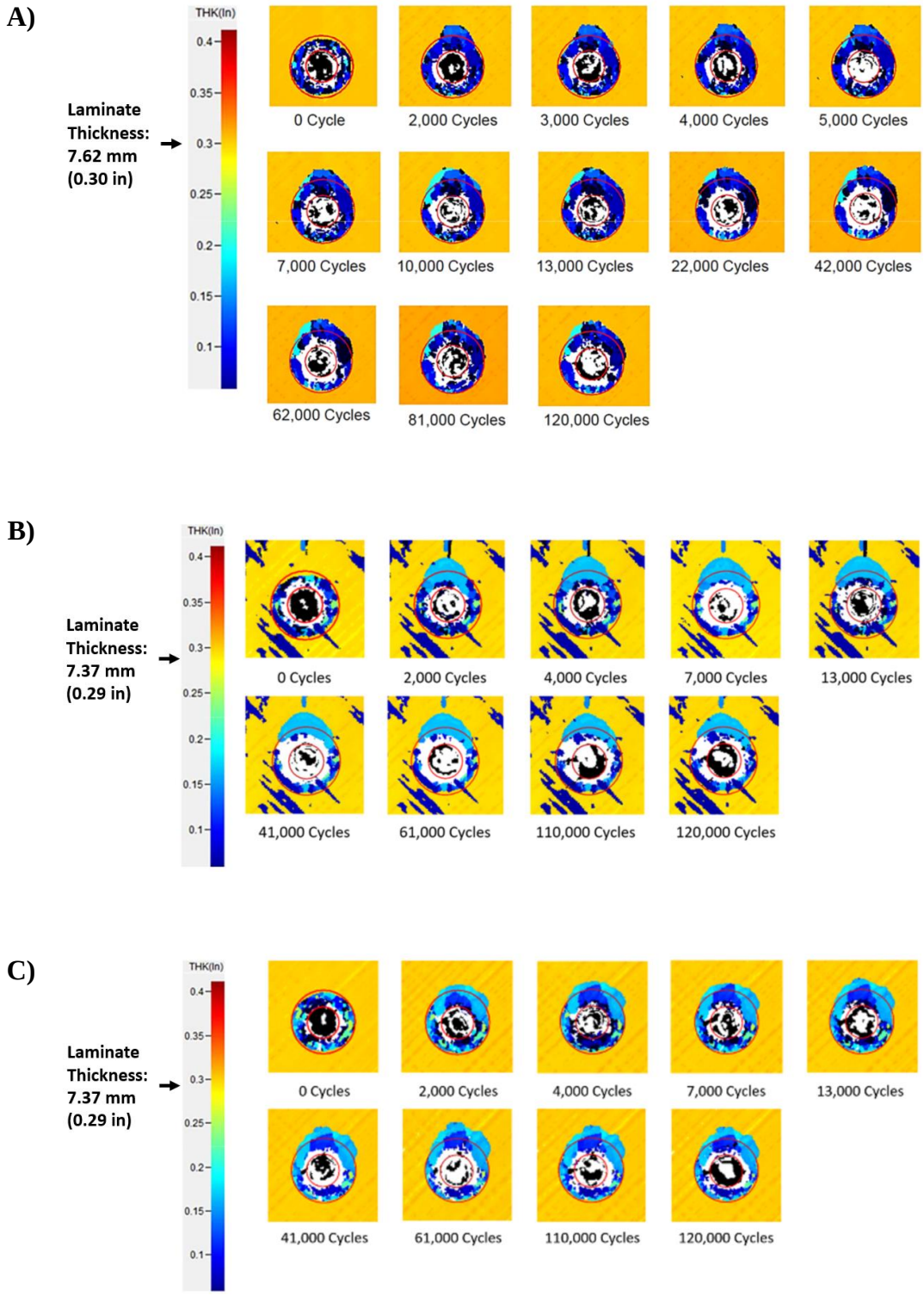

Figure 4.36: C-scan images used to monitor delamination growth in fatigue test for A) large groupings of 0° plies, B) reference lamiante and C) large change in angle plies.

Ultrasonic C-scan images comparing the 66% versus 50% of the ultimate bearing stress support the hole elongation versus number of cycles conclusion. Two specimens that have large groupings 0° degree plies in Figure 4.37 were either loaded at 66% or 50% ultimate bearing stress. The top row images represent a specimen that has been loaded to 66% ultimate bearing load and bottom is 50%. These images show that the rate of hole elongation may indicate the severity of bearing damage, such that measuring hole elongation can be a method of assessing delamination propagation without using costly NDE techniques. In the early stage of the fatigue test, the specimen loaded at 66% ultiamte bearing load shows that the rate of hole elongation is greater and bearing damage is more severe compared to the 50% tested specimens. Furthermore, damage in the 66% specimens keep increasing, as shown in Figure 4.37, corresponding to increasing hole elongation, as shown in Figure 4.30. Meanwhile, the 50% specimens show little damage change after 22,000 cycles in Figure 4.37, corresponding to the relatively little (or no) increase in hole elongation, as plotted in Figure 4.30 for the 50% of ultimate tests.

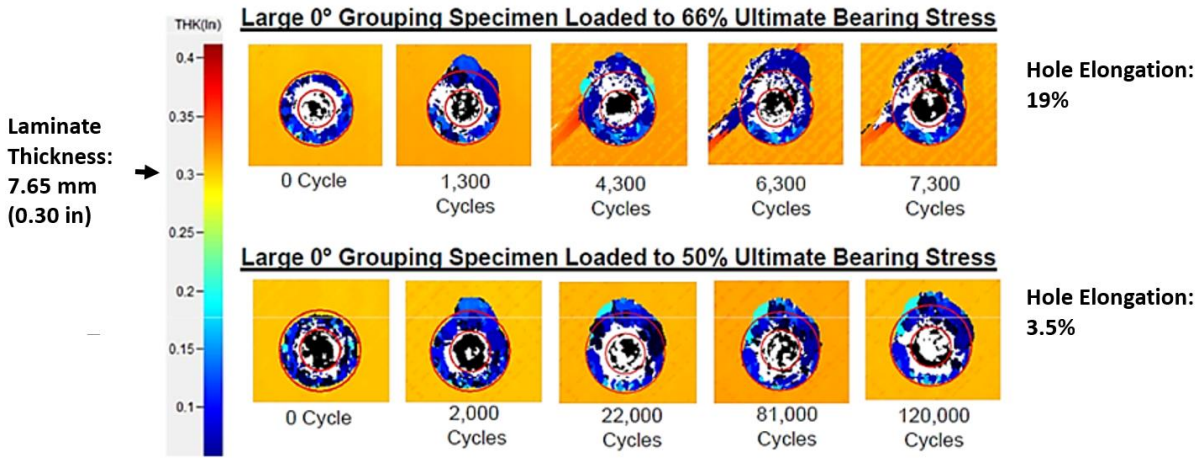

Figure 4.37: Ultrasonic C-scans of specimen cycled at 66% ultimate bearing stress (top) versus 50% ultimate bearing stress (bottom).

Optical microscopies comparing the specimens cycled at 66% ultimate bearing loads are shown in and Figure 4.38 through Figure 4.40. The specimens that experienced 50% ultimate bearing loads are shown in Figure 4.41 through Figure 4.43. Major failure modes include matrix cracks, delamination, shear cracks, and material erosion. The microscopy images also show shear cracks initiating from opposite direction and moving towards the same direction. The joining of these two shear cracks initiates delamination and creates a wedge shape feature, which propagates delamination as loading is applied on the bearing face by the fastener. When shear cracks form, it can either grow towards the outer surface of the laminate, in the shank region, or towards the conical region of the laminate. Shear cracks that move towards the outer surface of the laminate can initiate delamination near the last few plies, instead of arresting when it reaches the last ply. This may be caused by the lateral constraint from the finger-tight washers that were applied prior to performing the fatigue test. As shown in Figure 4.33 through Figure 4.35, joint

stiffness increases in the beginning of the cyclic load and becomes steady. However, it does not decrease below the initial joint stiffness. Shear cracks may have arrested at the very last ply and not initiate delamination, if the shear cracks travel beyond the washer diamater. As described by Wang et al. [5], shear cracks extending beyond the washer will behave similarly to a pin bearing joint and fail catastrophically. When shear cracks move toward the conical region of the laminate, delamination will also be initiated near the conical and straight shank interface. This phenomenon was observed for the specimen loaded at 50% ultimate bearing load and may be caused by local stiffness from the conical section of the laminate and the lateral support of the washer. However, specimens loaded at 66% ultimate bearing load show delamination occuring in both the shank and conical region of the laminate. The high fatigue load caused the pin to impact the bolted hole surface more violently, thus dissipating more strain energy through the laminate thickness. This may lead cracks propagation to extend towards and through the conical region. Additionally, at the 66% ultimate bearing load, specimens show more material erosion occuring on both the interface between the shank and the conical region as well as the bottom edge of the straight shank region. This may be caused by pin repeated impact in the loading direction and bending of the pin. In order to develop a deep-level understanding of whether or not pin bending effects bearing damage, the semi-circular notched (SCN) experiment was created.

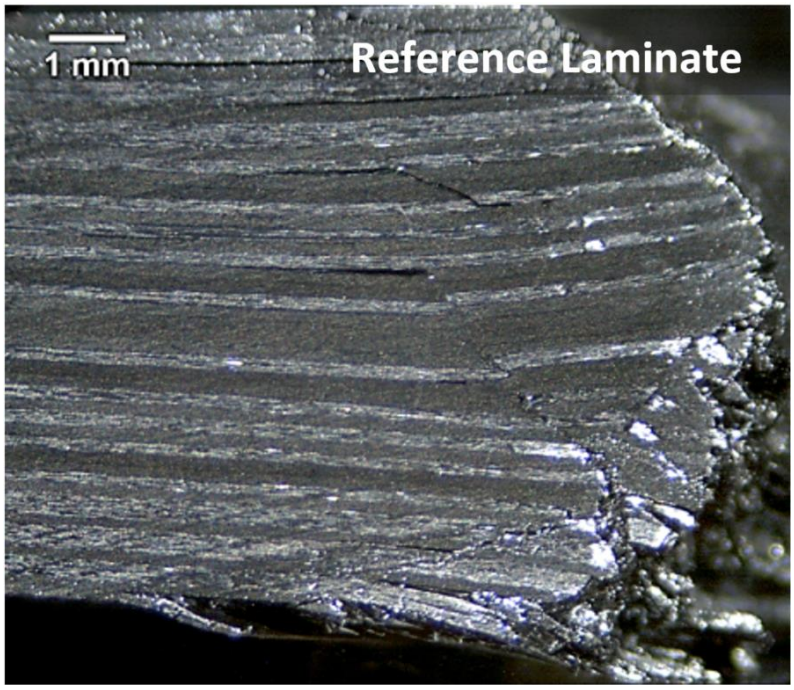

Figure 4.38: Microscopy of the reference laminate after cyclic loading it to 66% ultimate bearing stress.

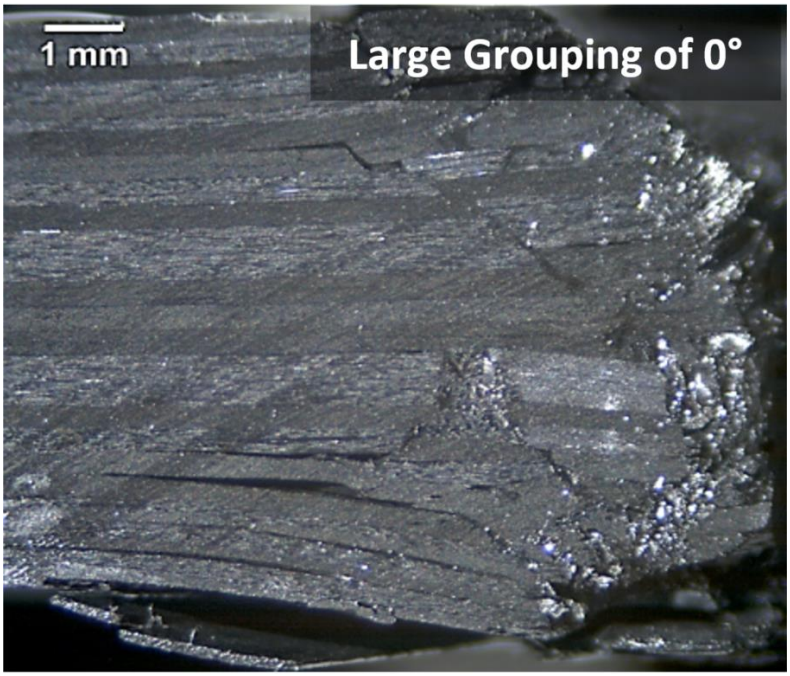

Figure 4.39: Microscopy of the DLS specimen with large grouping of 0° plies after performing cyclic load at 66% ultimate bearing stress.

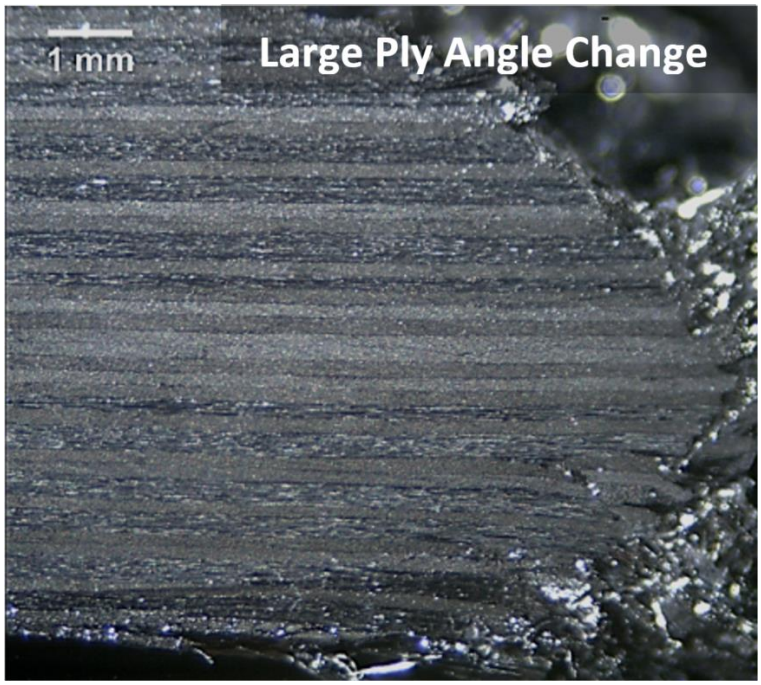

Figure 4.40: Microscopy of the DLS specimen with large chagne in angle plies after performing cyclic load at 66% ultimate bearing stress.

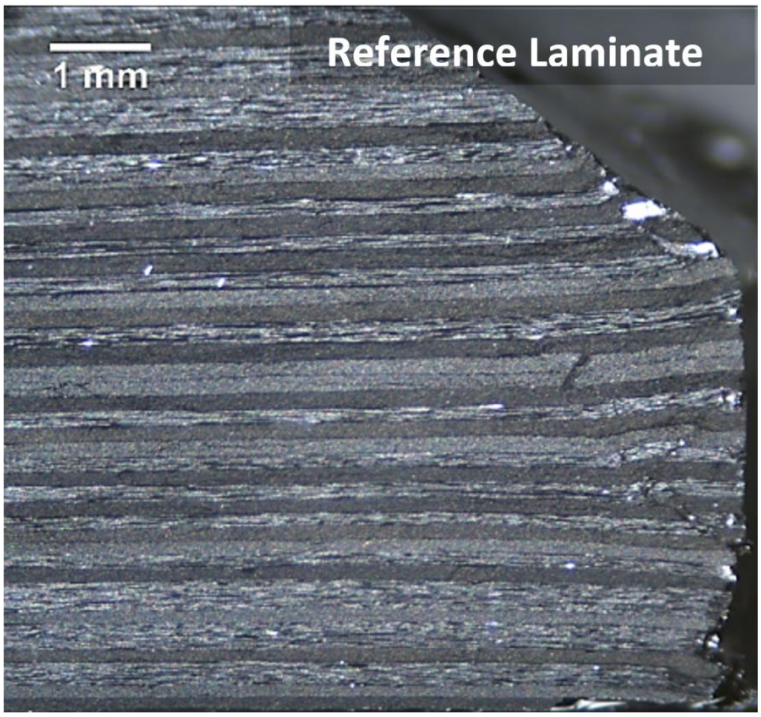

Figure 4.41: Microscopy of DLS reference laminate after experiencing cyclic load at 50% ultimate bearing stress.

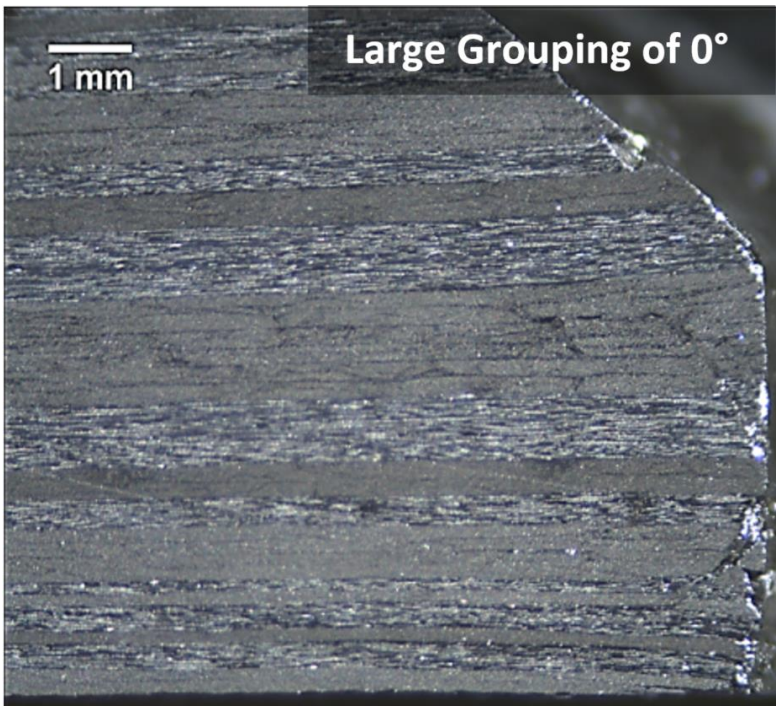

Figure 4.42: Microscopy of DLS specimen with large grouping of 0° plies after experiencing cyclic load at 50% ultimate bearing stress.

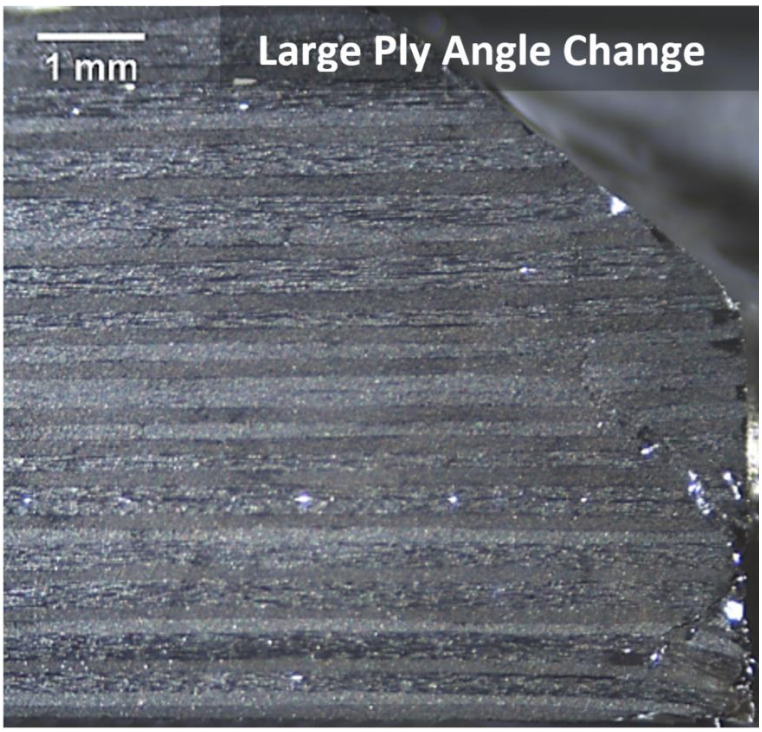

Figure 4.43: Microscopy of DLS specimen with large change in angle plies after cyclic loading it at 50% ultimate bearing stress.

4.5 SEMI-CIRCULAR NOTCH STATIC TEST

The semi-circular notched (SCN) experiment was developed to investigate the effect of pin bending and results from these tests were compared to DLS test results. Both experiments were performed using specimens having the countersunk hole, however the SCN configuration also tested straight through-hole specimens. Static test results for the three types of SCN and DLS specimens are shown in Figure 4.44. These plots show that the DLS joint has a significantly higher bearing strength (about 2X) compared to the SCN countersunk and through-hole specimens. Table 4.7 and Table 4.8 summarizes the average initial failure stress and ultimate bearing strength of the different configurations for all tests. Bearing stress values of the countersunk holes were calculated by considering only half the laminate thickness area, since it was assumed that the shank region carried all of the bearing loads. In the DLS configuration, there was a consistent finger tight torque that was applied directly on the bolt, which provided a lateral pressure closer to the joint than in the SCN experiment. The lateral pressure in the SCN was applied from the vise to the two sliding aluminum plates acting as the lateral constraint to restrict brooming phenomena that was found in pin bearing tests, which has no lateral constraint [16]. However, adding the two plates in the SCN test configuration may have helped with the brooming effect, the applied lateral force is further away from the pin loading location, compared to the DLS test setup. Thus, global stresses in the SCN specimens are not the same, but the local stresses at the pin loading location would theoretically be similar to DLS specimens. Removing the aluminum plates will change the experiment into a pin loading. Therefore, lateral reinforcement is necessary to emulate the DLS joint configuration as close as possible.

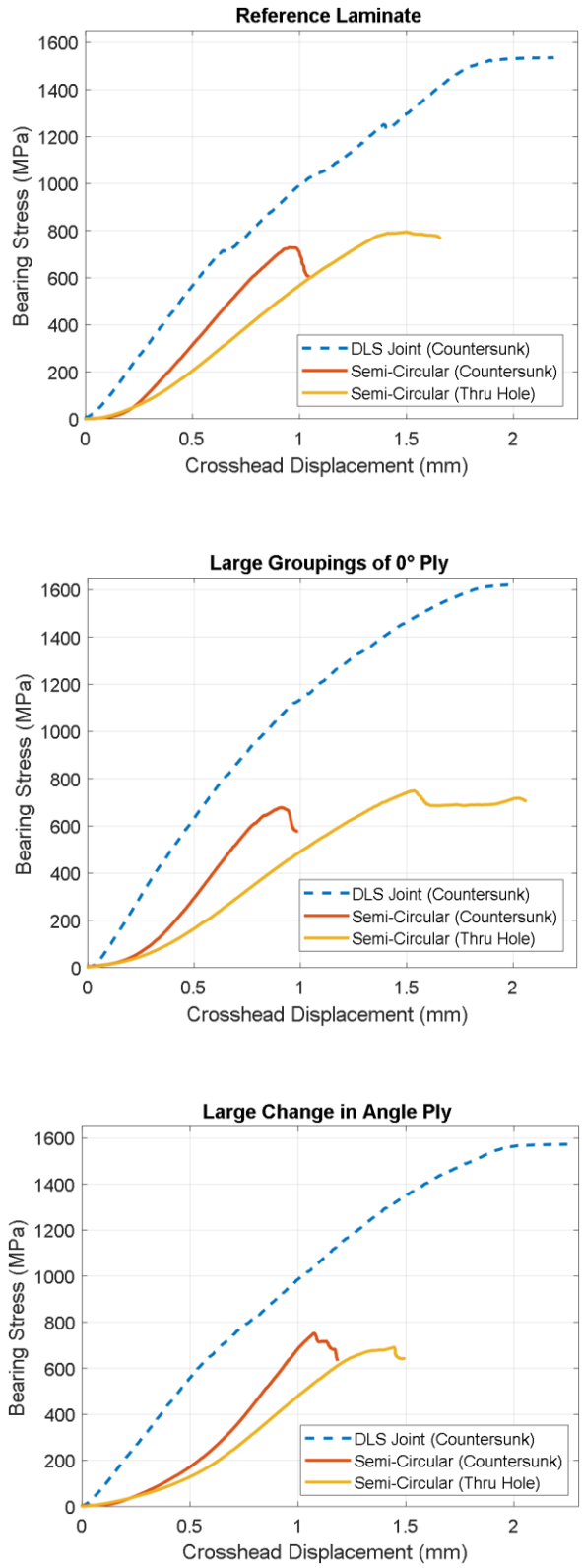

Figure 4.44: DLS and SCN static test results for three laminate types

.

Table 4.7: Average initial failure stress from DLS and SCN static tests showing that regardless of the test type, their initial failure stress is similar.

Average Initial Failure Stress			
Specimen Type	**DLS Countersunk**	**SCN Countersunk**	**SCN Through-Hole**
Reference Laminate	822 ± 54 MPa	768 ± 30 MPa	741 ± 29 MPa
Large 0° Groupings	800 ± 53 MPa	685 ± 19 MPa	740 ± 23 MPa
Large Angle Ply Change	884 ± 156 MPa	761 ± 15 MPa	714 ± 15 MPa

Table 4.8: Bearing strength from DLS and SCN static tests.

Average Bearing Strengths			
Specimen Type	**DLS Countersunk**	**SCN Countersunk**	**SCN Through-Hole**
Reference Laminate	1564 MPa	774 ± 30 MPa	741 ± 82 MPa
Large 0° Groupings	1574 MPa	699 ± 14 MPa	740 ± 6 MPa
Large Angle Ply Change	1570 MPa	761 ± 20 MPa	714 ± 15 MPa

Bearing strengths for the countersunk and through-hole in the SCN experiment showed no significant differences between the laminate types. Since the pin loaded on the countersunk hole was only loaded on the straight shank region its bearing strength is similar to the through-hole. However, microscopy showed different damage morphologies between these two hole types (see Figure 4.45). All of these microscopy images were taken by sectioning the specimens along the loading direction, which is parallel to the 0° plies. The images in the first row are the SCN through-hole specimens for the reference laminate, large groupings of 0° plies and large change in angle plies from left to right, respectively. Bearing damage was found on both the top and bottom edges of the hole, such as matrix cracks, delamination, fiber fractures and shear cracks. Results indicate that matrix cracks near the center of the through-hole specimen, which lead to kink band formation. These kink bands eventually lead to shear cracks traveling through the outer surface of the laminate. Other researchers observed similar results from performing DLS static test on a protruding head fastener [4, 5]. Ultrasonic C-scan images of the through-hole specimens show dark blue color around the hole, indicating that the delamination occurs near the outer surfaces of the specimen (see Figure 4.46). The color scale is dependent on the thickness of the laminate. Thus, darker blue color represents delamination closest to the outer surfaces and lighter blue is approximately near the center depth of the laminate.

The most common failure mechanism shown in both the countersunk and through-holes were shear cracks, which occurs when matrix cracks cause the fibers to become unstable and shear under in-plane compressive load. In comparison to the through-hole specimens, the countersunk holes for both the SCN and DLS test

configuration have most of its damage adjacent to the bottom outer surface of the straight shank portion of the hole and all specimen types exhibit shear cracks. These shear cracks were not found in the conical region. Fibers between the shank and conical interface have support from the conical region, whereas the bottom portion of the shank region is adjacent to a free surface where there is no lateral constraint suppressing fiber buckling. Thus, there is delamination observed in the bottom of shank surfaces than in the conical region.

The pin bending effect motivated the design of the SCN test configuration, which actually eliminates pin bending. Comparing both the countersunk hole SCN and DLS bolted joint static test, it was found that the very similar shear cracks and delamination on the bottom of the straight shank region since this damage feature was present in both cases (i.e., with and without pin bending present). Thus, such damage cannot be attributed mainly to the pin bending (as originally thought to be so). Instead, the DLS configuration suppressed delamination from initiating near the conical and straight shank region of the hole. This interface has large shear stresses and when the pin bears against this conical region, it behaves as a lateral constraint preventing delamination from growing. From microscopy, it is evident that there is more delamination along the interface between the conical and straight shank region for the SCN countersunk hole than in the DLS bolted joint (see Figure 4.47). Additionally, the ultrasonic C-scan shows light blue color around the SCN countersunk hole, which illustrates that there is delamination in near the center of the laminate (see Figure 4.46).

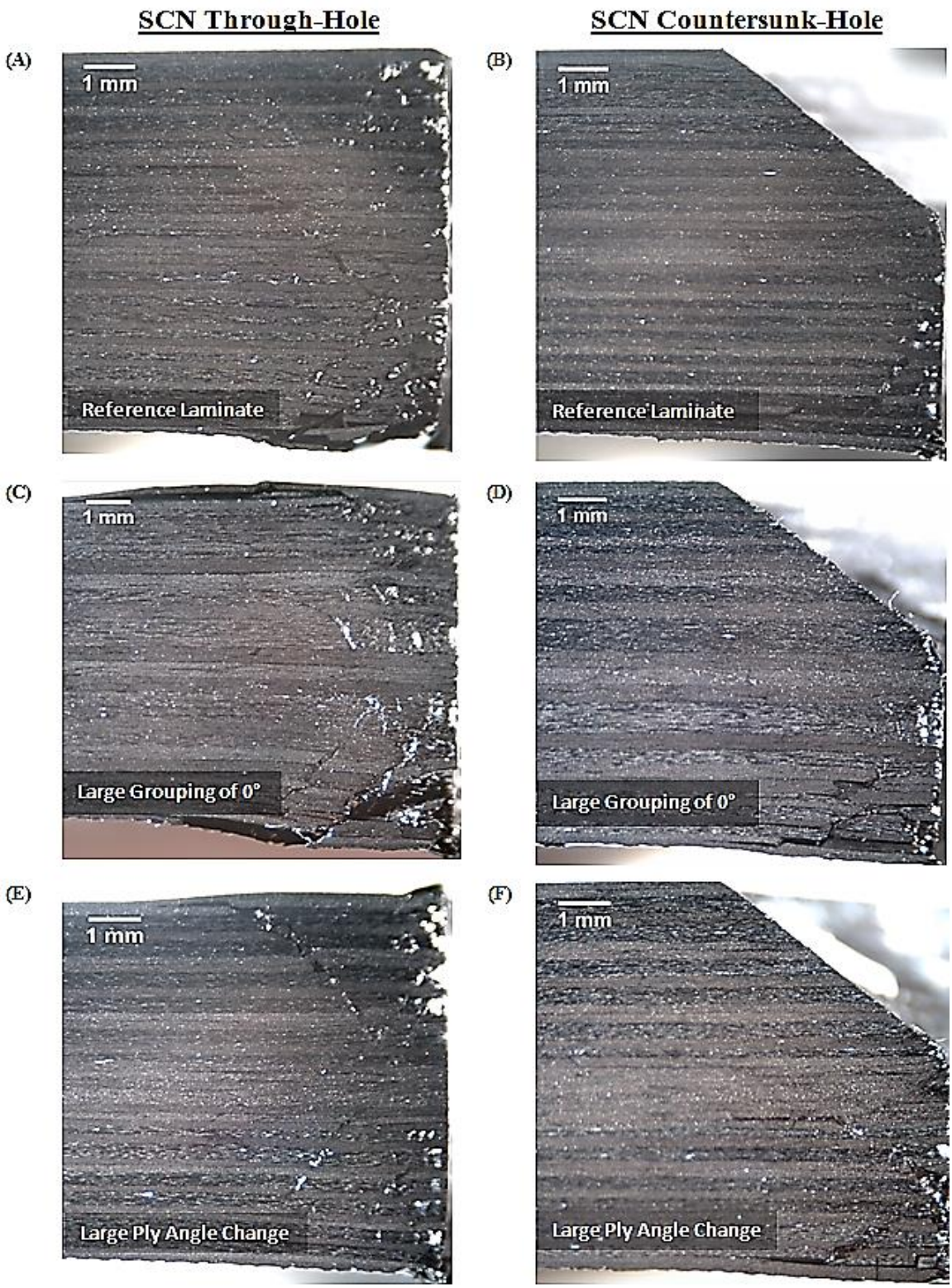

Figure 4.45: Microscopies of SCN through-hole (left) and countersunk (right) specimens after bearing static test.

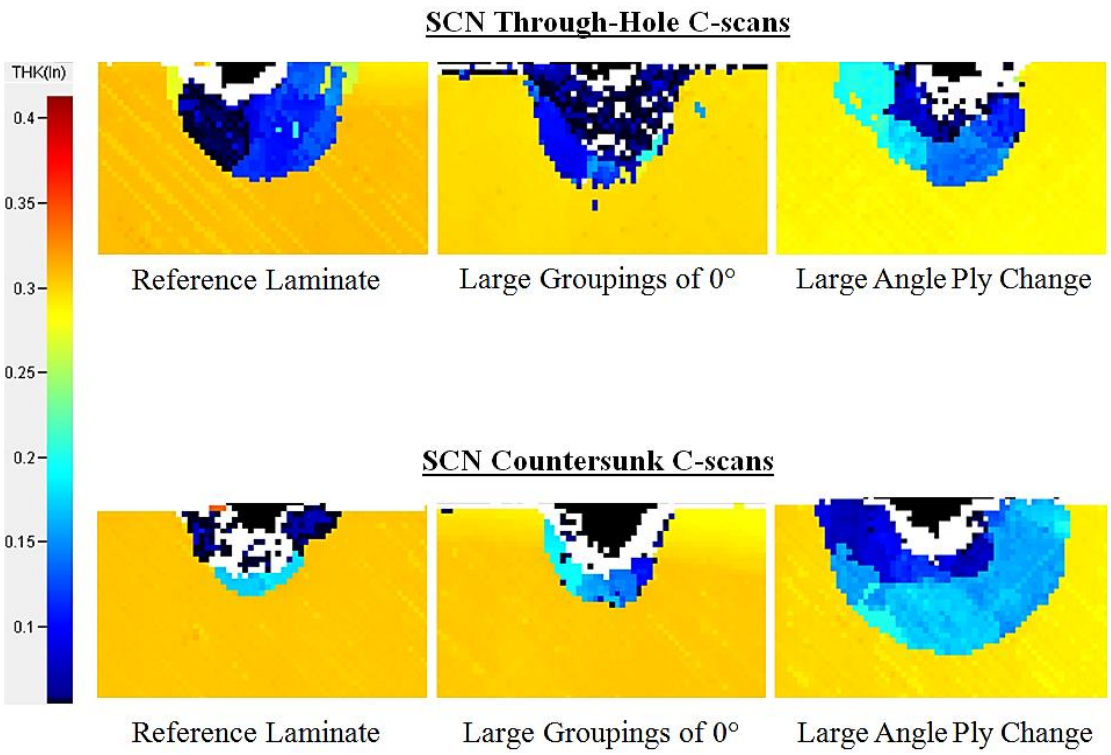

Figure 4.46: Ultrasonic C-scans of SCN through-hole (top) and countersunk hole (bottom) after static test.

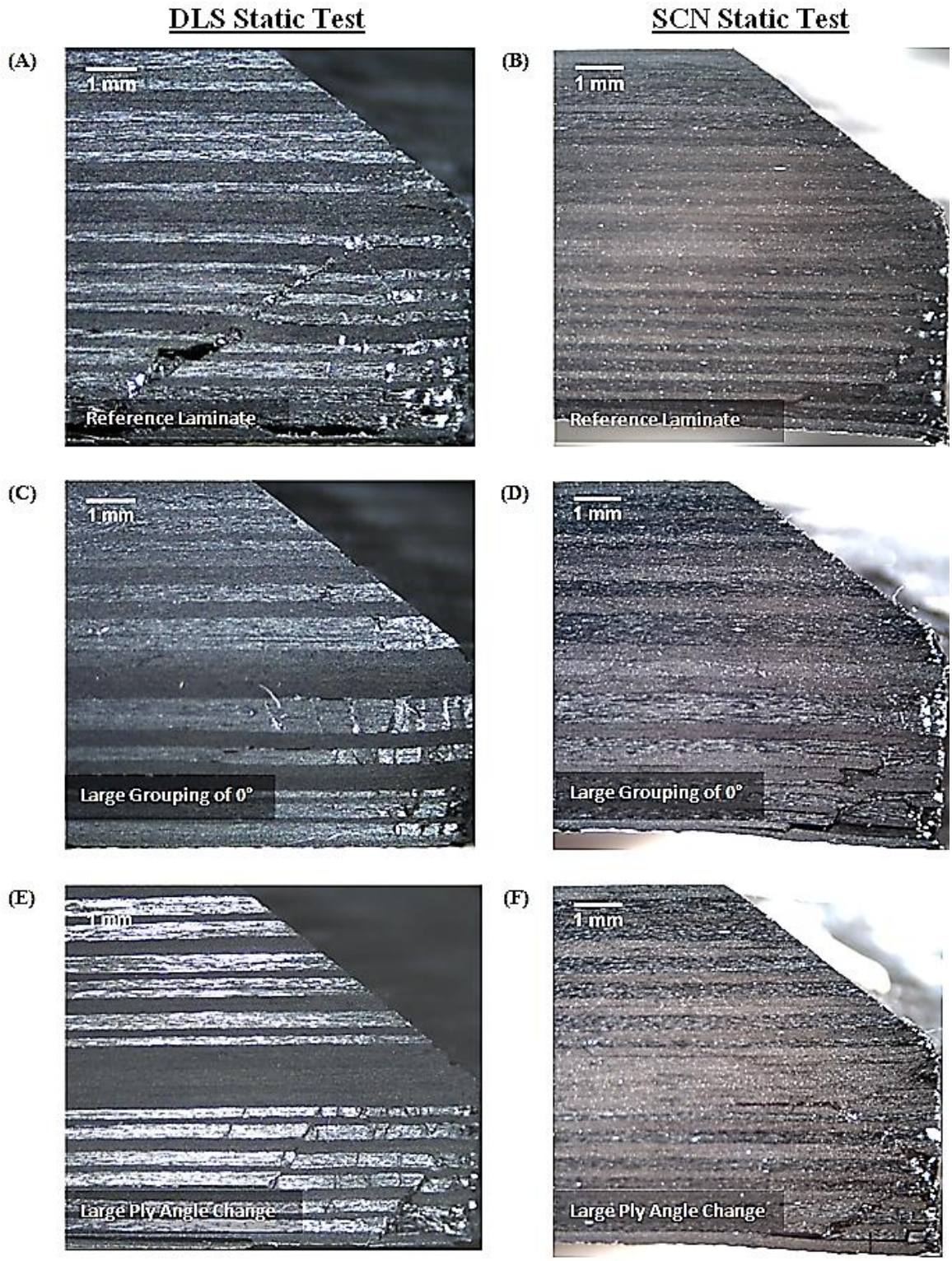

Figure 4.47: Microscopies of DLS versus SCN countersunk specimens after performing static test.

Damage morphologies due to pin bending in SCN static tests for countersunk specimens were compared to the DLS fatigue tests. Microscopy images of the fatigue test showed shear cracks formation near the bottom of the shank region and it was previously assumed to be caused by pin bending (see Figure 4.48). However, the SCN countersunk static test experiment showed similar shear cracks. This is due to the in-plane compressive loads, which created matrix cracks causing the fibers to become unstable. Since the bottom of the shank is a free surface, the fibers have a tendency of more easily fracturing or buckle under compressive loading at this location. Therefore, the pin bending did not affect the shear crack formation found in the fatigue tested DLS specimens. Instead, pin bending may have caused material erosion at the corner of the bottom shank region (see Figure 4.48). Material erosion was not observed in the static tested specimens for both DLS and SCN test configurations. However, it is visible in DLS fatigue tests that were loaded at 50% and 66% ultimate bearing stress. During the loading stage of the fatigue test, the pin may bend and force the already existing shear cracks further into the specimen. Then when the pin unloads, it creates some space between the pin and bolt hole which allow some debris around the corners of the shank region to be removed from the hole bearing surface (see Figure 4.49). In addition, the specimen was removed from the test fixture after a number of cycles to perform ultrasonic C-scan, which may also contribute to the material erosion.

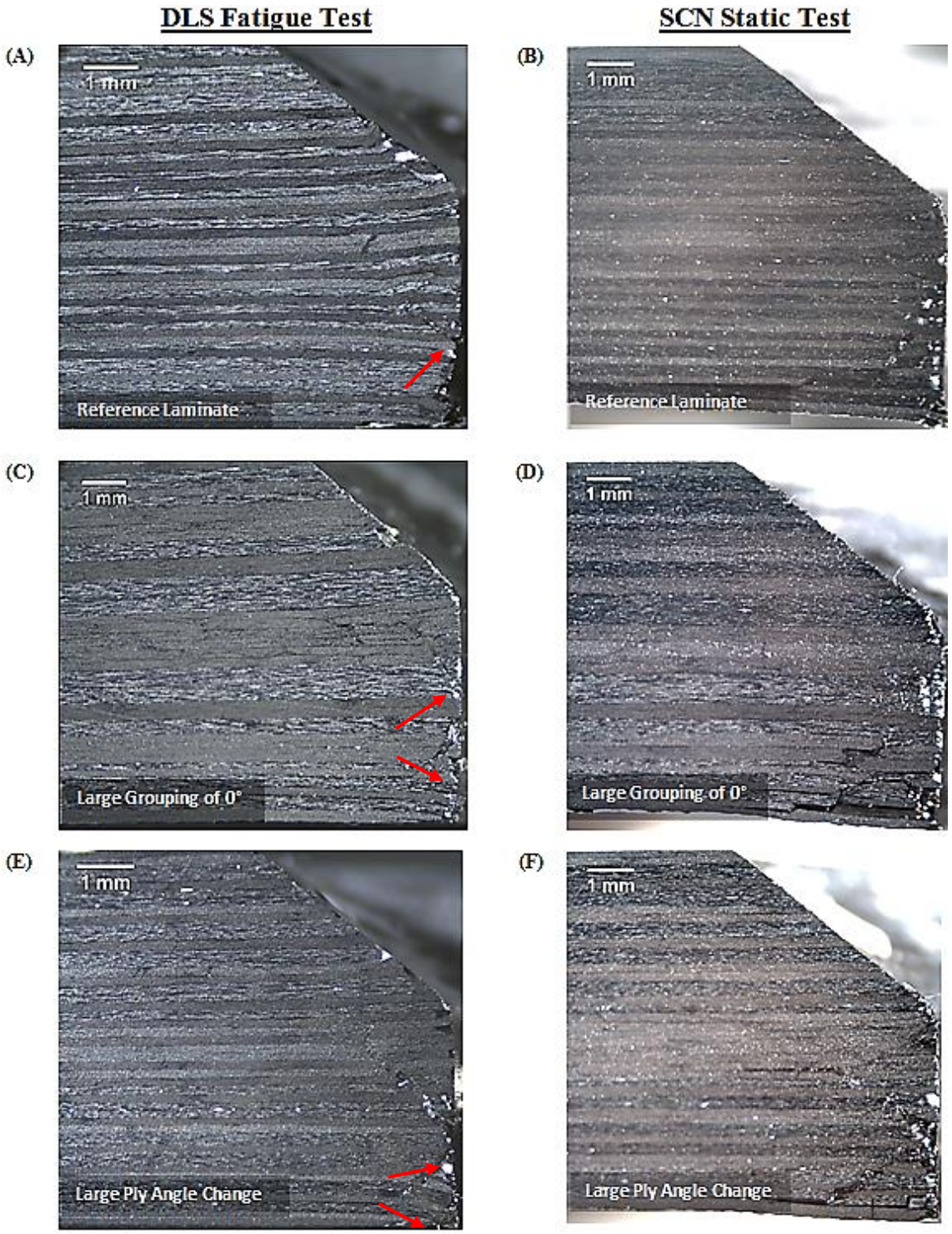

Figure 4.48: Optical microscopies of DLS fatigue versus SCN countersunk static tested speciimen for all laminate types.

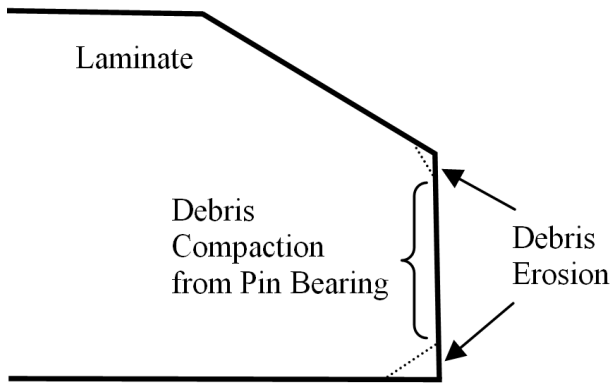

Figure 4.49: Pin bending effect on material erosion during fatigue test

Chapter 4 includes material as it appear in the Investigation of Delamination and Growth Behavior at Fastener Locations in Primary Composite Structures, 2017. Ngo, Mimi and Kim, Hyonny, Proceedings of the 32nd Annual American Society for Composites Technical Conference, 2017 and A Comparative Study on Pin Bearing Effect Under Bearing Static and Fatigue Failure, 2018. Ngo, Mimi and Kim, Hyonny, Proceedings of the 33rd Annual American Society for Composites Technical Conference, 2018. The dissertation author was the primary investigator and author of this paper.

5 FINITE ELEMENT MODELING

Semi-circular notched specimens were modeled using finite element analysis (FEA) to comprehensively understand: (i) stresses developed during static bearing test and (ii) delamination initiation and propagation. Crack initiation and propagation was studied through using the Virtual Crack Closure Technique (VCCT), which is a computational fracture mechanics subroutine implemented in Abaqus, a commercial FEA software [34]. In addition, Hashin failure criteria was included in the model to allow material degradation as delamination grows in order to capture a more realistic bearing failure behavior. The assumptions and limitations of VCCT and Hashin failure criteria will be discussed.

5.1 VIRTUAL CRACK CLOSURE TECHNIQUE (VCCT)

Virtual Crack Closure Technique (VCCT) uses linear elastic fracture mechanics approach to calculate strain energy release rates, with the assumption that the energy required to separate a surface is the same as the energy needed to close the same surface. A delamination can be simulated as a fracture process because a delamination is a separation between plies, which can be seen as a crack in a composite material specifically running between the lamina. In fracture mechanics, strain energy release rate (G) is a quantity that is compared to the critical strain energy release rate (G_c) to determine when crack propagates. When G is greater than G_c, then the crack will grow. Additionally, there are three ways in which loads can be applied on a material to enable crack propagation. In Mode I, forces are applied perpendicular to the crack growth

direction, creating an opening mode. Mode II is when forces produce an in-plane shear stress across the cracks, simulating a sliding mode. Lastly, Mode III is due to an out-of-plane shear stress, similar to a tearing mode (see Figure 5.1).

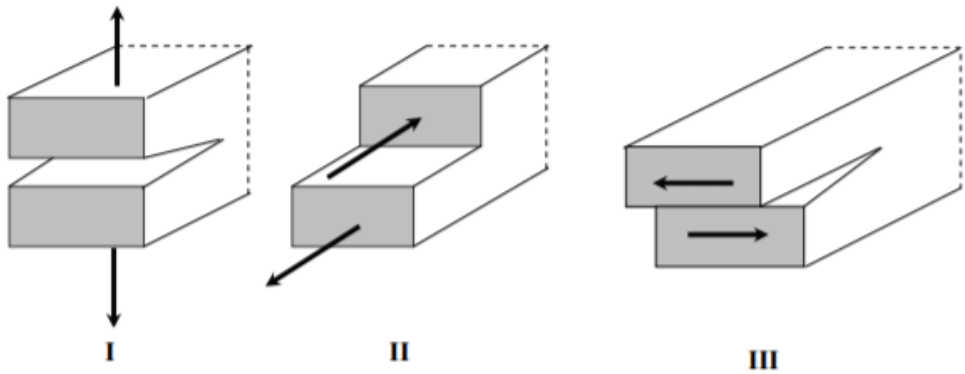

Figure 5.1: Three frature modes including Mode I (opening mode), Mode II (sliding mode), Mode III (tearing mode) [30].

In VCCT, it is assumed that the strain energy released when a crack is extended by a certain amount, requires the same amount of energy to close the crack by the same amount. Equation 5.1 is used to calculate the strain energy release rate in the pure Mode I case for a 2D shell element model. However, Abaqus is also capable of performing VCCT in 3D solid element models. From this equation, a crack extends from point *i* to *j*, where the initial crack tip is at nodes 2 and 5 (see Figure 5.2). The force and displacement at these nodes can be used to calculate the strain energy release rates for all three fracture modes (see Figure 5.3). When the strain energy release rate at nodes 2 and 5 is greater than the material fracture toughness then the node will release to propagate the crack. Although Equation 5.1 only illustrates pure Mode I, similar equations can be

used to calculate pure Mode II and Mode III. This is an iterative process that is performed at each node and Abaqus uses either Paris Law, BK Law or Reeder Law to calculate an equivalent strain energy release rate G_{equiv}, which is a mixed-mode strain energy release rate. More details on these laws can be found in literature by Wu and Reuter [31], Benzeggagh and Kenane [32], and Reeder, et al, [33]. In general, a mixture of more than one fracture mode causes crack propagation, particularly for delamination. Thus, in Abaqus users can select to use either of those laws to calculate the equivalent strain energy release rate (G_{equiv}) and compare it to the critical equivalent value (G_{equivC}).

In this research, the BK law was used because the required input values for the selected material is readily available in literature and it delivers an adequate description of the fracture locus for a wide range of composites [35]. Also, BK law is equivalent to the Reeder Law when the critical strain energy release rate of Mode II is equivalent to Mode III (see Equations 5.2 and 5.3). Paris law was not used in this analysis because in Abaqus it requires more inputs which are not readily available.

$$\frac{1}{2}\left(\frac{v_{1,6}F_{v,2,5}}{bd}\right) = G_I \tag{5.1}$$

Where,

G_I is the Mode I strain energy release rate

b is the width of the element at the crack

d is the element length at the crack tip

$F_{v,2,5}$ is the vertical force between nodes 2 and 5

$v_{1,6}$ is the vertical displacement between nodes 1 and 6

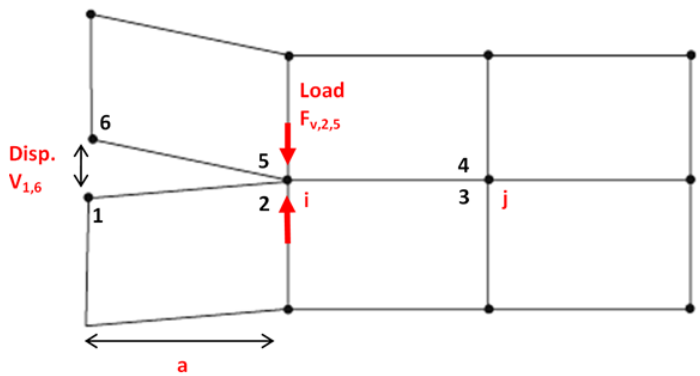

(A) Crack closed

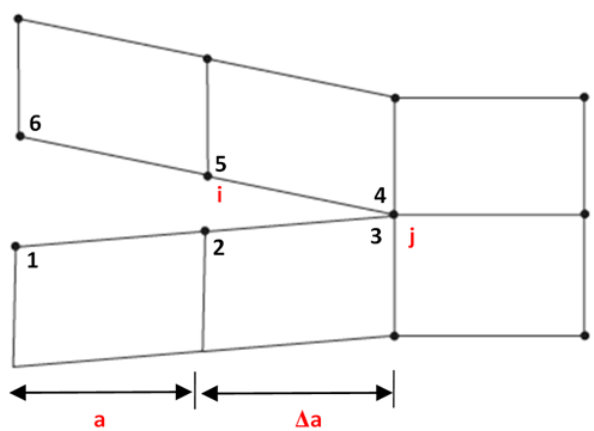

(B) Nodes 2 and 5 released to open crack

Figure 5.2: Crack extension from node release in Mode I strain energy release rate calculation [34].

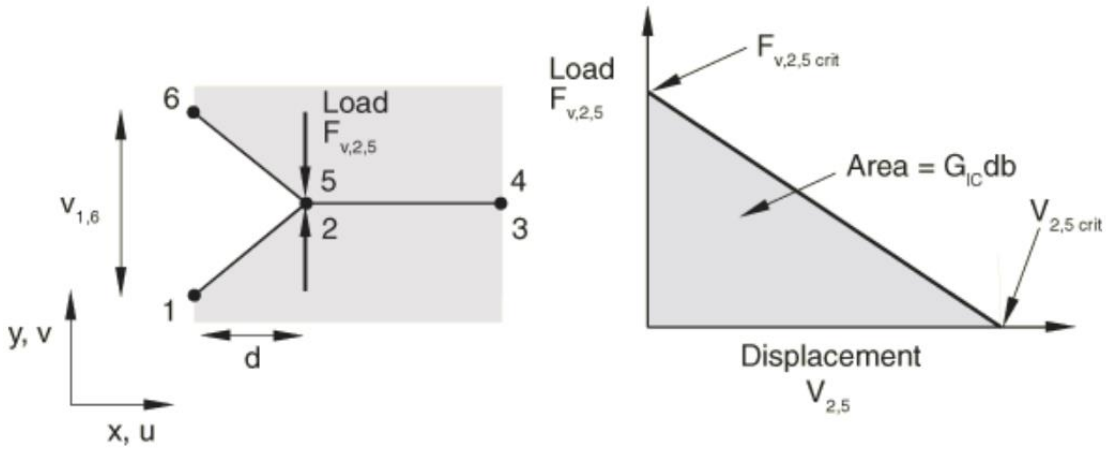

Figure 5.3: Area under the force versus displacement plot from nodes 2 and 5 is used to calculate strain energy release rates [34].

<u>BK Law:</u>

$$G_{equivC} = G_{IC} + (G_{IIC} - G_{IC})\left(\frac{G_{II}-G_{III}}{G_I+G_{II}+G_{III}}\right)^{\eta} \tag{5.2}$$

<u>Reeder Law:</u>

$$G_{equivC} = G_{IC} + (G_{IIC} - G_{IC})\left(\frac{G_{II}-G_{III}}{G_I+G_{II}+G_{III}}\right)^{\eta} + (G_{IIIC} - G_{IIC})\left(\frac{G_{III}}{G_{II}+G_{III}}\right)\left(\frac{G_{II}-G_{III}}{G_I+G_{II}+G_{III}}\right)^{\eta} \tag{5.3}$$

5.2 Semi-Circular Notched Model Description

FE analysis was performed for the SCN model to provide information on the stress profile on the pin-bearing surface of the hole, progressive failure modes and strain energy release rates. These outputs can assist in developing a better understanding of why bearing damage only occurs in certain regions, where damage initiates and propagate, and the location of stress concentration through the laminate thickness.

The SCN specimen was modeled in Abaqus for all three laminate types with a steel alloy pin. The composite specimen and pin assembly is shown with geometric dimensions in Figure 5.4. The specimen was modeled with a total number of 48 plies and uses AS4/3501-6 linear elastic material properties for the composite laminate (see Table 5.1). In order to prevent a sharp tip mesh geometry at the hole edge between the conical and straight shank interface, the conical region instance was created with 26 plies and the straight shank region was developed with 22 plies. The laminate was partitioned to have two plies per element through the thickness in the straight shank region and 26 plies in one element for the conical region (see Figure 5.5).

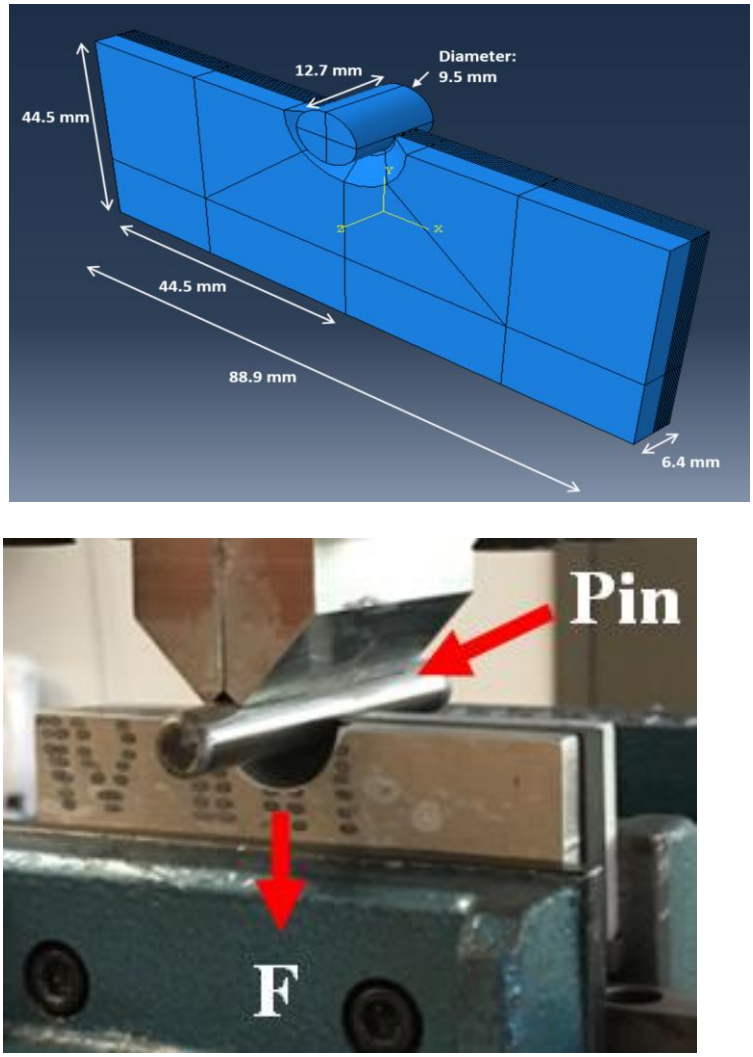

Figure 5.4: FE model of SCN specimen with steel pin assembly (top) representing the setup for SCN test configuration without the aluminum plates on both sides (bottom).

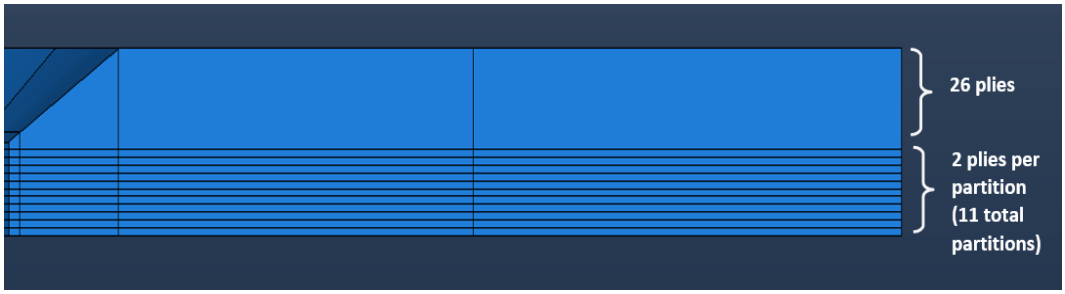

Figure 5.5: Semi-circular notched FE model illustrating how the plies were partitioned through thickness of the laminate.

Table 5.1: Material properties of AS4/3501-6 carbon fiber reinforced epoxy composite.

Unidirectional Carbon/Epoxy Material Properties (AS4/3501-6)	
E1	147 GPa
E2	10.3 GPa
E3	10.3 GPa
G12	7 GPa
G23	3.7 GPa
G13	7 GPa
v12	0.27
v23	0.54
v13	0.27

FE analysis was performed on an SCN specimen with pin assembly having and damage implemented in the model to study bearing stress distribution on the bolt-bearing surface. These bearing stress profiles along with the strain energy release rates will aid in better understanding how delamination initiates and arrest. In the SCN FE model used to with no damage, a three-dimensional (3D) continuum solid (C3D8R) element was used to investigate the inter-laminar shear stress. In general, delamination initiation and propagation are influenced by inter-laminar shear stresses, thus it is necessary to investigate shear stresses (S23 and S13).

A second FE analysis was performed on SCN specimen having both Hashin failure criteria and VCCT implemented. Hashin damage in Abaqus is not compatible with 3D stress elements, thus an 8-node quadrilateral continuum shell with reduce integration

and hourglass control (SC8R) element was used in the model. When using VCCT in Abaqus, pre-cracks must be created in the model before running the analysis. The pre-crack begins 0.5 mm away from the hole edge surface and between plies 26- 27, plies 27-28, plies 46-47 and plies 47-48 (see Figure 5.6). The first two pre-cracks were placed near the interface between the conical and straight shank region and the second two pre-cracks were placed on the bottom surface of the straight shank region. The placement of these pre-cracks were based upon observations made through optical microscopy. Delaminations were commonly found in the lower bottom region of the straight shank and with high load, delamination can be found between the conical and straight shank interface (see Figure 5.7).

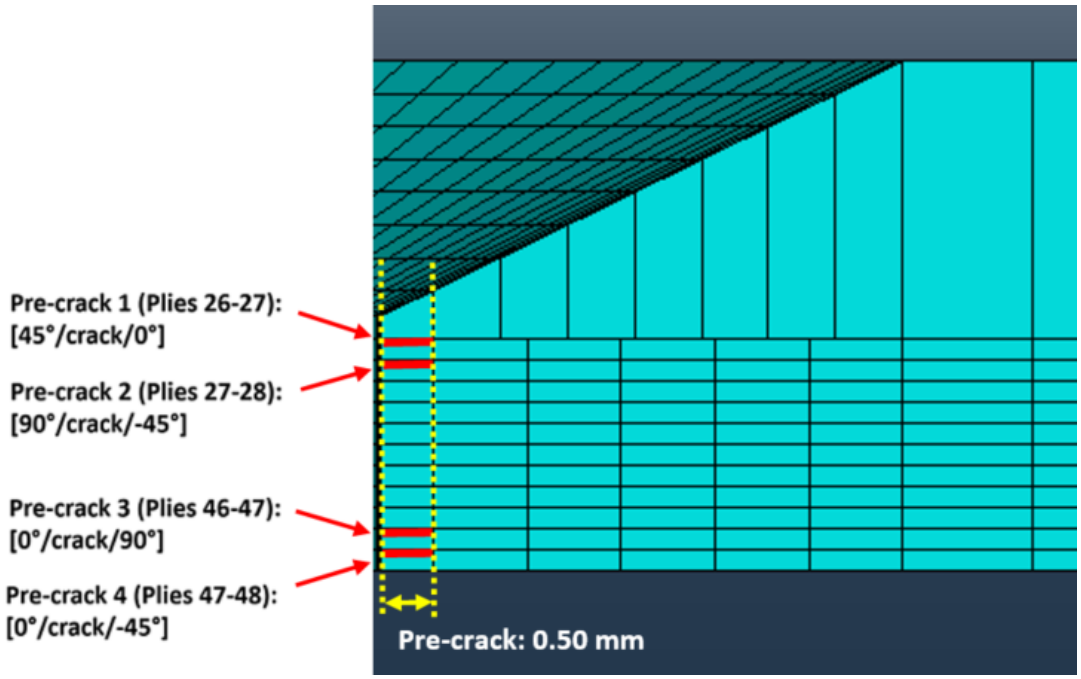

Figure 5.6: FE model of SCN specimen illustrating pre-crack locations for using VCCT in Abaqus.

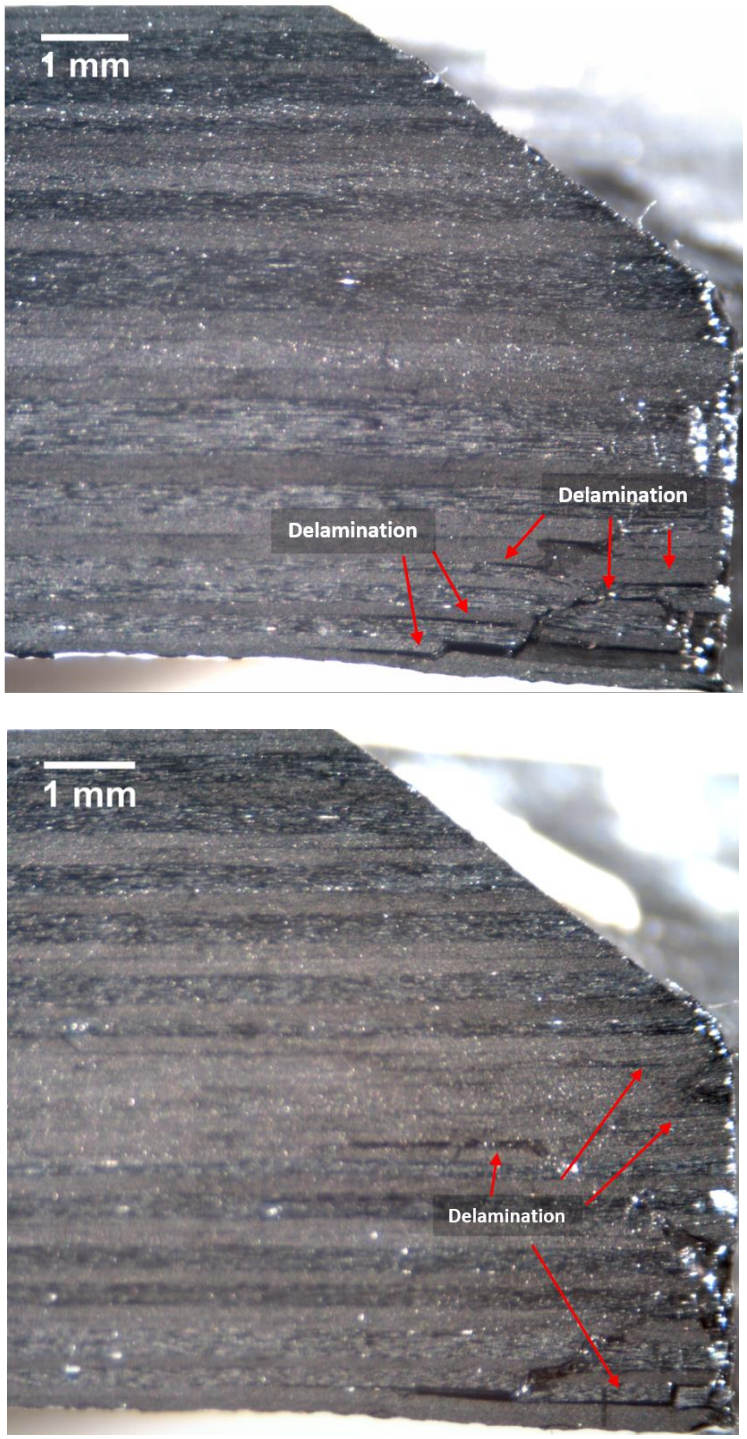

Figure 5.7: Optical microscopy from SCN specimens showing delaminaiton locations, which was used to determine the placements of pre-cracks in the FE model.

Table 5.2: VCCT input parameters for AS4/3501-6 composite material.

VCCT Parameters	
G_{IC}	81.6 N/m^2
G_{IIC}	554 N/m^2
G_{IIIC}	554 N/m^2
η	1.75

Table 5.3: Hashin damage input parameters for Abaqus.

Hashin Damage Inputs	
Longitudinal Tensile Strength, F_{1t}	2280 MPa
Longitudinal Compressive Strength, F_{1c}	1725 MPa
Transverse Tensile Strength, F_{2t}	57 MPa
Transverse Compressive Strength, F_{2c}	228 MPa
Longitudinal Shear Strength	76 MPa
Transverse Shear Strength	76 MPa
Damage Evolution	
Longitudinal Tensile Fracture Energy	8,850,822 N/m^2
Longitudinal Compressive Fracture Energy	8,850,822 N/m^2
Transverse Tensile Fracture Energy	1770 N/m^2
Transverse Compressive Fracture Energy	1770 N/m^2

Additionally, default parameters for automatic stabilization and contact control were used to assist in the problem solution convergence. Particularly, when using VCCT, implementing multiple cracks through the laminate thickness will cause convergence issue. Boundary conditions on the SCN specimen and pin assembly are shown in Figure 5.8. The specimen is fixed in the 2-direction (see Figure 5.8 for axis) on the bottom surface to prevent rigid body motion and the two perpendicular sides are fixed in the 3-direction to prevent out-of-plane displacement. This setup mimics the aluminum plates and vice gripping constraint during the experimental setup. Additionally, the pin was constrained such that it is fully supported and can only move in the bearing direction towards the bolt-hole surface. A downward displacement of 1 mm was applied to the pin, replicating a displacement control from the MTS machine onto the specimen during the static test.

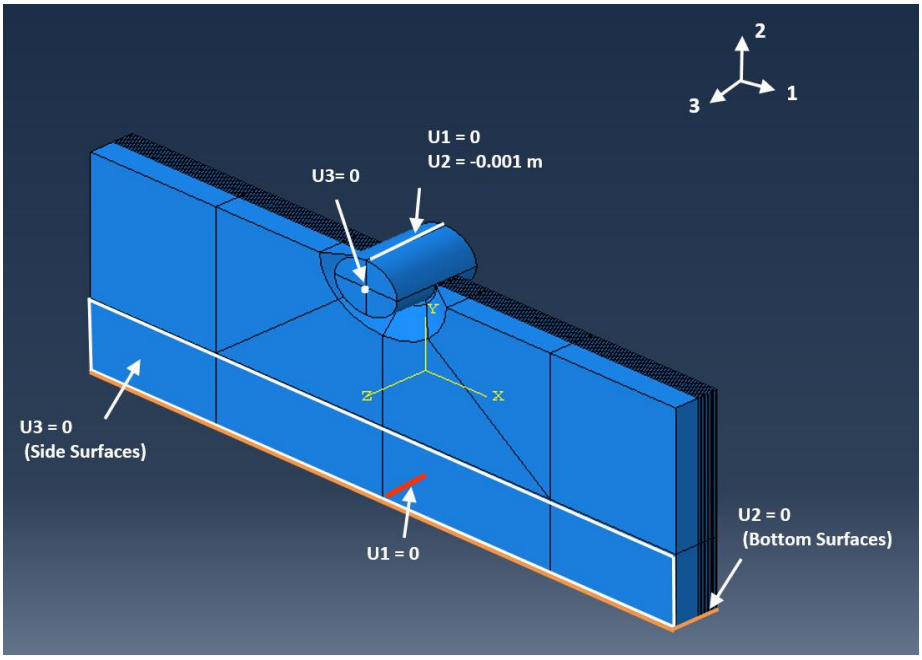

Figure 5.8: Boundary conditions and displacement applied to the SCN FE model in Abaqus.

5.3 Preliminary Studies

Preliminary studies were performed for SCN specimens: (i) mesh study using VCCT and Hashin failure criteria and (ii) model verification through validating VCCT modeling method for composite in Abaqus with a published benchmark problem, performing a mesh study to show convergence of stiffness, and correlating results from FEM to experimental data.

The mesh sensitivity study was performed on the SCN specimen having a layup from the reference laminate. Both Hashin damage and VCCT were implemented to the model. In order to prevent the initial crack tip length from influencing the results when

changing the mesh size, the pre-crack was assigned to initiate at 0.5 mm away from the hole edge. For all mesh studies, the pin global mesh size is 1 mm and the SCN specimen global mesh size is 2 mm at locations away from the cracks. The location near the crack tip and conical region varies in mesh size from 0.6 mm to 2 mm (see Figure 5.9). Figure 5.10 shows the load versus displacement for the different mesh sizes. Through observations, the mesh size of 2 mm and 0.60 mm shows a greater deviation compared to the 0.8 mm and 1 mm. This may indicate that there is an optimum mesh size when using VCCT and Hashin damage criteria in the FE model. Thus, the mesh size of 0.80 mm was used in all the analysis for the SCN specimen with damage implemented in the model. For specimens with no damage, a mesh size of 1 mm was used to reduce analysis cost.

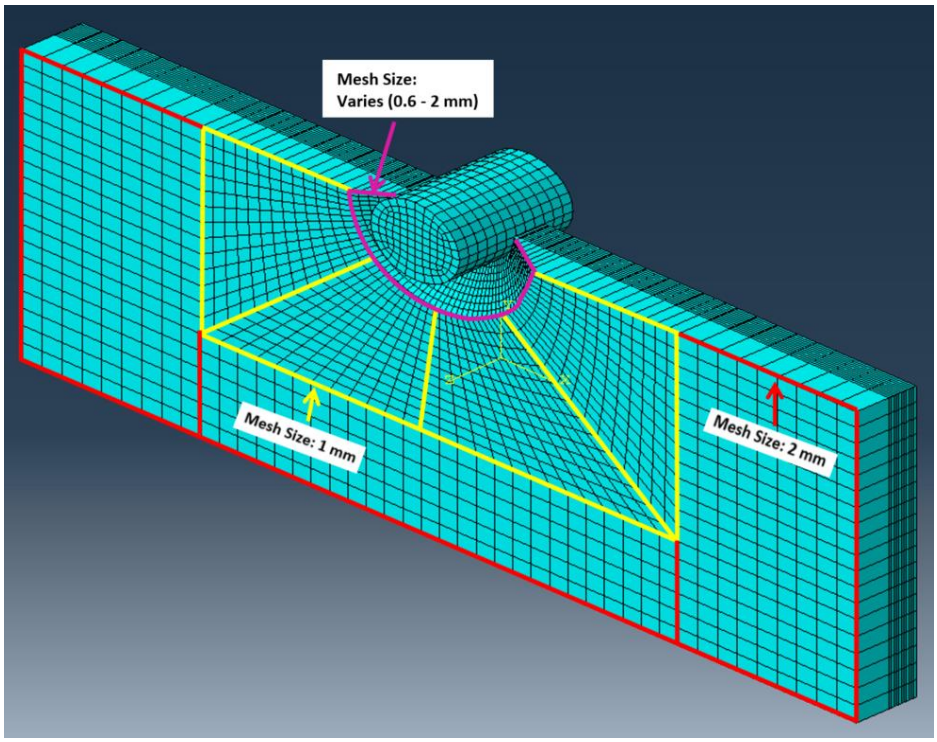

Figure 5.9: Element size for mesh sensitivity study. The mesh size was changed in the radius geometry near the crack tip.

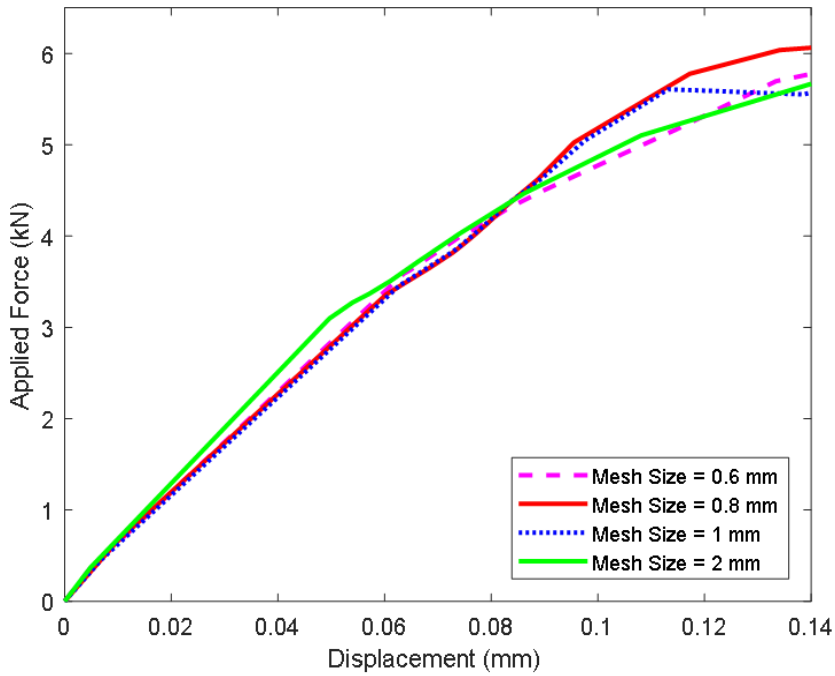

Figure 5.10: Mesh sensitivity study for SCN FE model with VCCT and Hashin damage included. Mesh size 0.8 mm and 1 mm show closer convergence behavior.

Model verification was performed through two process. The first step was to verify that the method of applying VCCT in composite material is accurate through performing a benchmark study case on a DCB model by Ronald Kreuger [36]. The strain energy release rate and critical load at which the delamination propagates match with the benchmark study (see Figure 5.11). Thus, verifying that the process for developing a model using VCCT in Abaqus can be used in the SCN FE model. After completing this first step, the same procedure for implementing VCCT was applied to the SCN FE model.

Two SCN FE models with the same Abaqus input variables were created with and without damage. Abaqus output for this FE model without damage used to correlate with the experimental test data (see Figure 5.12). The result shows that the FE model did not

correlate with the experimental data. Reasons for discrepancy in the stiffness may be due to manufacturing defects that were not modeled, material properties, test machine compliance, and boundary condition definitions. In the FE model, the side surfaces were constrained such that there is no out-of-plane displacement (see Figure 5.8). However, on the experimental test setup, the vise holding the aluminum side plates and specimen was clamped with the same pressure as “finger-tight”. Thus, as load increases, there may be some movement between the aluminum plates, specimen and vice that was not accounted for in the FE analysis. Additionally, displacement from the experimental data was taken from the crosshead displacement of the MTS test machine, which includes the compliance of the machine. The material property inputs were taken from literature instead of performing coupon testing on the specimens, which could also influence the FE model results. Although the FE model and experimental data did not show good agreement in stiffness, the model can still provide insights on stress concentration at the bolt-bearing face during loading. Bolted joint of composite material, particularly in the study of bearing failure is a very complex problem that will require more time to develop an accurate FE model to correlate with the experimental data. However, one is only using FE models to predict bearing failure in composite material, high fidelity results are difficult to achieve by only analysis. As presented in this chapter, many issues may arise in modeling that can influence the results.

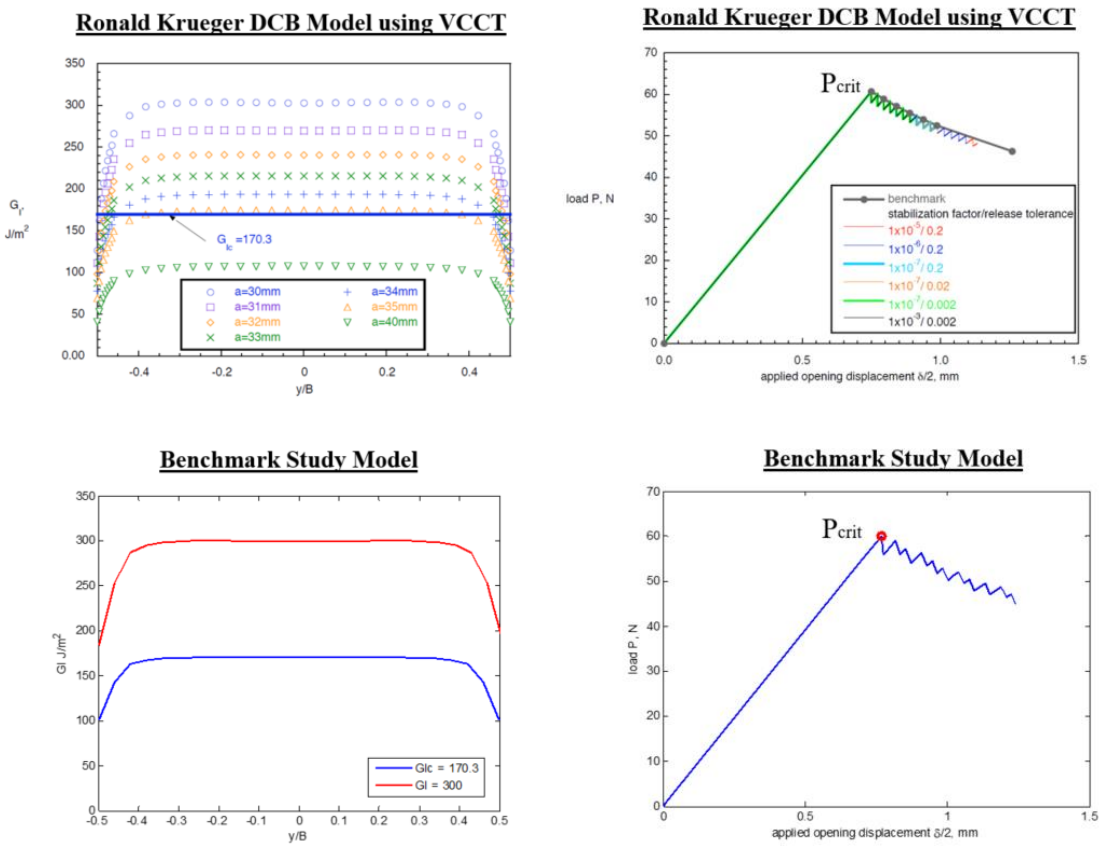

Figure 5.11: Benchmark study case performed on DCB model to verify VCCT process in Abaqus is correct. Strain energy release rate (left) and critical load at crack initiation (right) was matched with Ronald Kreuger's DCB model.

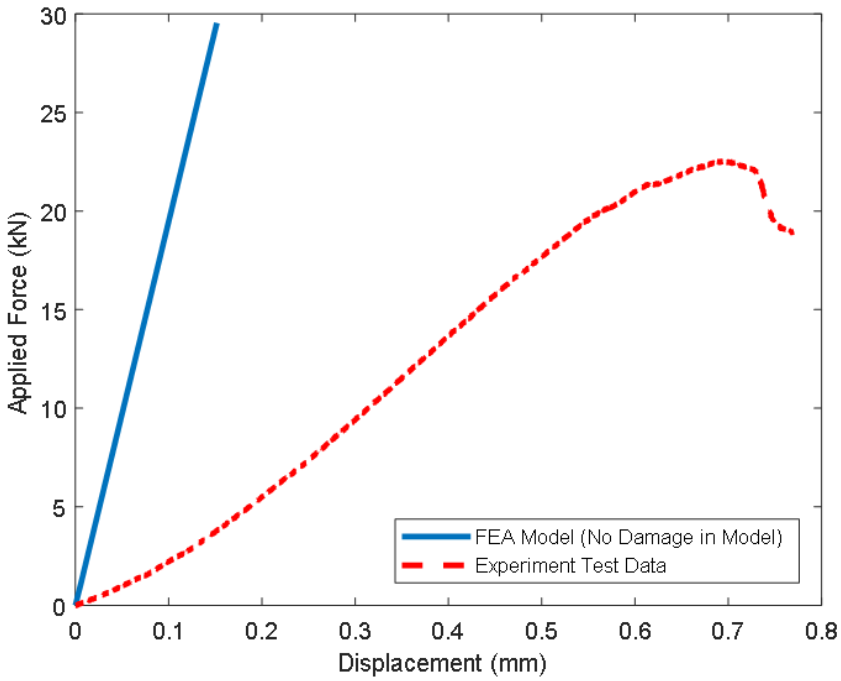

Figure 5.12: FE model of SCN specimen with and without damage compared to experimenta test data for model verification.

5.4 SCN FE Model with No Damage

FE analysis was performed on an SCN model with no damage using a 3D solid continuum shell element (C83DR) to develop a better understanding of stress distribution on the bearing face. However, the stiffness of the model was not able to correlate with the experimental data. Thus, values presented hereon will not be used to make any quantitative conclusions, but instead, this model will be used to provide insights on stress concentration locations. Information on stress concentrations can show the most likely location where bearing damage will occur first and how it may propagate with increasing loads.

Bearing stress in Figure 5.13 shows stress concentration located at the conical region of the laminate. In comparison to observations from the SCN microscopy image for the same laminate type, the major bearing damage occurs near the bottom of the shank (see Figure 5.7). Both shear cracks and delamination were found mostly on the bottom of the shank, but only delamination was observed between the straight shank and conical interface. This possibly indicates that bearing damage initiates between this interface and the shear cracks would travel downwards towards the outer edge of the laminate surface. As the shear cracks propagate through the laminate thickness, the continuous compressive load from the pin can initiate delamination. Thus, both delamination and shear cracks are mainly found on the bottom of the shank region. This hypothesis can be further verified with a validated FE model. However, these current results show that bearing stresses from FE model can assist in explaining progressive damage in composites.

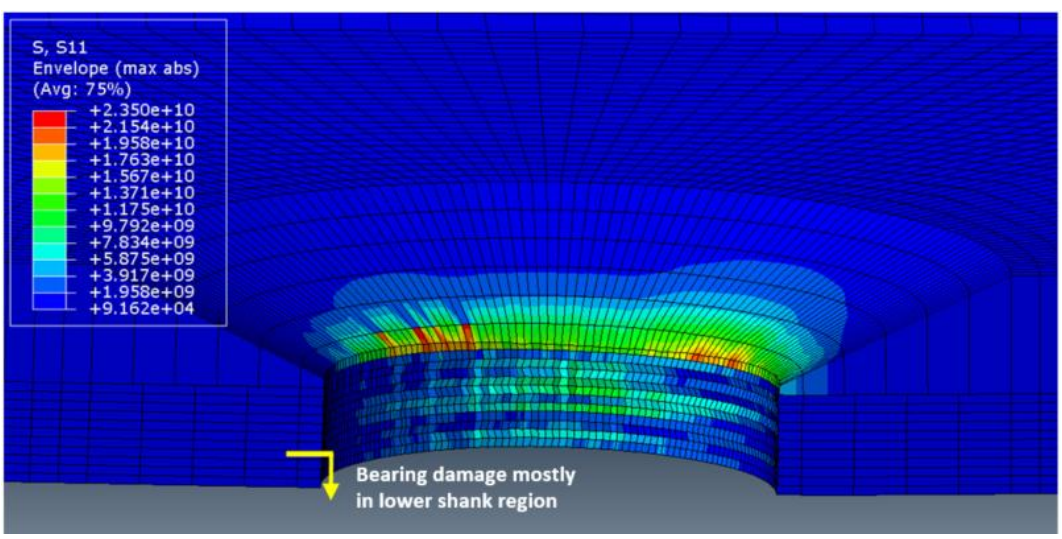

Figure 5.13: Contour plot of the bearing stress distribution on the loading direction. Units for stress displayed is Pa.

Transverse shear stress (S13) is critical to delamination initation, whereas transverse normal (through the thickness, S33) stress influences inter-laminar delamination propagation. Thus, both of these results are examined in the FE analysis. The stress concentrates in the middle section of the pin-bearing surface near and between the conical and shank region interface in both contour stress plots (see Figure 5.14 and Figure 5.15). This result may explain why delamination was observed between the conical and shank region because the abrupt changed in geometry at the intersection may influence the transverse shear stresses. On the contrary, at the bottom of the shank region where the surface is free, there is very little shear stress.

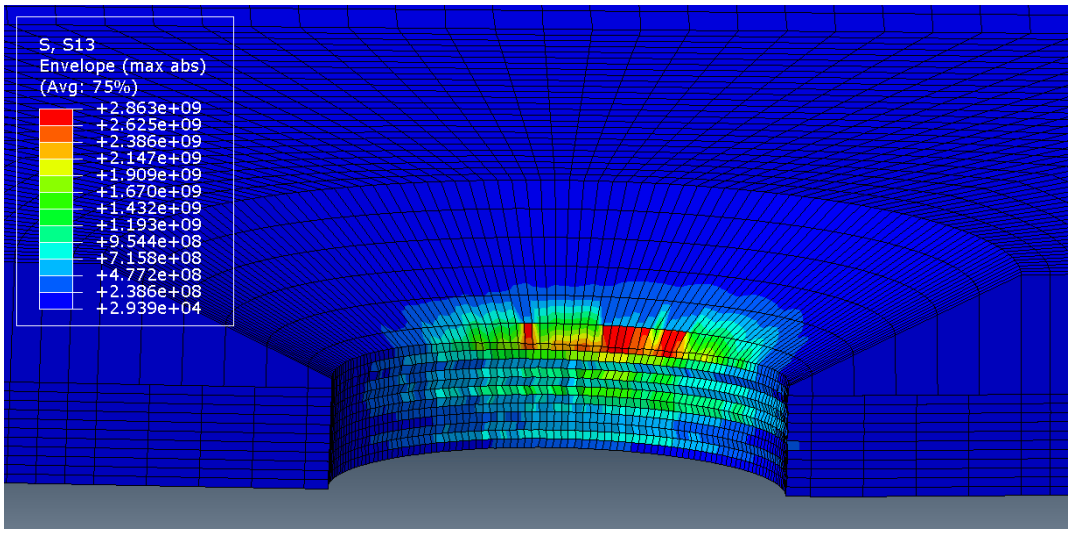

Figure 5.14: Transverse shear stress of SCN FE model show greatest shear stress at the center of the pin-bearing surface on the conical region. Units are in Pa.

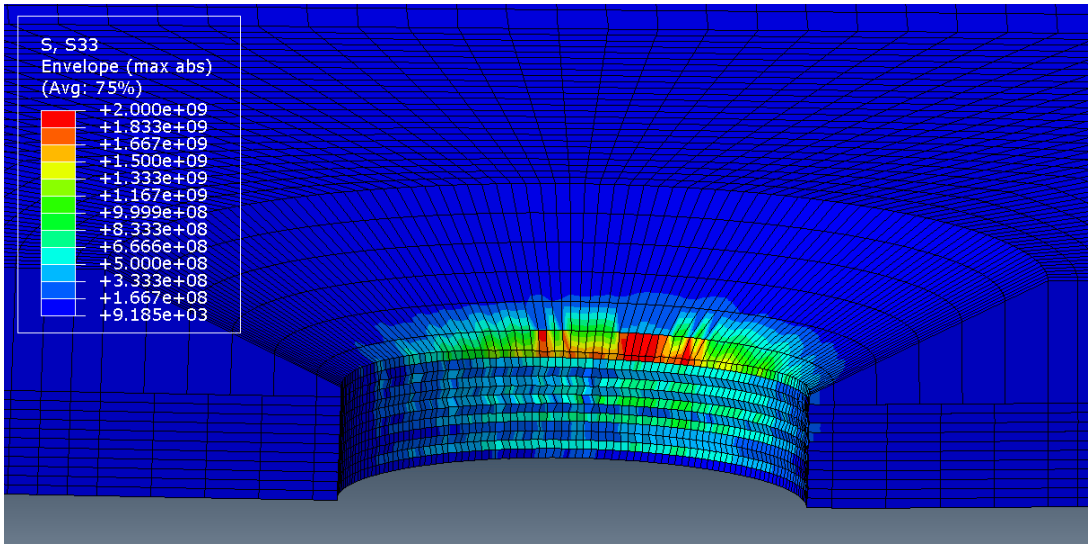

Figure 5.15: Transverse normal stress on the pin-bearing surface of the SCN laminate. Stress units displayed is Pa.

5.5 Bearing Stress with Hashin Failure Criteria and VCCT

SCN FE model with pin assembly was modeled with Hashin damage and VCCT to allow delamination initiation and propagation. The pre-cracks were placed in locations that delamination were commonly observed through optical microscopy images (see Figure 5.7). Figure 5.16 and Figure 5.17 show the Hashin fiber compression and tension failure modes in the SCN FE model. These failure maps indicate that fiber fractures or delamination failure most likely occur near the intersection between the conical and shank region. This may indicate that fiber fracture initiates near this this intersection and cause a series of shear cracks that propagates towards the free edge surface of the laminate (bottom of shank region) (see Figure 5.20). Figure 5.18 and Figure 5.19 shows plot contour of the matrix compression and tension failure, respectively. Matrix

compression failure occurs through the thickness of the laminate on the pin-bearing surface, but there is more damage near the conical and shank intersection. Both matrix compression and tension failure occur before delamination initiates. Thus, understanding where matrix cracks occur can indicate where delamination will most likely develop in the composite.

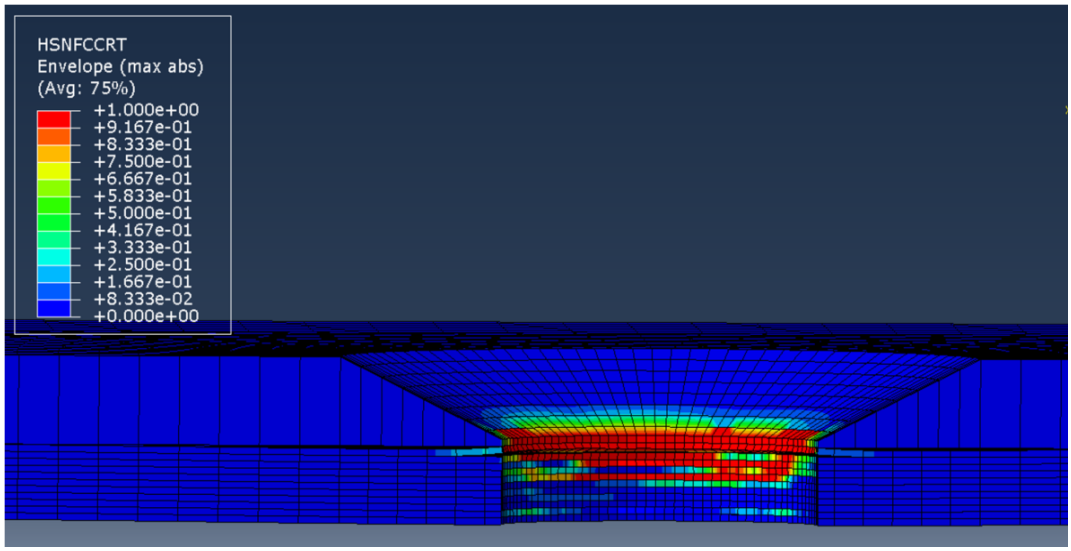

Figure 5.16: Hashin fiber compresison failure, which show locations where pin loading has the most affect on the bolt-bearing surface. Red color (value of 1) indicates damage has occured, whereas blue color (value of 0) means there is no damage.

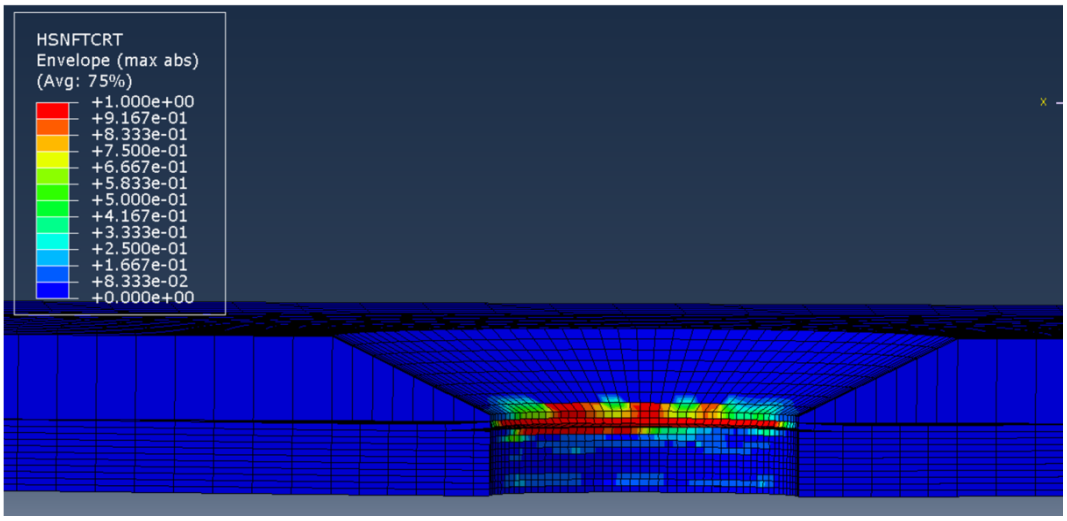

Figure 5.17: Hashin fiber tension failure image illustrating locations where fibers have high tensile stress. Red color (value of 1) indicates damage has occured, whereas blue color (value of 0) means there is no damage.

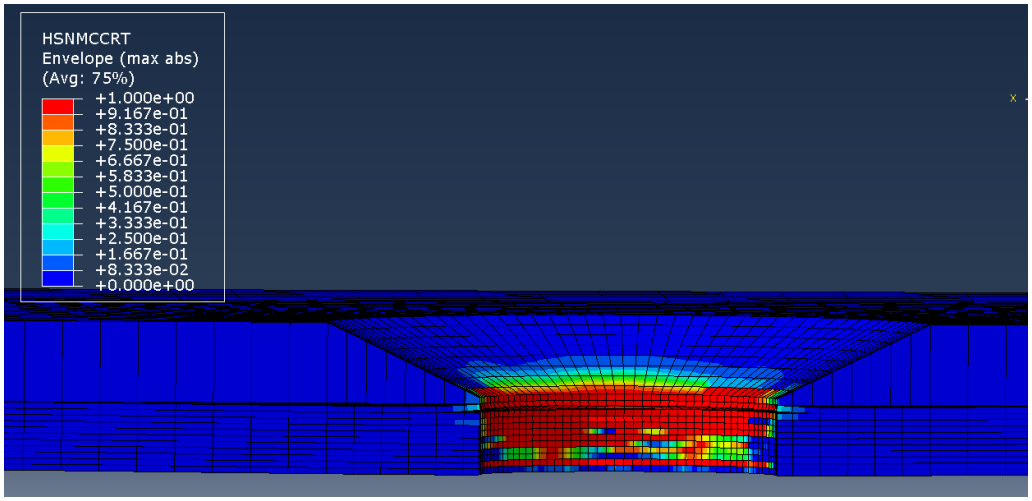

Figure 5.18: Hashin matrix compressiom failure with four pre-cracks, which occurs first before other failure modes occur (i.e. fiber tension and compression). Red color (value of 1) indicates damage has occured, whereas blue color (value of 0) means there is no damage.

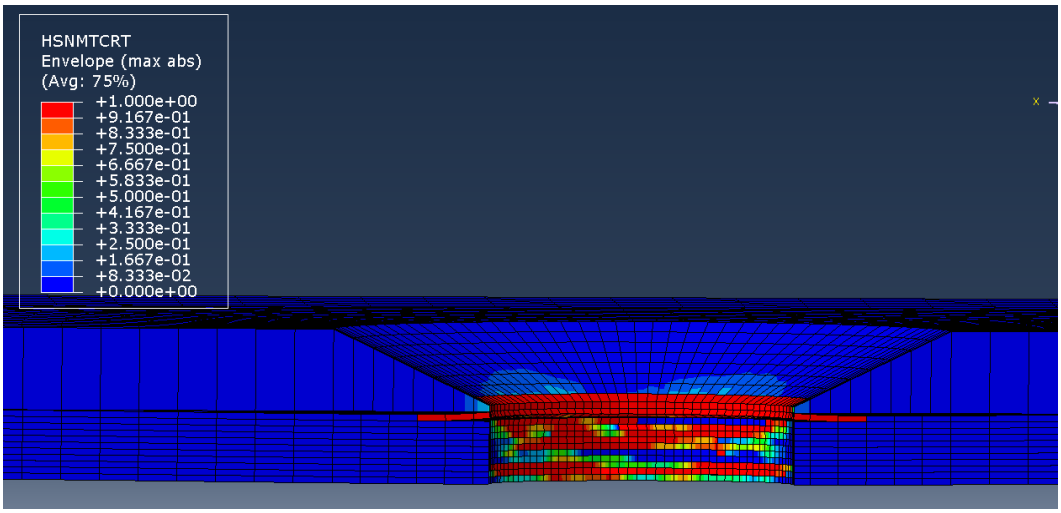

Figure 5.19: Hashin matrix tension failure in indicating tensile stress in matrix is greatest where delamination occurs. Red color (value of 1) indicates damage has occured, whereas blue color (value of 0) means there is no damage.

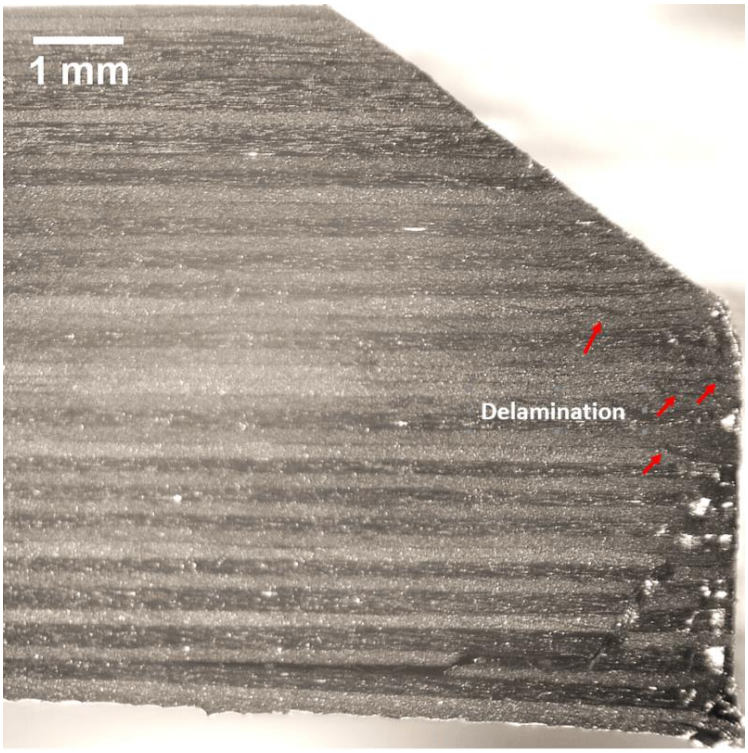

Figure 5.20: Microscopy of the reference layup type specimen showing location of delamination. This supports the damage observed in the FE model.

Delamination initiates in later time increment compared to the Hashin damage, which is expected because matrix cracks and fiber fractures were found to occur before delamination through the progressive damage study for bearing failure. Results from the VCCT model show that delamination occurs at crack 1 first, which is the location between the conical and shank region (see Figure 5.21). This figure shows the bond state of the laminate, thus each image represents the delamination surface. The red color represents that the laminate is fully bonded, whereas the blue color means the nodes have fully debonded (delamination). On the bottom of the laminate, there is blue color on the last nodes because those nodes were not bonded prior to running the analysis. Nodes where there is a fixed boundary condition can cause analysis issues if those nodes are also assigned to the bonded set. Figure 5.22 shows the strain energy release rate plot from Mode I before the crack initiates. This was greater compared to the strain energy release rates of the other cracks. The plot shows two peaks along the crack path, which corresponds with the two node release locations on Figure 5.21. Figure 5.23 shows the final delamination state of cracks 1 and 2 prior to terminating the analysis. Cracks 3 and 4 did not propagate. These results support the hypothesis that matrix crack and delamination occurs between the conical and shank region first. However, this is only valid for this SCN configuration because the boundary condition for the DLS bolted joint is different. In addition, the SCN experimental data show more delamination between the shank and conical region because there is very little lateral support from washers near the bolt-hole region. This is even more evident in modeling because the FE model has no boundary condition near the bolt-hole region and the abrupt change in the geometry of the joint makes the conical region more likely to have stress concentrations. Figure 5.24

shows the bearing stress S11 along the path of the pin bearing surface, which shows the stress concentration location on the pin bearing surface. Although, the stress values cannot be used to make any quantitative conclusions at this time, since the model does not correlate well with the experimental data, it can provide qualitative insights on stress concentration regions. In this case, bearing stress is greatest, between the conical and shank region.

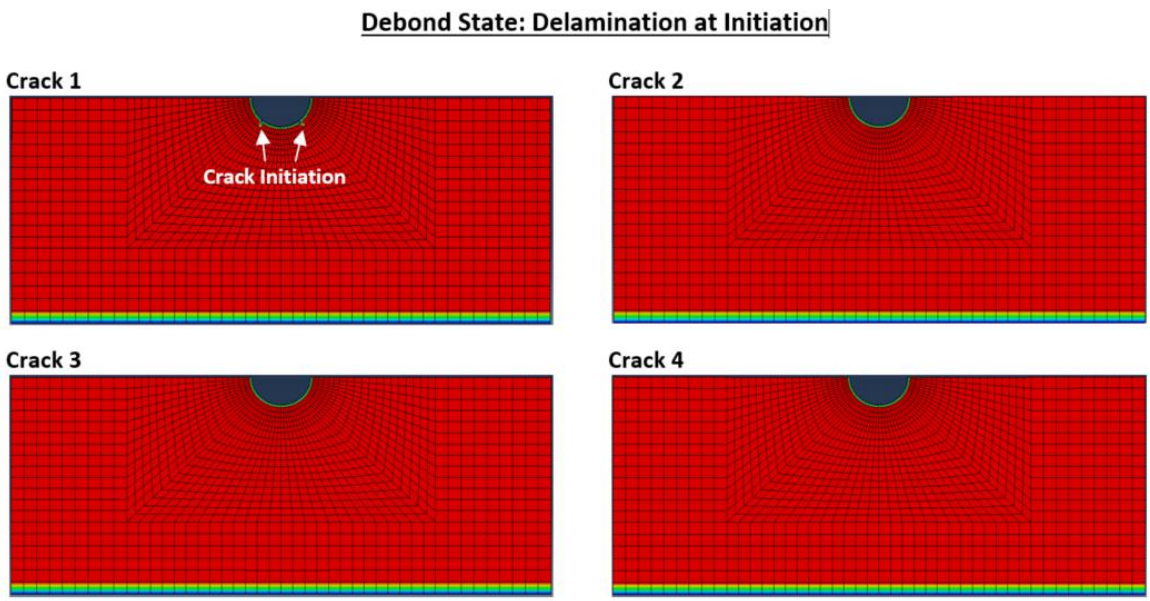

Figure 5.21: Bond state mapping of each crack. Red color indicate the plies between the cracks are still bonded and blue represents disbond. Crack 1 shows delamination initiation first.

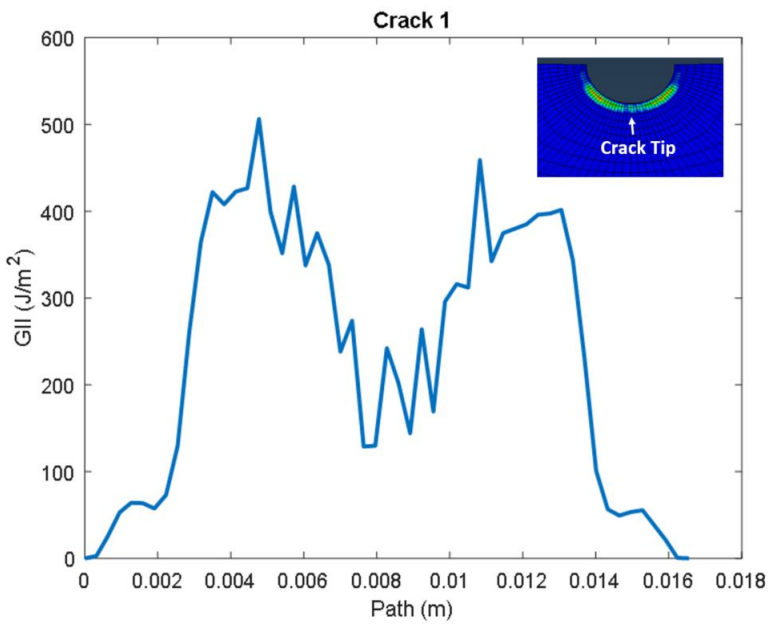

Figure 5.22: Strain energy release rate from Mode II of crack 1 prior to delamination initiation. Mode II is the dominating failure mode for delamination in this joint configuration. The material fracture toughness input was 554 J/m^2.

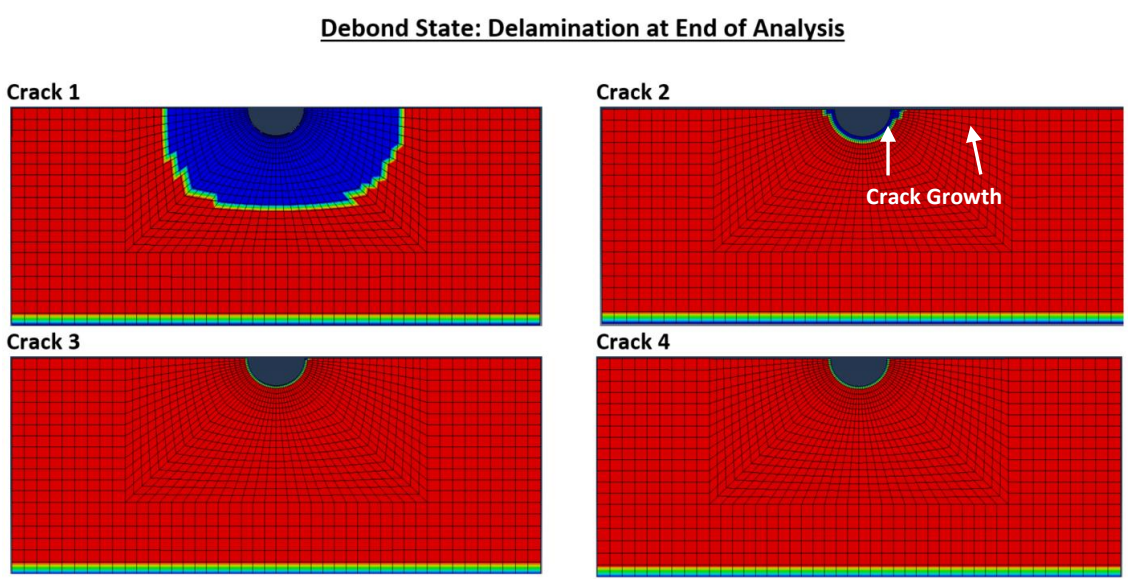

Figure 5.23: Final bond state status before analysis was terminated. Delamination propagated in Crack 1 and nodes began to release in crack 2.

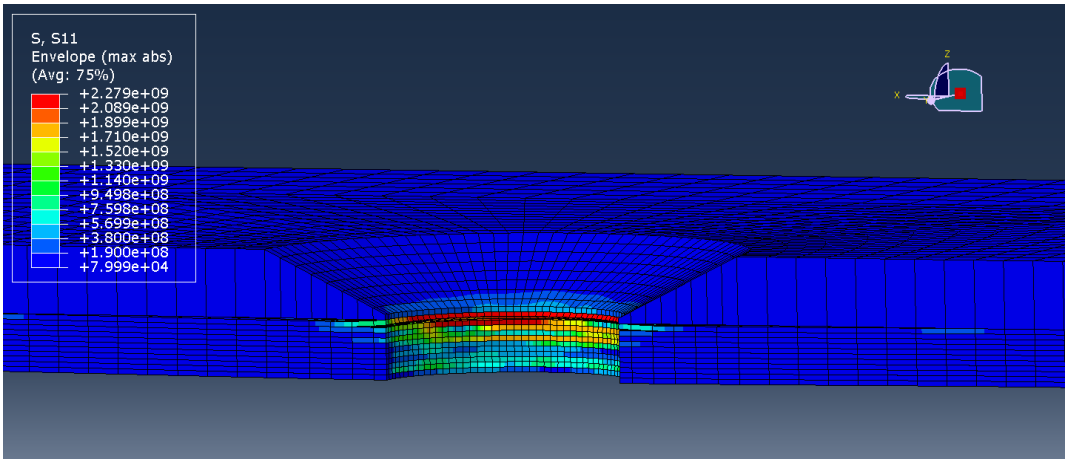

Figure 5.24: Bearing stress on the bolt-hole surface showing stress concentration between the concial and shank interface.

6 CONCLUSIONS

Static bearing tests were performed for double lap shear (DLS), single lap shear (SLS) and semi-circular notched (SCN) for three different laminate types. Results from the double lap and single lap shear test configurations showed that bearing failure is governed by damage accumulation due to matrix cracking, compression-induced fiber fracture, and delamination. Damage initiates at the most highly-loaded bearing surface of the straight shank region. During fatigue loading, large wedge-shaped features develop from fiber compression failures and serve to pry open the cracks, further propagating delamination via Mode I dominated opening. Comparing DLS and SLS loading configurations, the DLS shows lower initial bearing failure stress, but higher ultimate bearing strength, whereas the SLS exhibits plateau-like response after the ultimate stress is reached with a higher level of damage developed for a given applied load, relative to DLS.

Results from the DLS fatigue tests show that there is a correlation between joint stiffness, damage area, and hole elongation. When hole elongation increased, the damage area (observed by C-scan) also increased. During the first 25,000 cycles, each specimen type had an increase in hole elongation, stiffness, and damage area and then they all stabilized. Joint stiffness in particular increases in the first few thousands of cycles as local damage allows for more uniform contact of the fastener onto the bearing surface. After this initial stiffness increase, stiffness generally decreases as damage develops further away from the bearing surface (fiber compression, delamination). When cyclically loading DLS specimens at 66% of the ultimate bearing stress, the hole elongation exceeded the industry-based 4% hole elongation criteria early in the fatigue cycles

compared to applying 50% of the ultimate stress. On the contrary, at the 50% stress level, the hole elongation stabilizes even after 60,000 cycles. While these results are specific to this material system and laminate, a distinct threshold behavior exists for bolted joint fatigue where above a certain bearing stress level, hole elongation continues to grow with additional cycles, and below, it stabilizes after modest initial growth. Hole elongation has been found to be a strong indicator of internal damage. Increasing hole elongation correlates with increasing internal damage. No (or very low) hole elongation, equates to no internal damage, or no further growth if elongation stops growing. Hole elongation is thus recommended as a key damage inspection metric as it is visual based and requires no special equipment like C-scan. Due to the high clamping force from bolt torque-up, the SLS specimens exhibited different response than the un-torqued DLS specimens. The single lap shear fatigue test showed no damage area growth beyond the conical section or hole diameter elongation for the conditions tested.

Optical microscopy from DLS fatigue tests suggested that bearing damage may be affected by pin bending. Thus, the semi-circular notched experiments were conducted to study pin bending effects on bearing damage morphology, hole elongation and damage area growth mechanisms. Results show that the DLS static loaded specimens have greater bearing strength compared to the SCN countersunk specimens due to through-thickness constraint achieved by bolt clamp-up. The finger tight torque in the DLS bolted joint setup increased the bearing strength. Additionally, fatigue testing created shear crack formations near the bottom of the shank region (near outer surface), which were originally assumed to be caused by pin bending. However, the SCN countersunk experiment which allows for no pin bending also showed this damage at this location,

and therefore indicates that the pin bending had no strong effect on the bearing failure morphology for this diameter to thickness ratio. Instead, pin bending may contribute to material erosion found in the fatigue specimens. The microscopy comparisons showed that the straight shank region of the countersunk hole behaves similar to half of the through-hole specimen, which shows that shear cracks travel from the hole surface towards the outermost surface of the laminate. Large shear cracks mainly occur near the bottom of the shank region for both the SCN countersunk hole and DLS bolted joint test configurations, which may be caused by the instability of fibers near the outer face of the laminate instead of being at the interior of the laminate. The half of the laminate having the conical region provides local out-of-plane stiffness preventing shear cracks from forming.

FE modeling of the SCN specimen is able to provide qualitative insights on stress concentration regions on the bolt-bearing surface that cannot be observed during experimental testing. However, the complexity of modeling the failure modes associated with composite joint bearing failure using built-in Abaqus capabilities shows the need for advance modeling techniques and experimental testing.

REFERENCES

[1] Ireman, Tomas, Ranvik Tron and Eriksson Ingvar. "On Damage Development in Mechanically Fastened Composite Laminates." Composite Structures, 2000. 151-171.

[2] Lawlor, V.P., W.F. Stanley and M.A. McCarthy. "Characterisation of Damage Development in Single Shar Bolted Composite Joints." *Plastic, Rubber, and Composites*. Macromolecular Engineering, 2002. 126-133.

[3] D5961, ASTM. "Standard Test Method for Bearing Response of Polymer Matrix Composite Laminate." *American Society of Testing Materials*. 2013.

[4] Ekh, J., J Schon and L.G. Melin. "Secondary Bending in Multi Fastener, Composite-to-Aluminum Single Shear Lap Joints." Engineering, Composites Part B:. 2005. 195-208.

[5] Chishti, Maajid, Wang Hui Chun, Thomson S. Rodney, Orifici, Adrian "Progressive Damage in Single Lap Countersunk Composite Joints." Material Science and Engineering, 2010.

[6] McCarthy MA, Lawlor VP, Stanley WF, McCarthy CT. "Bolt-hole Clearance Effectsand Strength Criteria in Single-bolt, Single-lap, Composite Bolted Joints."Composite Science of Technology, 2002. 1415–31.

[7] Qin, Tianliang, Zhao Libin, Zhang Jianyu. "Fastener Effects on Mechanical Behaviors of Double-Lap Composite Joints." Composite Structures, 2013. 413-423.

[8] Chishti M, Wang CH, Thomson RS, Orifici AC. "Numerical Analysis of Damage Progression and Strength of Countersunk Composite Joints." Composite Structures, 2012 .643–53.

[9] Persson, Erik, Eriksson, Ingvar, Zackrisson Leif, "Effects of Hole Machining Defects on Strength and Fatigue Life of Composite Laminates." Composite Part A: Applied Science Manufacturing, 1997. 141-151.

[10] Bonnet, Cedric, Poulachon, Gerard, Rech Joel, Girard, Yannick, Costes, Philippe Jean. "CFRP Drilling: Fundamental Study of Local Feed Force and Consequences on Hole Exit Damage." International Journal of Machine Tools and Fracture, 2015. 57-64.

[11] Wong TL, Wu SM, Groy GM. "Analysis of Delamination in Drilling Composite Materials." Proceedings of the 14th SAMPE Technology Conference, 1982. 471-483.

[12] Ho-Cheng H., Dharan C.K.H., “Delamination during Drilling in Composite Laminates.” Journal of Engineering for Industry, 1990. 236-236.

[13] Karnik SR, Gaitonde VN, Campos Rubio J, EstevesCoreia A, Abroa AM, DAvim JP. “Delamination in Drilling of Polymeric Composites.” Journal of Material Process Technology, 2007. 204-209.

[14] Krishnaraj Vijayan, Prabukarthi A., RamanthanArun, Elanghovan N., Kumar, Senthil M., ZitouneRedouane, Davim J.P. “Optimization of Machine Parameters at High Speed Drilling of Carbon Fiber Reinforced (CFRP) Laminates.” Composite: Part B, 2012. 1791-1799.

[15] Durao Luis Miguel P., Tavares Joao Manuel R.S., Albuquerque Victor Hugo C.de, Marques Jorge Filipe S., Andrade Oscar N.G. “Drilling Damage in Composite Materials.” Materials, 2014. 3902-3819.

[16] Wang, Hong-Sheng, Hung Chang-Li and Chang Fu-Kuo. "Bearing Failure of Bolted Composite Joints. Part I: Experimental Characterization." Journal of Composite Materials, 1996. 1284-1313.

[17] Crews John H. “Bolt-Bearing Fatigue of a Graphite/Epoxy Laminate.” National Aeronautics and Space Administration Technical Memorandum, 1980. 1-30.

[18] Eriksson, Ingvar. “On the Bearing Strength of Bolted Graphite/Epoxy Laminates.” Journal of Composite Materials, 1990. Vol. 24, 1246-1269.

[19] Xiao Yi, Ishikawa Takashi. “Bearing Strength and Failure Behavior of Bolted Composite Joints (Part I: Experimental Investigation).” Composites Science and Technology, 2005.

[20] Khashaba U.A., Sallam H.E.M, Al-Shorbagy A.E., Seif M.A. “Effect of Washer Size and Tightening Torque on the Performance of Bolted Joints in Composite Structures.” Composite Structures, 2006.

[21] Irisarri F.X., Vandellos T., Paulmier P., Laurin F. “Experiments and Modeling of Clamping Effects on the Bearing Strength of Mechanically Fastened Joint in CFRP Laminates.” European Conference on Composite Materials, 2014.

[22] Quinn W. J., Matthews F.L. “The Effect of Stacking Sequence on the Pin-Bearing Strength in Glass Fiber Reinforced Plastic.” Journal of Composite Materials, 1977. Vol. 11. 139-145.

[23] Smith P.A., Pascoe K.J. “The Effect of Stacking Sequence on the Bearing Strengths of Quasi-Isotropic Composite Laminates.” Composite Structures, 1986. 1-20.

[24] Park, Heung-Joon. “Effects of Stacking Sequence and Clamping Force on the Bearing Strengths of Mechanically Fastened Joints in Composite Laminates.” Composite Structures, 2001, Vol. 53, no. 2. 213–221.

[25] Baba, B. Okutan. “Behavior of Pin-Loaded Laminated Composites.” Experimental Mechanics, 2006, Vol. 5, 589-600.

[26] Saunders, D.S., Galea S.C., Deirmendjian G.K. “The Development of Fatigue Damage around Fastener Holes in Thick Graphite/Epoxy Composite Laminates.” Composites, Vol.24, No.4, 1993 309-321.

[27] Starikov Roman, SchonJoakim. “Fatigue Resistance of Composite Joints with Countersunk Composite and Metal Fasteners.” International Journal of Fatigue, 2002. 39-47.

[28] Sypt, Paul Van Der, Cherif Mehdi, Bois Christophe. “Analysis of the fatigue behavior of laminated composite holes subjected to pin-bearing loads.” International Journal of Fatigue, 2017. 86-98.

[29] McCarthy M.A., Lawlor V.P., Stanley W.F. “An Experimental Study of Bolt-Hole Clearance Effects in Single-lap, Multibolt Composite.” Journal of Composite Materials, 2004. 799-825.

[30] Elisa Pietropaoli. “Virtual Crack Closure Technique and Finite Element Method for Predicting the Delamination Growth Initiation in Composite Structures.” IntechOpen Advances in Composite Materials, 2011. 463- 480.

[31] Wu, E.M. and Reuter R.C. Jr. “Crack Extension in Fiberglass Reinforced Plastics.” T and M Report, University of Illinois, 1965. 275.

[32] Benzeggagh, M.L. and Kenane, M. “Measure of Mixed-Mode Delaminaiton Fracture Toughness of Unidirectional Glass/Epoxy Composites with Mix-Mode Bending Apparatus.” Composite Science and Technology, 1996. 439-449.

[33] Reeder, J.R., Song, K., Chunchu, P.B. and Ambur, D.R. “Postbuckling and Growth of Delaminations in Composite Plates Subjected to Axial Compression, 43rd AIAA/ASME/ASCE/AHS/ASC Structures, Structural Dynamics, and Materails Conference, Denver, CO, AIAA, 2002. 1746-2002.

[34] VCCT for Abaqus User's Manual, Version 6.13, 2013.

[35] Bui, Q.V. "A Modified Benzeggagh-Kenane Fracture Criterion for Mixed-mode Delamination." Journal of Composite Materials, Vol. 45, No.4, 2011. 389-413.

[36] Krueger, Ronald. "Development and Applications of Benchmark Examples for Static Delamination Propagation Predictions." Proceeding for the 28th Annual Technical Conference of the American Society for Composites, 2011.

APPENDICES

A. DRILLING PROCESS FOR COMPOSITE MATERIAL

DLS and SLS specimens were drilled using the HASS T2 CNC milling machine at UC San Diego lab facility. The following steps were used in the drilling process for these specimens.

1. The specimen thickness at the hole location was measured to attain thickness information to ensure the conical region in the countersunk hole is half of that thickness. This was performed because specimens all had small variation in thickness.

2. To setup the specimen on the CNC machining table, use a stiff sacrificial material to place underneath the specimen. This helps prevent delamination from initiating when the drill exits the specimen. For these specimens, a 1/8" (3.175 mm) thick FR4 fiberglass was used as the sacrificial material. For every new hole, use a new surface on the sacrificial material.

3. Clamp all four sides of the specimen to ensure the vibration from the tool will not move the specimen. Do not apply too much pressure on the specimen when clamping to the machine table. This can cause local compression damage on the specimen.

4. Place a vacuum hose (may need to hold by hand) close to the tool during the drilling process to help remove all the debris and cool the tool. Do not use lubricant on the material.

5. Table 6.1 shows parameters used to drill, ream and countersunk the bolt-hole.

Table 6.1: Speed and feed rates used to fabricate all specimens used in this research.

	Drill	**Ream**	**Countersink**
Speed Rate	2000 rpm	200 rpm	2000 rpm
Feed Rate	50.8 mm/min	50.8 mm/min	50.8 mm/min
Pecking Depth	No Pecking	No Pecking	0.076 mm

6. After each tool has completed its operation, ensure to vacuum the debris out before drilling a new hole.

Drill Operation Tips:

- Since the drilling, reaming and countersunk cutting is all in one operation, do not remove the specimen from the machine table until all of these procedures are complete.

- If using a high steel drill bit for a 3/8” hole diameter, the drill was able to produce five quality holes before becoming dull. Two methods that can help save the drill life is to drill a pilot hole first using a smaller diameter drill. The second option is to use a carbide tip drill bit.

- For thick laminates, it is critical to perform pecking operation to help reduce overheating of the tool.
- If hole quality shows many small pockets of holes, it can be caused by overheating of the tool.
- If the hole has rough surfaces, it can indicate that the tool is dull. Also, if machining by a hand tool and great force is required to remove the material, this is also a sign that the tool is dull.

B. Fixture and Specimen Drawings

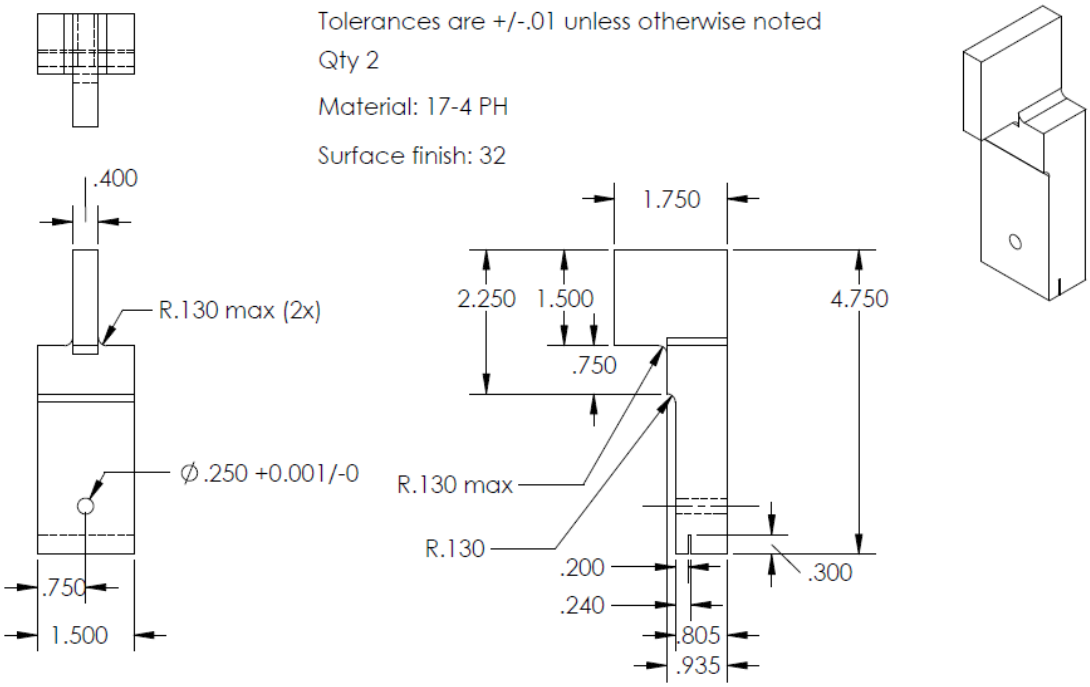

Figure 6.1: Single lap shear test fixture with dimensions in inches.

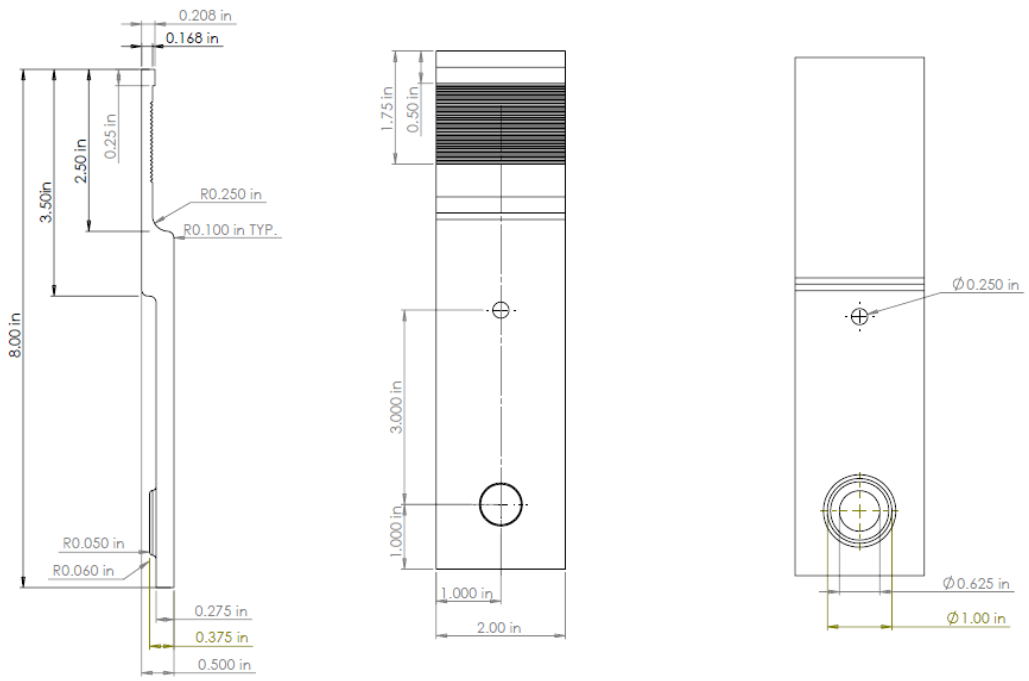

Figure 6.2: Double lap shear test fixture with dimensions in inches.

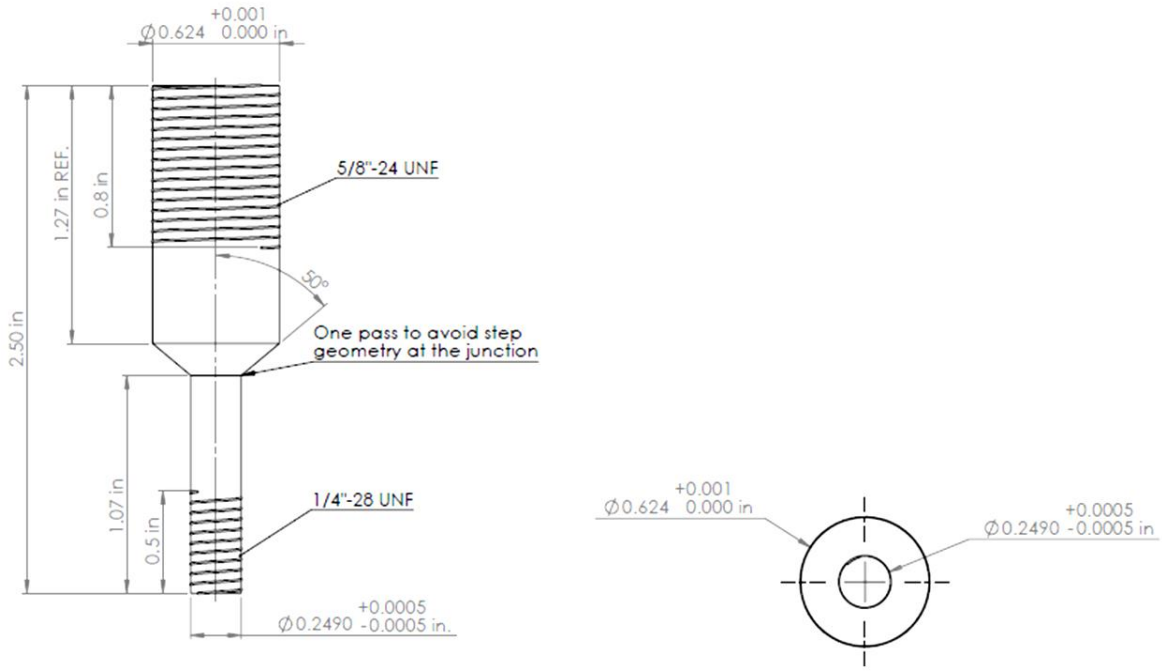

Figure 6.3: Dimensions of the custom designed pin used in the double lap shear test.

C. ULTRASONIC C-SCAN SETTINGS

Table 6.2: Ultrasonic C-scan input parameters on the UTwin software.

Composite Input Parameters	
Material Velocity	0.120 (in/µs)
A/D Gain	40 dB
LP Filter	5 MHz
HP Filter	2 MHz
A/D Average	1
Sample Rate	100
P/R Gain	0 dB
P/R Voltage	150 Volts
P/R Damp	40.5 (ohms)
P/R Frequency	5 MHz
Sync Mode	Initial
Sync Threshold	80

D. STATIC AND FATIGUE TEST PROCEDURE

Static and fatigue tests were performed on the MTS hydraulic 22-kip machine, which offers both Basic TestWare and MultiPurpose TestWare (MPT) programs (see Figure C.1 and Figure C.2). Basic TestWare was used for all static tests because the user interface for can be manually operated. All static tests were performed using the Basic TestWare program because users can easily change input parameters during the test operation. Since static tests were manually stopped based on the load versus displacement plot, this was the ideal program to use. All fatigue tests were done through the MPT program because a series of operations can be written to occur at the same time and in a sequential order. For instance, when the load is set to increase to a specific value before beginning the fatigue test, this data may not be necessary. Thus, in the MPT program, the data collection can be program to start after reaching

the specified load. Although this is a simple example explaining the capabilities of MPT, there are many commands that can be used in one experimental testing (see Figure C.2).

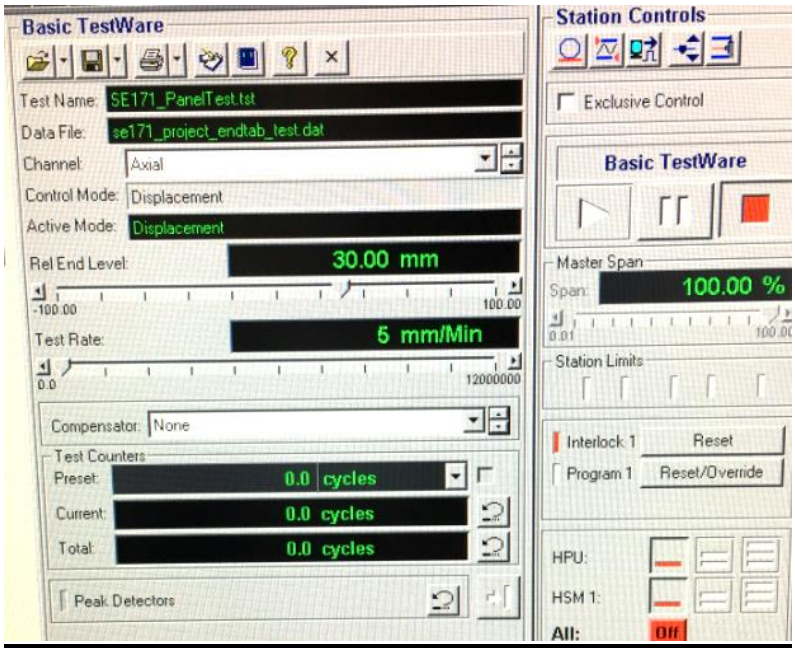

Figure 6.4: Basic TestWare user interface. Simple test operations can be modified during the test.

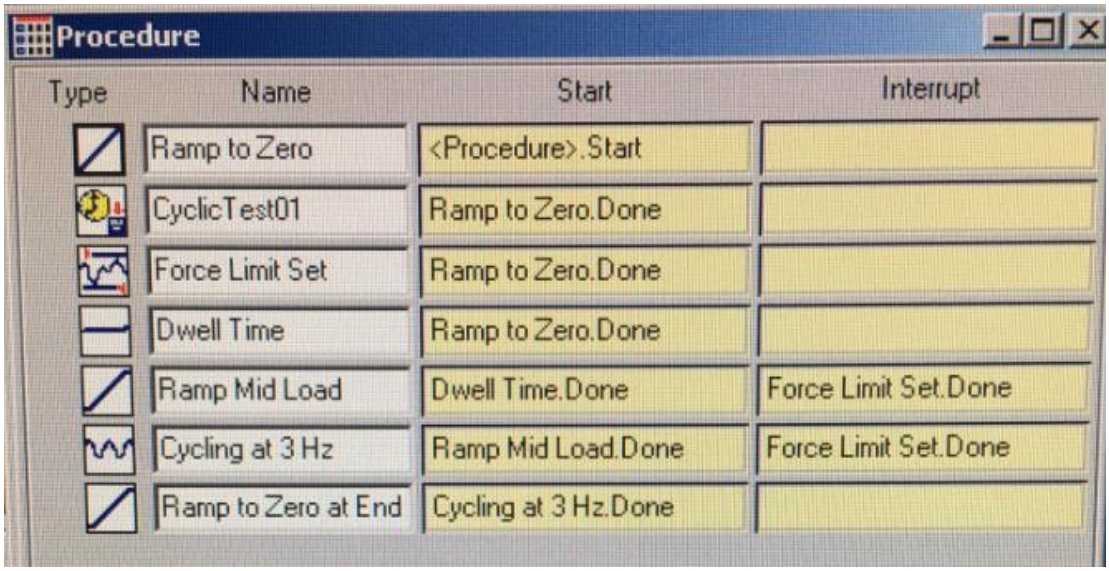

Procedure

Type	Name	Start	Interrupt
	Ramp to Zero	<Procedure>.Start	
	CyclicTest01	Ramp to Zero.Done	
	Force Limit Set	Ramp to Zero.Done	
	Dwell Time	Ramp to Zero.Done	
	Ramp Mid Load	Dwell Time.Done	Force Limit Set.Done
	Cycling at 3 Hz	Ramp Mid Load.Done	Force Limit Set.Done
	Ramp to Zero at End	Cycling at 3 Hz.Done	

Figure 6.5: Procedure used for fatigue test on the MPT program. Each type can either run simutaneously with one another or in a chronological order.

Tips for Fatigue Test on the MTS 22-kip Test Machine

- Have a few practice specimens to test the machine and program that was written to run the test.

- Before starting the test, ensure all limit switch are activated. If the test is load control then ensure the limit switch for load is on. The limit switch is used for safety purpose, such that it can turn off the hydraulic pump if the load exceeds the user defined value.

- Under load control, if the frequency is set too high, the machine can begin to cycle the specimen, then spike the load and break the specimen. Thus, it is critical to have limit switch activated during the test. The spike in load was caused by the

gain of the test machine. User is requesting the machine to reach a certain load value at such a high frequency that it does not give the machine enough time to reach that load.

- Solution: When load spike during test, check the P-Gain and I-Gain value. Large P-Gain value will make the MTS more responsive in reaching higher frequency fatigue test, but there is a risk of overshooting the load. In this research, P-Gain value of 0.20 and I-Gain of 0.015 was used for the DLS fatigue test and P-Gail value of 0.40 was used for SLS fatigue test.

E. Bearing Strength for DLS Specimens

Table 6.3: Bearing Strength for all specimens tested under static load.

DLS Bearing Strengths			
Specimen Type	*** Specimen 1**	**** Specimen 2**	***** Specimen 3**
Reference	1010 MPa	1242 MPa	1564 MPa
Large 0° Groupings	817 MPa	1086 MPa	1574 MPa
Large Angle Change	775 MPa	1554 MPa	1570 MPa

* Specimen 1: Stopped test immediately after load exceeds linear region of load versus displacement plot (low load).

** Specimen 2: Stopped test when load goes beyond linear region of load versus displacement plot, but before reaching ultimate failure (mid load).

*** Specimen 3: Stopped at when specimen fails (ultimate load).

F. HOLE ELONGATION MEASUREMENTS

Table 6.4: Hole elongation measured for the reference specimens that were cycled at 50% ultimate bearing stress.

Number of Cycles	Specimen 1		Specimen 2	
	in	mm	in	mm
0	0	0	0	0
2000	0.002	0.051	0.001	0.025
3000	0.003	0.076	0.002	0.051
4000	0.004	0.102	0.003	0.076
5000	0.005	0.127	0.003	0.076
6000	0.005	0.127	0.003	0.076
7000	0.006	0.152	0.004	0.102
8000	0.007	0.178	0.005	0.127
9,000	0.007	0.178	0.005	0.127
10,000	0.007	0.178	0.005	0.127
11,000	0.007	0.178	0.005	0.127
12,000	0.007	0.178	0.005	0.127
13,000	0.007	0.178	0.005	0.127
15,000	0.007	0.178	0.005	0.127
17,000	0.007	0.178	0.006	0.152
19,000	0.007	0.178	0.006	0.152
21,000	0.007	0.178	0.006	0.152
26,000	0.007	0.178	0.006	0.152
31,000	0.008	0.203	0.006	0.152
36,000	0.008	0.203	0.006	0.152
41,000	0.008	0.203	0.006	0.152
51,000	0.008	0.203	0.006	0.152
61,000	0.009	0.229	Pin Fractured	
71,000	0.009	0.229		
81,000	0.009	0.229		
83,384	0.009	0.229		
91,000	0.009	0.229		
110,000	0.01	0.254		
120,000	0.01	0.254		

Table 6.5: Hole elongation measured for the reference specimens that were cycled at 50% ultimate bearing stress.

Number of Cycles	Specimen 3		Specimen 4	
	in	mm	in	mm
0	0	0	0	0
1000	0	0	0	0
2000	0.001	0.025	0.001	0.025
5000	0.001	0.025	0.001	0.025
10000	0.005	0.127	0.002	0.051
20000	0.005	0.127	0.003	0.076
30000	0.006	0.152	0.003	0.076
40000	0.006	0.152	0.004	0.102
50,000	0.006	0.152	0.004	0.102
60,000	0.006	0.152	0.004	0.102
80,000	0.006	0.152	0.005	0.127

Table 6.6: Hole elongation measured for the specimen with large groupings of 0° plies that were cycled at 50% ultimate bearing stress.

Number of Cycles	Specimen 1		Specimen 2		Specimen 3	
	in	mm	in	mm	in	mm
0	0	0	0	0	0	0
2000	0.003	0.076	0.004	0.102	0.001	0.025
3000	0.004	0.102	0.007	0.178	0.001	0.025
4000	0.006	0.152	0.01	0.254	0.001	0.025
5000	0.007	0.178	0.016	0.406	0.001	0.025
6000	0.007	0.178	0.016	0.406	0.001	0.025
7000	0.008	0.203	0.016	0.406	0.001	0.025
8000	0.009	0.229	0.017	0.432	0.002	0.051
9,000	0.01	0.254	0.017	0.432	0.002	0.051
10,000	0.01	0.254	0.017	0.432	0.002	0.051
11,000	0.01	0.254	0.017	0.432	0.002	0.051
12,000	0.01	0.254	0.017	0.432	0.002	0.051
13,000	0.011	0.279	0.017	0.432	Pin Fractured	
15,000	0.011	0.279	0.017	0.432		
17,000	0.011	0.279	0.018	0.457		
19,000	0.011	0.279	0.018	0.457		
21,000	0.011	0.279	0.018	0.457		
26,000	0.011	0.279	0.018	0.457		
31,000	0.011	0.279	0.018	0.457		
36,000	0.011	0.279	0.018	0.457		
41,000	0.011	0.279	0.018	0.457		
51,000	0.012	0.305	0.018	0.457		
61,000	0.012	0.305	0.018	0.457		
71,000	0.013	0.330	0.018	0.457		
81,000	0.013	0.330	0.019	0.483		
101,000	0.013	0.330	0.019	0.483		
116,000	0.013	0.330	0.019	0.483		
120,000	0.013	0.330	0.019	0.483		

Table 6.7: Hole elongation measured for the specimen with large change in angle plies that were loaded to 50% ultimate bearing stress.

Number of Cycles	Specimen 1		Specimen 2		Specimen 3	
	in	mm	in	mm	in	mm
0	0	0	0	0	0	0
2000	0.002	0.051	0.01	0.254	0.006	0.152
3000	0.004	0.102	0.024	0.610	0.006	0.152
4000	0.005	0.127	0.026	0.660	0.007	0.178
5000	0.006	0.152	0.036	0.914	0.008	0.203
6000	0.006	0.152	0.032	0.813	0.013	0.330
7000	0.007	0.178	0.032	0.813	0.013	0.330
8000	0.008	0.203	0.032	0.813	0.013	0.330
9,000	0.008	0.203	0.034	0.864	0.013	0.330
10,000	0.008	0.203	0.039	0.991	0.013	0.330
11,000	0.008	0.203	0.04	1.016	0.013	0.330
12,000	0.008	0.203	0.041	1.041	0.013	0.330
13,000	0.008	0.203	0.041	1.041	0.028	0.711
15,000	0.008	0.203	0.041	1.041	0.028	0.711
17,000	0.008	0.203	0.041	1.041	0.028	0.711
19,000	0.008	0.203	0.041	1.041	0.029	0.737
21,000	0.008	0.203	0.041	1.041	0.029	0.737
26,000	0.008	0.203	0.041	1.041	0.029	0.737
31,000	0.008	0.203	0.041	1.041	0.029	0.737
36,000	0.008	0.203	0.041	1.041	0.029	0.737
41,000	0.008	0.203	0.041	1.041	0.029	0.737
51,000	0.008	0.203	0.042	1.067	0.029	0.737
61,000	0.008	0.203	0.043	1.092	Pin Fractured	
71,000	0.008	0.203	0.043	1.092		
81,000	0.009	0.229	0.043	1.092		
101,000	0.009	0.229	0.044	1.118		
116,000	0.01	0.254	0.044	1.118		
120,000	0.01	0.254	0.044	1.118		

Table 6.8: Hole elongation measured for the specimen with large change in angle plies that were loaded to 50% ultimate bearing stress. Continuation of Figure 6.5.

Number of Cycles	Specimen 3		Specimen 4	
	in	mm	in	mm
0	0	0	0	0
1,000	0	0	0	0
2,000	0.001	0.025	0.001	0.025
5,000	0.001	0.025	0.001	0.025
10,000	0.005	0.127	0.002	0.051
20,000	0.005	0.127	0.003	0.076
30,000	0.006	0.152	0.003	0.076
40,000	0.006	0.152	0.004	0.102
50,000	0.006	0.152	0.004	0.102
60,000	0.006	0.152	0.004	0.102
80,000	0.006	0.152	0.005	0.127

Table 6.9: Hole elongation measured for all specimens that were loaded to 66% ultimate bearing stress.

Number of Cycles	Reference Laminate		Large Groupings of 0° Plies		Large Change in Angle Plies	
	in	mm	in	mm	in	mm
0	0	0	0	0	0	0
1	0.025	0.635	0.005	0.127	0.008	0.203
1,000	0.052	1.321	0.047	1.194	0.011	0.279
2,000	0.052	1.321	0.051	1.295	0.011	0.279
3,000	0.052	1.321	0.054	1.372	0.012	0.305
4,000	0.063	1.600	0.059	1.499	0.012	0.305

Table 6.10: Hole elongation measured for specimen with large groupings of 0° plies that were loaded to 66% ultimate bearing stress. Continuation of Table 6.9, but for this laminate type.

Number of Cycles	Large Groupings of 0° Plies	
	in	mm
0	0	0
1,300	0.003	0.076
2,300	0.004	0.102
3,300	0.016	0.406
4,300	0.047	1.194
5,300	0.068	1.727
6,300	0.07	1.778
7,300	0.072	1.829

Table 6.11: Hole elongation measured for the reference lamiante and one with large chagne in angle plies that were loaded to 66% ultimate bearing stress. Continuation of

Table 6.10, but for these laminate type.

Number of Cycles	Reference Laminate		Large Change in Angle Plies	
	in	mm	in	mm
0	0	0	0	0
2,000	0.002	0.051	0.003	0.076
3,000	0.007	0.178	0.008	0.203
4,000	0.008	0.203	0.008	0.203
6,000	0.046	1.168	0.048	1.219
7,000	0.047	1.194	0.069	1.753
8,000	0.06	1.524	0.106	2.692
9,000	0.068	1.727	0.107	2.718
10,000	0.073	1.854	0.107	2.718